

NAVAL POSTGRADUATE SCHOOL Monterey, California



**PEBB Feedback Control Law Library
Volume 1
Three-Phase Inverter Control Algorithms**

by

John G. Ciezki and Robert W. Ashton

January 1999

19990309036

Approved for public release; distribution is unlimited.

Prepared for: Naval Surface Warfare Center (NSWC) Annapolis Det.

NAVAL POSTGRADUATE SCHOOL
Monterey, California


RADM ROBERT C. CHAPLIN
Superintendent


R. Elster
Provost

This report was sponsored by the Naval Surface Warfare Center (NSWC) Annapolis Detachment.

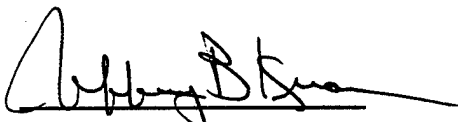
Approved for public release; distribution unlimited.

The report was prepared by:

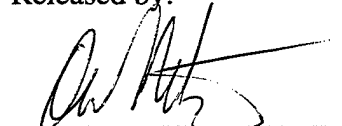

JOHN G. CIEZKI
Assistant Professor
Department of Electrical and
Computer Engineering


ROBERT W. ASHTON
Associate Professor
Department of Electrical and
Computer Engineering

Reviewed by:


JEFFREY B. KNORR
Chairman
Department of Electrical and
Computer Engineering

Released by:


DAVID W. NETZER
Associate Provost and
Dean of Research

REPORT DOCUMENTATION PAGE			Form Approved OMB No. 0704-0188	
<small>Public reporting burden for the collection of information is estimated to average 1 hour per response, including the time for reviewing instructions, searching existing data sources, gathering and maintaining the data needed, and completing and reviewing the collection of information. Send comments regarding this burden estimate or any other aspect of this collection of information, including suggestions for reducing this burden to Washington Headquarters Services, Directorate for Information Operations and Reports, 1215 Jefferson Davis Highway, Suite 1204, Arlington VA 22202-4302, and to the Office of Management and Budget, Paperwork Reduction Project (0704-0188), Washington DC 20503.</small>				
1. AGENCY USE ONLY (Leave blank)	2. REPORT DATE January 1999	3. REPORT TYPE AND DATES COVERED Technical Report		
4. TITLE AND SUBTITLE PEBB Feedback Control Law Library, Vol. 1: Three-Phase Inverter Control Algorithms		5. FUNDING NUMBERS N0016796WR60488		
6. AUTHOR(S) John G. Ciezki and Robert W. Ashton				
7. PERFORMING ORGANIZATION NAME(S) AND ADDRESS(ES) Department of Electrical and Computer Engineering Naval Postgraduate School Monterey, CA 93943-5000		8. PERFORMING ORGANIZATION REPORT NUMBER NPS-EC-99-002		
9. SPONSORING/MONITORING AGENCY NAME(S) AND ADDRESS(ES) Naval Surface Warfare Center Carderock Division/Annapolis Detachment 3A Leggett Circle Annapolis, MD 21402-5067		10. SPONSORING/MONITORING AGENCY REPORT NUMBER		
11. SUPPLEMENTARY NOTES The views expressed in this report are those of the author and do not reflect the official policy or position of the Department of Defense or the United States Government.				
12a. DISTRIBUTION/AVAILABILITY STATEMENT Approved for public release; distribution is unlimited.		12b. DISTRIBUTION CODE A		
13. ABSTRACT (Maximum 200 words) The Navy is actively engaged in developing Power Electronic Building Blocks (PEBBs) for its initiatives into DC Zonal Electric Distribution (DC ZEDS). DC ZEDS is a key element of the Integrated Power System (IPS) effort which seeks to modify the current surface combatant so that both ship service and ship propulsion electrical loads are powered from a common set of prime movers. Presently, the current generation of PEBB-like devices include high-power, fast-switching, high-bandwidth dc-dc converters and dc-ac inverters. This report summarized the algorithms required to control a conventional three-phase inverter. First, implementation issues regarding the Sine-Triangle Pulse-Width-Modulation and Space-Vector Modulation are presented with an emphasis placed on digital realizations. Then, two current control schemes are documented via analysis, design example, and simulation. Next, a complex voltage-control scheme is documented, a design example proffered, and simulation studies conducted to illustrate dynamic response. The report concludes with detailed analyses, designs, and simulations of two three-phase induction machine startup and speed control algorithms.				
14. SUBJECT TERMS PWM inverter, space vector, vector control, PEBB			15. NUMBER OF PAGES 81	
			16. PRICE CODE	
17. SECURITY CLASSIFICATION OF REPORT UNCLASSIFIED	18. SECURITY CLASSIFICATION OF THIS PAGE UNCLASSIFIED	19. SECURITY CLASSIFICATION OF ABSTRACT UNCLASSIFIED	20. LIMITATION OF ABSTRACT SAR	

Table of Contents

I. Background	1
Zonal Eleeltrical Distribution	1
DC Zonal Electrical Distribution	1
Power Electronic Building Block	2
Integrated Power System	2
Naval Postgraduate School Involvement	3
A. ARCP Inverter Control	7
1. Modulation Strategies	8
a. Sine-Triangle Pulse-Width-Modulation	8
b. Space Vector Modulation	10
2. Current Control Algorithms	20
a. Implementation in the Stationary Reference Frame	20
b. Implementation in the Synchronous Reference Frame	28
3. Voltage Control Algorithms	30
B. Induction Machine Startup Control	46
1. Constant Air-Gap Flux Control	46
2. Indirect Method of Vector Control	57
C. Concluding Comments	71
References	74

I. BACKGROUND

The U.S. Navy is actively engaged in promoting the application of state-of-the-art and commercial-off-the-shelf technologies to realize cost-effective platforms. In particular, research and development is focussed on improving producibility, enhancing operational flexibility, maximizing survivability, decreasing manning requirements and decreasing overall system cost. From the power system perspective, these goals have translated into research initiatives seeking to reduce the size and weight of the principle distribution components and to optimize the operation and survivability of key system elements. Presently, these efforts have been concentrated in four areas: zonal distribution, DC Zonal Electric Distribution (DC ZEDS), Power Electronic Building Blocks (PEBBs), and the Integrated Power System (IPS) also referred to as the Integrated Electric Drive (IED).

Zonal Electrical Distribution

The zonal distribution program has identified that a zonal architecture has a number of advantages over the current radial distribution architecture. The radial network includes generators supplying switchboards then a myriad of feeder cables strewn throughout the ship to provide power to vital and non-vital electrical loads. The zonal architecture is based on implementing a port and starboard bus and sectioning the ship service electrical loads into a number of zones delineated by watertight bulkhead compartments. Vital loads within a zone are connected to either bus via an auctioneering process. The advantages of zonal include the elimination of a significant amount of feeder cables, main busses only transition watertight compartments, the ship may be fabricated and tested in zones, and ship construction is markedly simplified. The arguments for zonal distribution are persuasive and the only issue that remains is whether the distribution busses are three-phase ac or dc.

DC Zonal Electrical Distribution

The DC ZEDS program is investigating the feasibility of zonal dc distribution. In DC ZEDS, the ac generator voltages are immediately rectified and the 1200 Vdc to 2000 Vdc is sent to the port and starboard busses. Each bus is connected to an electrical zone through a power converter called a Ship Service Converter Module (SSCM). The SSCM buffers the main bus and intra-zonal loads, monitors zone conditions, and adjusts and regulates the main bus voltage downward to a level commensurate with dc-to-ac inverter requirements (850-950 Vdc). Three-phase and single-phase ac voltages are synthesized within a zone by a power converter called a Ship Service Inverter Module (SSIM). The SSIM employs "intelligent" feedback control to provide tightly-regulated ac voltage and current to the corresponding loads. In addition, the SSIM on-board intelligence facilitates rapid current limiting which allows for a degree of self protection. It is envisioned that

standardized converter modules will be paralleled to achieve the required zone power requirements and will employ soft-switching technology in order to minimize switching losses and maximize control bandwidth. The principle benefits of DC ZEDS are that fault detection and clearing are both simpler and faster and that faults are now isolated to a particular zone. The time lag associated with initiating ac bus transfers is virtually eliminated, enhancing the integrity of power flow to critical electrical apparatus. In addition, DC ZEDS eliminates the need for most of the distribution transformers and ac switchgear providing substantial savings in size and weight. The ready availability of feedback-controlled dc-to-ac inverters facilitates the application of variable speed drives which in turn optimize the operation of blowers and pumps while implementing an automatic limiting of the in-rush currents experienced when starting large motors. DC ZEDS also eliminates the requirement that the ship service generators be operated at 60 Hz. This allows for a more optimized generator design in terms of size, weight and cost. Finally SSCMs and SSIMs are multifunctional and allow for the inclusion of more intelligent power management and fault protection. Thus, despite the fact that technological hurdles still persist in realizing a dc zonal distribution system, the advantages are clear and the arguments are sound.

Power Electronic Building Block

The PEBB program has concentrated on developing power electronic modules which combine a power section, current and/or voltage sensors and an on-board computer intelligence. In theory, the aggregate can be programmed and interconnected to realize intelligent circuit breakers or more complex power converters. The emphasis thus far has been on using existing technology to realize high-power high-bandwidth converters for applications such as DC ZEDS. The high-bandwidth control is realized by employing switching frequencies greater than 20kHz together with DSP-based digital controllers. Owing to the intensive input/output (I/O) requirements of many of the DC ZEDS components, customized DSP resources are required which in turn require algorithms to be developed and corresponding code to be generated. The development of reliable multifunctional units has progressed as evidenced by several testbed demonstrations conducted at the Naval Surface Warfare Center (NSWC) in Annapolis Maryland.

Integrated Power System

Finally the IPS program has revisited the feasibility of supplying both ship service and ship propulsion requirements from a common set of prime movers. A current surface combatant utilizes four large General Electric LM2500 gas turbines and a clutch and reduction gear to deliver power to two Controllable-Reversible-Pitch (CRP) propellers. Low speeds are achieved by idling the turbine and adjusting the propeller pitch. Speeds

above 15 knots are achieved by a combination of pitch control and governed throttle control where the speed of the turbine is adjusted between 1200rpm and 3600rpm. Ship service is supplied from four Allison 501K gas turbines driving 2.5MW, 60Hz synchronous machines. Auxiliary Propulsion Units (APUs) are available to provide operation up to 5 knots and are powered from the ship service.

In electric drive, four prime movers deliver power to synchronous machines which in turn supply both ship service and ship propulsion power converters. Propulsion power converters feed propulsion motors which directly control propeller speed. The advantages of IPS are manifold. First, the number of prime movers is reduced which leads to associated benefits in manning, reliability, cost and prime mover efficiency. By no longer requiring the prime mover to be in line with the propeller shaft, the gas turbines can be located on higher decks reducing the size of inlet/outlet ducting and minimizing the probability of losing power during a flooding casualty. In addition, a shorter shaft line reduces the complexity of aligning equipment across several ship construction zones. Since flexible electrical connections link the various propulsion apparatus, any prime mover can be configured to power any propulsion converter and either propeller shaft. Also, by eliminating the direct connection of the reduction gears and gas turbines to the propeller shaft, electric drive will be considerably quieter than the current system, reducing ship signature. From a fuel consumption point of view, the prime mover speed is decoupled from the propeller shaft speed and thus the prime mover may be operated at its most efficient setting (around 3300rpm for an LM2500). This in turn reduces emissions. The infinitely variable speed control available with electric drive makes low-speed maneuvering and reversals simple and rapid. Finally, IPS also provides excess generating capacity that may be used for powering future electrical auxiliaries such as Pulse-Energy Weapons (PEWs) and the ElectroMagnetic Aircraft Launching System (EMALS). As was stated for DC ZEDS, several technical hurdles regarding motor and converter design remain to be resolved; however, as these issues are confronted by R&D resources, IPS will be available to contribute to the design of more cost-effective Naval platforms.

Naval Postgraduate School Involvement

During the past six years, personnel at the Naval Postgraduate School (NPS) have supported the research efforts into zonal distribution, DC ZEDS, PEBB and IPS through a number of reimbursable research projects and over twenty Master's theses. Currently, the principle focus of the faculty has been on generating deliverables concerning DC ZEDS and PEBB. In particular, NPS faculty have supervised the fabrication of several medium-power SSCM power sections, the design and validation of a number of SSCM feedback algorithms, the implementation of SSCM regulators using both analog and DSP resources, the analysis and implementation of various paralleling regimes for SSCMs, the

development of closed-loop algorithms for SSIMs, the study of the interconnection feasibility and dynamics of multiple SSCMs and SSIMs, the analysis and fabrication of a soft-switching SSCM, the analysis and simulation of a soft-switching SSIM, and the investigation of the effects of input filter parameters on the stability of the dc distribution system. A number of conference and journal publications have resulted from these research efforts.

In terms of student participation, the above efforts have been extensively supported by over twenty thesis projects. Kline (Dec. 1993) developed a detailed SIMULINK model of a representative portion of a shipboard electric power distribution system. He addressed the modeling and control of a three-phase synchronous generator. In Colby (Dec. 1993), the constant power characteristics of DC ZEDS was investigated and some observations regarding stability and controllability were made upon employing a reduced-order representation of the dc-dc converter modules using PSPICE. Mark Kipps (Mar. 1994) developed a means of using a built-in differential algebraic solver within ACSL to simulate stiffly-connected isolated power systems without relying on reformulated machine representations or introducing fictitious circuit components. Blalock (Mar. 1995) initiated some of the detailed modeling of a DC ZEDS system consisting of a phase-controlled rectifier, dc-dc buck chopper and three-phase inverter. In addition, he performed the preliminary investigations into various closed-loop algorithms for the buck chopper and implemented a bench-top hardware testbed. He then incorporated feedback control of the dc-dc converter using the dSPACE hardware-in-the-loop development system. Blalock further conducted hardware and software studies and used the results to validate his computer representations.

Paralleling and interleaving dc-dc buck choppers was first considered by Filor (Sep. 1995) in a detailed ACSL simulation exercise that included a model of a steam turbine driven synchronous machine, rectifier, filter and buck choppers. Some of the issues regarding paralleling were brought to the fore for treatment by future students. Salerno (Jun. 1996) significantly advanced the proposed closed-loop dc-dc converter algorithm, integrated a DSP solution, coded the algorithms, aided in implementing the hardware setup and conducted a series of validation studies. Close to the same time, Oberley (Dec. 1996) developed a detailed ACSL representation of an ARCP inverter. Then using reduced-order representations, investigated various stationary and synchronous reference frame current control algorithms using a hardware testbed and the dSPACE hardware-in-the-loop development system. In addition, he investigated and contrasted the PWM implementations using Sine-Triangle PWM (STPWM) and Space Vector Modulation (SVM). These studies were conducted in ACSL assuming an RL load. Finally, Oberley considered an involved feedback/feedforward voltage control scheme which involved significant reference frame theory. In Nelson (Dec. 1996), the one-cycle control algorithm

for a buck chopper was considered and implemented. Comparisons were made between the computer representation and the hardware. Allen (Mar. 1997) documented the design and fabrication of several dc-dc buck chopper power sections while Badorf (Jun. 1997) detailed the controller design, implemented the required gating circuitry, and built and documented the associated analog control hardware. Badorf also developed ACSL simulations of a variety of interconnection possibilities for DC ZEDS and performed various transient studies.

Langlois (Jun. 1997) supervised the fabrication of a PEBB testbed used for interconnecting buck choppers and ARCP inverters. He then compiled some hardware studies investigating the transient response of the units for different configurations and loadings. In Hanson (Jun. 1997), the operation of the PUC was documented and the closed-loop algorithm for the buck chopper was programmed and validated. In addition, Hanson set forth the approach for implementing the closed-loop control of the ARCP inverters. Floodeen (Sep. 1998) further delved into the operation of the PUC and investigated developing C++ programs for controlling the various converters. In addition, Floodeen incorporated several auxiliary functions into the buck chopper control, including a non-droop based algorithm. He also set forth the method and coding required to implement the closed-loop current control of the ARCP. Presently, Moore (Mar. 1999) is investigating a de-centralized buck chopper paralleling algorithm that relies on injected signal detection. He plans to develop a hardware testbed to illustrate proof-of-concept. Marinac (Sep. 1999) will extend Moore's results to the paralleling of ARCP inverters. Greseth (Sep. 1999) is investigating the stability issues regarding the dc-dc converter input filters and generator/rectifier source. In particular, the stability problems associated with the constant power loads is analyzed and simulated using ACSL. A hardware testbed is used to validate conclusions.

There have been a host of other thesis topics including induction motor vector control (Pierce, Sep. 1995), cycloconverter drives for ship propulsion (Mercer, Dec. 1996) and a paper study on integrated electric drive design issues (Arrington, Sep. 1998) that have contributed to various aspects of IPS. Work has been performed on the simulation and control of solar-powered vehicles (Roerig, Mar. 1995 and Yourkowski, Mar. 1996) and the design and development of a UPS for a marine vehicle (Garcia, Dec. 1994 and Callahan, Mar. 1997). Zupfer (Dec. 1993) and Jones (Jun. 1995) investigated Active Power Line conditioner issues while Hand (Mar. 1994) was involved in the development of a power supply for an amateur satellite. Finally, hardware setups were used to perform investigations into a slip energy recovery system (Tait, Dec. 1995) and a Mapham converter (Tyner, Dec. 1995).

The remainder of this report focusses on the deliverables pertaining to a control law library for PEBB devices. The following sections contain detailed descriptions of closed-loop algorithms for dc-dc converters, dc-ac inverters and ac-dc phase-controlled rectifiers. These algorithm are designed to be realizable with the PEBB Universal Controller (Generation 0) and have been validated using detailed and reduced-order Advanced Continuous Simulation Language (ACSL) simulation models.

A. ARCP Inverter Control

The Auxiliary Resonant Commutated Pole (ARCP) inverter operates similar to a classical three-phase bridge inverter except that at the switching instances, auxiliary circuitry ensures that each semiconductor device is activated with approximately zero volts across it. For a given output power level, the transistor soft-switching facilitates higher switching frequencies. By extending switching frequencies from about 20kHz up to 60kHz for units rated in the tens of kilowatts, the ARCP inverter allows for faster-acting higher-bandwidth feedback control systems to regulate the voltages across or currents through a three-phase load and for smaller output filter elements.

An ARCP inverter consists of six main transistors with freewheeling diodes and a set of six auxiliary transistors with corresponding freewheeling diodes. For the set of units delivered to NSWC (via NPS) by Penn State University (PSU), the user has the option of either generating all twelve device gate signals or specifying only the main transistor gate signals and allowing the ARCP unit to appropriately activate the auxiliary devices. All actuation signals are optically coupled to the ARCP to maximize isolation and optimize noise immunity. The Power Electronic Building Block (PEBB) Universal Controller Generation 0 (PUC-GEN0) was developed with extensive Input/Output (I/O) capability (12 optical output transmitters and 10 Analog-to-Digital converter input ports) to interface with the ARCP units. Currently, the PUC-GEN0 is Assembly Language programmable with future generations anticipated to be programmable in C. In the remainder of this section, it is assumed that the auxiliary device control was left to the on-board ARCP circuitry so that the PUC-GEN0 can be dedicated to implement more sophisticated closed-loop algorithms. This seems reasonable since future inverter algorithms may also require paralleling and condition monitoring features that would exhaust the I/O capability of the PUC-GEN0 if it was also required to control the auxiliary switches.

Closed-loop inverter control is a mature subject area. The intent of this section is to explore a number of closed-loop voltage and current algorithms that would be appropriate for three-phase naval shipboard loads. First, we will focus on how a duty cycle signal may be derived using Sine-Triangle Pulse-Width-Modulation (STPWM) and then using Space Vector Modulation (SVM). A brief exposition on reference frame theory will be included with SVM. Reference frame analysis is also key to the current and voltage control stratagems presented in the subsequent sections. The current control algorithms are addressed first, documenting the control in the stationary reference frame then extending the analysis to the synchronous reference frame. The voltage control algorithm is a sophisticated control loop incorporating both feedback and feedforward elements. Both the voltage and current controls can be ultimately implemented using either STPWM or SVM. Finally, two algorithms for implementing a current-limited induction machine startup are documented.

1. Modulation Strategies

The most basic inverter modulation strategies are the 180° (six-step) and 120° modes. The 180° mode involves gating the inverter leg switches in a complementary fashion with each device on for 180° of an output cycle. The signals for the three inverter legs are phase displaced by 120° to achieve a balanced set. The 120° mode gates each device in an inverter leg for 120° of an output cycle with 60° separating the gating of the upper and lower switches. Once again, the signals for the three inverter legs are phase displaced by 120° to achieve a balanced set. Both of these algorithms are simple but are unattractive since the fundamental output amplitude is not directly controllable and considerable harmonics are injected into the load. The solution is to intelligently place notches into these quasi-rectangular waveforms using one of the variants of Pulse-Width-Modulation (PWM).

a. Sine-Triangle Pulse-Width-Modulation

STPWM employs a high-frequency carrier waveform together with a balanced set of modulating signals at the desired output frequency. Each modulating signal controls the transistor switching for a given leg. When the modulating signal is greater (less) than the carrier waveform, the upper (lower) switch is gated. Three modes of operation are possible depending on the relative amplitudes of the carrier and modulation signals. If the modulating signal amplitudes are less than the carrier amplitude, STPWM is operating in the linear mode and the phase voltage amplitude is directly proportional to the modulating signal amplitude. For instance if V_{pk} denotes the peak value of the modulating signal, A_t the peak triangle amplitude and V_{dc} the inverter dc input voltage, the fundamental phase voltage is given by

$$v_{as,1} = V_{pk} \frac{V_{dc}}{2A_t} \cos(\omega t) \quad (1)$$

where ω is the desired output frequency in radians/sec. When the modulating signal amplitude exceeds the triangle amplitude, STPWM transitions into the pulse-dropping (over-modulation) mode where there is a nonlinear relationship between the modulation amplitude and the phase voltage amplitude. If we define the modulation index

$$M = \frac{V_{pk}}{A_t} \quad (2)$$

then

$$v_{as,1} = \frac{V_{dc} M}{\pi} \left[\sin^{-1}\left(\frac{1}{M}\right) + \frac{1}{M} \sqrt{1 - \left(\frac{1}{M}\right)^2} \right] \cos(\omega t) \quad (3)$$

Finally, if the modulating amplitude is significantly larger than the carrier amplitude, only

two waveform intersections occur per desired output cycle and STPWM operates in 180° mode and

$$v_{as,1} = \frac{2 V_{dc}}{\pi} \cos(\omega t) \quad (4)$$

In any of the modes as long as the modulating signals are not corrupted by harmonics and are at a much lower frequency than the carrier waveform, a given inverter transistor is switched "on" and "off" once per cycle of the carrier waveform. This fixes the switching frequency as compared to a hysteresis inverter control and also produces well-defined harmonics.

Normally, the modulating signals used in STPWM are derived from feedback and possibly feedforward signals. The strategy, together with protections against gating both transistors in a given inverter leg, is readily implemented using standard Integrated Circuit (IC) chips. However, it is intended that the PUC-GEN0 be used to control the ARCP so it is necessary to discretize the STPWM algorithm.

If we assume that we calculate the modulating signals each time we sample the feedback quantities, we implicitly assume that that modulating signal stays constant over a switching (triangle) cycle and the inverter leg duty cycle can be evaluated as follows. Designating D_{tA} , D_{tB} , and D_{tC} as the duty cycle amounts for each of the top switches in the inverter legs,

$$D_{tA} = \frac{A_t + V_{mod,a}}{2 A_t} \quad (5)$$

$$D_{tB} = \frac{A_t + V_{mod,b}}{2 A_t} \quad (6)$$

$$D_{tC} = \frac{A_t + V_{mod,c}}{2 A_t} \quad (7)$$

Theoretically the duty cycles are constrained to lie between zero and one; however, the turn-off and turn-on times of the transistors disqualify duty cycles that result in very narrow pulses. If t_{min} is the minimum time length achievable for a pulse, then

$$D_{min} = \frac{t_{min}}{\frac{T}{2}} \quad (8)$$

where $\frac{T}{2}$ is half of a switching period and

$$D_{max} = 1 - D_{min} \quad (9)$$

Thus, if a duty cycle falls between D_{max} and one, we need to round the desired value up to one, effectively eliminating that transition of the modulating and carrier waveforms. If a duty cycle falls between D_{min} and zero, we need to round the desired value down to zero.

The duty cycles can then be converted into counts for the PUC-GEN0 counter/timers and implemented as described by Floodeen. Issues that need to be considered are (1) the quantization effect of converting the duty cycle to a count, (2) the harmonic performance of the inverter in pulse-dropping mode, (3) the effect of the delay inserted between gating "off" a leg switch and gating "on" the other leg switch, (4) the selection of A_t together with the feedback gains, and (5) the effect on harmonics of using asynchronous STPWM where the switching frequency is not a multiple of the desired inverter output frequency.

b. Space Vector Modulation

A three-phase bridge inverter, as shown in Figure 1, has eight possible switching states as illustrated in Table 1 where it is assumed that the leg transistors are fired in a complementary fashion. Also, a '1' in the table denotes that the switch is closed; a '0' in the table denotes that the switch is open.

Table 1. Possible Inverter Switching States

State	S_1	S_2	S_3
1	1	0	0
2	1	1	0
3	0	1	0
4	0	1	1
5	0	0	1
6	1	0	1
7	1	1	1
8	0	0	0

The voltages across the lower transistor switches (v_{ap} , v_{bp} and v_{cp}) are known once the gating signals are specified. That is, if the lower switch is gated $v_{ap} = 0$, while if the upper switch is gated $v_{ap} = V_{dc}$. It can be shown that for balanced loads, including symmetrical induction machines and synchronous machines, it is always true that

$$v_{as} + v_{bs} + v_{cs} = 0 \quad (10)$$

which then allows us to formulate the phase voltages based solely on knowledge of v_{ap} , v_{bp} and v_{cp} .

$$v_{as} = \frac{2}{3} v_{ap} - \frac{1}{3} v_{bp} - \frac{1}{3} v_{cp} \quad (11)$$

$$v_{bs} = \frac{2}{3} v_{bp} - \frac{1}{3} v_{ap} - \frac{1}{3} v_{cp} \quad (12)$$

$$v_{cs} = \frac{2}{3} v_{cp} - \frac{1}{3} v_{ap} - \frac{1}{3} v_{bp} \quad (13)$$

The phase voltages for each inverter state can be found by substitution as illustrated in Table 2.

Table 2. Phase Voltages for Each Inverter State

State	v_{ap}	v_{bp}	v_{cp}	v_{as}	v_{bs}	v_{cs}
1	V_{dc}	0	0	$\frac{2V_{dc}}{3}$	$-\frac{V_{dc}}{3}$	$-\frac{V_{dc}}{3}$
2	V_{dc}	V_{dc}	0	$\frac{V_{dc}}{3}$	$\frac{V_{dc}}{3}$	$-\frac{2V_{dc}}{3}$
3	0	V_{dc}	0	$-\frac{V_{dc}}{3}$	$\frac{2V_{dc}}{3}$	$-\frac{V_{dc}}{3}$
4	0	V_{dc}	V_{dc}	$-\frac{2V_{dc}}{3}$	$\frac{V_{dc}}{3}$	$\frac{V_{dc}}{3}$
5	0	0	V_{dc}	$-\frac{V_{dc}}{3}$	$-\frac{V_{dc}}{3}$	$\frac{2V_{dc}}{3}$
6	V_{dc}	0	V_{dc}	$\frac{V_{dc}}{3}$	$-\frac{2V_{dc}}{3}$	$\frac{V_{dc}}{3}$
7	V_{dc}	V_{dc}	V_{dc}	0	0	0
8	0	0	0	0	0	0

The six-step algorithm is implemented by sequentially selecting the first six states, each assigned for $\frac{1}{6}$ of the desired output period.

Reference frame theory is frequently applied in the analysis of electric machinery in order to achieve marked simplification of the modeling equations. The transformations or change of variables are diffeomorphic, one-to-one, and simply allows us to view the machine dynamics in a different coordinate system. The stationary reference frame is frequently used in the analysis of induction machines. It consists of an algebraic relationship where fictitious q and d-quantities are derived from the actual phase quantities. The phase voltage quantities are transformed into the stationary reference frame by

$$v_{qs}^s = v_{as} \quad (14)$$

$$v_{ds}^s = -\frac{\sqrt{3}}{3} v_{bs} + \frac{\sqrt{3}}{3} v_{cs} \quad (15)$$

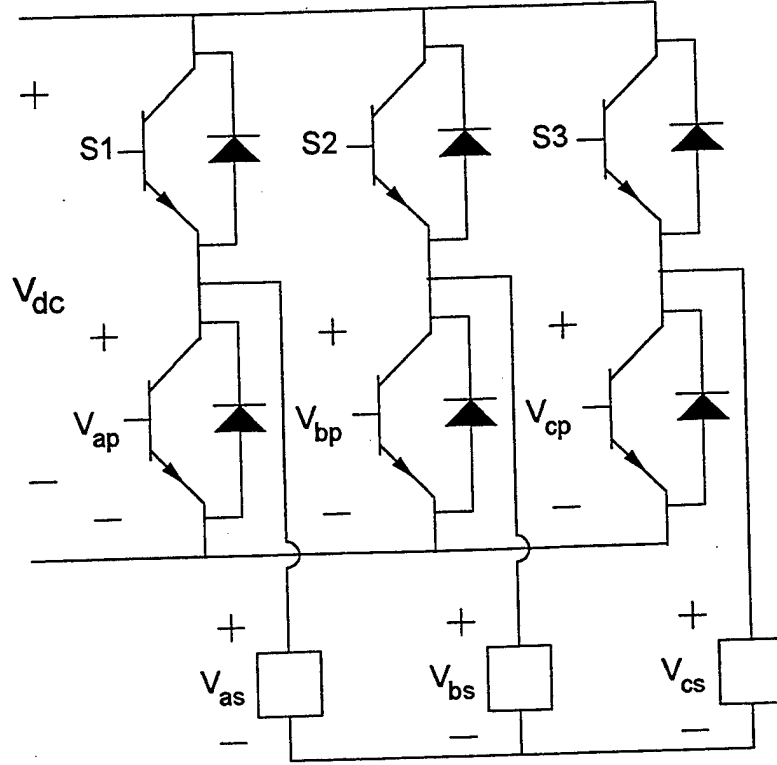


Figure 1. Three-Phase Voltage Source Inverter

If we view the stationary q-axis as being a horizontal axis and the stationary d-axis as being orthogonal and directed downward, we may then characterize the instantaneous values of v_{qs}^s and v_{ds}^s by a vector in the qd-plane where the amplitude of that vector is given by

$$\vec{v}_{qd,amp} = \sqrt{(v_{qs}^s)^2 + (v_{ds}^s)^2} \quad (16)$$

while the angle is given by

$$\vec{v}_{qd,ang} = \tan^{-1}\left(\frac{-v_{ds}^s}{v_{qs}^s}\right) = \gamma \quad (17)$$

Therefore, each inverter switching state corresponds to unique values of v_{qs}^s and v_{ds}^s and can thus be represented by a unique vector in the qd-plane. These are termed "space vectors" and are referred to herein as V_1 through V_8 . The vector descriptions are listed in Table 3 and are illustrated in Figure 2. As illustrated, the first six inverter space vectors are equal amplitude and are evenly displaced in the qd-plane. States 7 and 8 are represented by zero amplitude vectors.

The SVM idea stems from exploiting the inverter switching state representation in the qd-plane. If we can generate desired values for v_{qs}^s and v_{ds}^s , then we can implement those values by appropriately averaging the various inverter space vectors. Let's define $T_{sw,per}$ as

Table 3. Space Vector Representations of Inverter States

State	v_{qs}^s	v_{ds}^s	$\vec{v}_{qd,amp}$	$\vec{v}_{qd,ang}$
1	$\frac{2V_{dc}}{3}$	0	$\frac{2V_{dc}}{3}$	0°
2	$\frac{V_{dc}}{3}$	$-\frac{V_{dc}}{\sqrt{3}}$	$\frac{2V_{dc}}{3}$	60°
3	$-\frac{V_{dc}}{3}$	$-\frac{V_{dc}}{\sqrt{3}}$	$\frac{2V_{dc}}{3}$	120°
4	$-\frac{2V_{dc}}{3}$	0	$\frac{2V_{dc}}{3}$	180°
5	$-\frac{V_{dc}}{3}$	$\frac{V_{dc}}{\sqrt{3}}$	$\frac{2V_{dc}}{3}$	240°
6	$\frac{V_{dc}}{3}$	$\frac{V_{dc}}{\sqrt{3}}$	$\frac{2V_{dc}}{3}$	300°
7	0	0	0	origin
8	0	0	0	origin

the switching period. It will correspond to the amount of time allocated to the various inverter states used to synthesize the desired space vector. The qd-plane is divided into six sectors defined by $\vec{v}_{qd,ang}$. In order to minimize $T_{sw,per}$ relative to the desired output period, we choose to only use states adjacent to the sector in which the desired state vector resides. Also, a sequence of states exists which minimizes the number of switchings per cycle. These are illustrated in Table 4. Note that the optimal switch sequence uses both zero vectors, States 7 and 8. The averaging process may be viewed as follows. The weighting of adjacent inverter states is used to achieve the phase (γ) of the desired space vector. The weighting of these states relative to the zero states is used to achieve the desired space vector amplitude. Let's consider Sector I and define

$$T_{sw,per} = T_1 + T_2 + T_z \quad (18)$$

where T_1 is the time spent at State 1, T_2 is the time spent at State 2, and T_z is the time spent at the zero state. Note, the sequences illustrated in Table 4 consist of two such switching periods -- one starting at State 8 and one starting at State 7. If we next define V_1 as the space vector for State 1 and V_2 as the space vector for State 2, then the average space vector (\bar{V}) achieved over a switching period is given by

$$\bar{V} = \frac{T_1 V_1 + T_2 V_2}{T_{sw,per}} \quad (19)$$

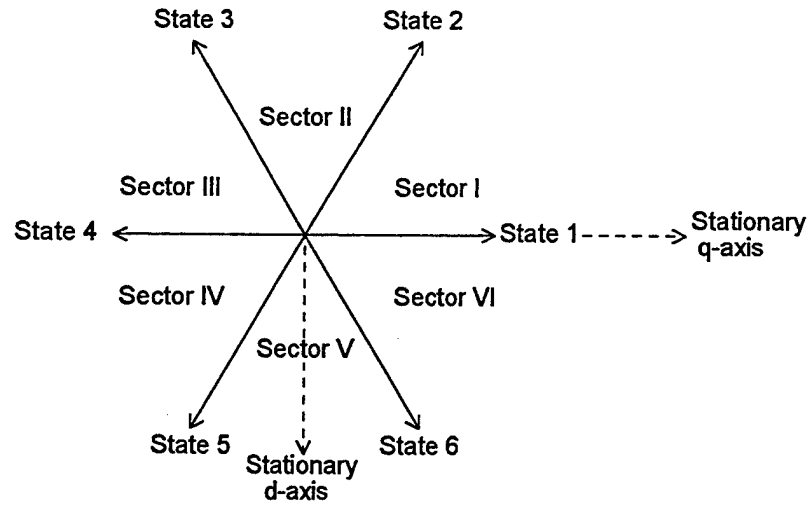


Figure 2. Illustration of Space Vectors

Table 4. Optimum Switch Sequences

Sector	$\vec{v}_{qd,ang}$	Switch Sequence
I	$0^\circ \leq \gamma < 60^\circ$	8,1,2,7,2,1,...
II	$60^\circ \leq \gamma < 120^\circ$	8,3,2,7,2,3,...
III	$120^\circ \leq \gamma < 180^\circ$	8,3,4,7,4,3,...
IV	$180^\circ \leq \gamma < 240^\circ$	8,5,4,7,4,5,...
V	$240^\circ \leq \gamma < 300^\circ$	8,5,6,7,6,5,...
VI	$300^\circ \leq \gamma < 360^\circ$	8,1,6,7,6,1,...

The assembly of the average space vector is illustrated in Figure 3. This expression is set equal to the desired space vector \vec{V}^* which can be decomposed into qd-components (in Sector I) as

$$v_{qs}^{s*} = V_{pk} \cos \gamma \quad (20)$$

$$v_{ds}^{s*} = -V_{pk} \sin \gamma \quad (21)$$

where γ is the angle of the desired space vector (equation 17). Substituting into the qd-

descriptions for V_1 and V_2 (Table 3) yields two equations in the two unknowns T_1 and T_2 .

$$T_1 = T_{sw,per} \frac{V_{pk}}{V_{dc}} \left[\frac{3}{2} \cos \gamma - \frac{\sqrt{3}}{2} \sin \gamma \right] \quad (22)$$

$$T_2 = T_{sw,per} \frac{V_{pk}}{V_{dc}} \sqrt{3} \sin \gamma \quad (23)$$

and then the zero state time is found from

$$T_z = T_{sw,per} - T_1 - T_2 \quad (24)$$

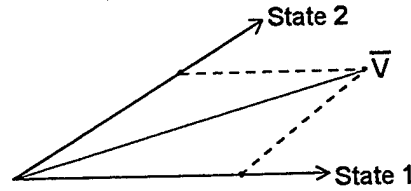


Figure 3. Derivation of the Average Space Vector

Given that we define

$$T_\alpha = T_{sw,per} \frac{v_{qs}^{s*}}{V_{dc}} \quad (25)$$

$$T_\beta = T_{sw,per} \frac{v_{ds}^{s*}}{V_{dc}} \quad (26)$$

we can establish the switch times for the devices in each sector. These are summarized in Table 5. As mentioned above, the optimal sequence for a given sector uses both zero states as illustrated in Table 4. For reasons of symmetry, half of the zero-state time illustrated in Table 5 is allocated to State 8 and half to State 7. Thus, the appropriate sequence may begin with either zero state. The corresponding duty cycles for the top switches in each leg are documented in Table 6. Whether the duty cycle is initially high or low for a given cycle depends on the current zero state. That is, if the previous sequence ends on State 8, then the upper switch remains low (open) for $1 - D$ of the cycle. If the sequence ends on State 7, the upper switch remains high (closed) for D of the cycle.

One issue that remains in implementing SVM is to establish what happens if the desired space vector has an amplitude larger than that achievable. This corresponds to the over-modulation region for STPWM. For Sector I, a given V_{pk} is realizable as long as the

Table 5. Switch Time Calculations

Sector	Non-Zero State Times	Zero-State Time
I	$T_1 = \frac{3}{2} t_\alpha + \frac{\sqrt{3}}{2} t_\beta$ $T_2 = -\sqrt{3} t_\beta$	$T_{sw,per} - T_1 - T_2$
II	$T_2 = \frac{3}{2} t_\alpha - \frac{\sqrt{3}}{2} t_\beta$ $T_3 = -\frac{3}{2} t_\alpha - \frac{\sqrt{3}}{2} t_\beta$	$T_{sw,per} - T_2 - T_3$
III	$T_3 = -\sqrt{3} t_\beta$ $T_4 = -\frac{3}{2} t_\alpha + \frac{\sqrt{3}}{2} t_\beta$	$T_{sw,per} - T_3 - T_4$
IV	$T_4 = -\frac{3}{2} t_\alpha - \frac{\sqrt{3}}{2} t_\beta$ $T_5 = \sqrt{3} t_\beta$	$T_{sw,per} - T_4 - T_5$
V	$T_5 = -\frac{3}{2} t_\alpha + \frac{\sqrt{3}}{2} t_\beta$ $T_6 = \frac{3}{2} t_\alpha + \frac{\sqrt{3}}{2} t_\beta$	$T_{sw,per} - T_5 - T_6$
VI	$T_6 = \sqrt{3} t_\beta$ $T_1 = \frac{3}{2} t_\alpha - \frac{\sqrt{3}}{2} t_\beta$	$T_{sw,per} - T_6 - T_1$

following condition is satisfied

$$V_{pk} \leq \frac{V_{dc}}{\sqrt{3}} \frac{1}{\cos(\gamma - 30^\circ)} \quad (27)$$

implying that a sinusoid of $\frac{V_{dc}}{\sqrt{3}}$ can be perfectly tracked through a sector (14% larger than in STPWM). If (27) is violated, inadmissible switch times will result. Two options exist: the desired space vector can be scaled down to the maximum amplitude given in (27), retaining the desired phase relationship, or the closest inverter state can be engaged for the entire $T_{sw,per}$. The determination can be based on which solution results in the smaller error vector. For instance using the scaling approach for Sector I, we would have the maximum vector amplitude constrained to be

$$V_{Lim} = \frac{V_{dc}}{\sqrt{3}} \frac{1}{\cos(\gamma - 30^\circ)} \quad (28)$$

and therefore the scaled desired qd-voltages would be given by

Table 6. Top Switch Duty Cycles

Sector	D_{tA}	D_{tB}	D_{tC}
I	$\frac{T_1 + T_2 + \frac{T_z}{2}}{T_{sw,per}}$	$\frac{T_2 + \frac{T_z}{2}}{T_{sw,per}}$	$\frac{\frac{T_z}{2}}{T_{sw,per}}$
II	$\frac{T_2 + \frac{T_z}{2}}{T_{sw,per}}$	$\frac{T_2 + T_3 + \frac{T_z}{2}}{T_{sw,per}}$	$\frac{\frac{T_z}{2}}{T_{sw,per}}$
III	$\frac{\frac{T_z}{2}}{T_{sw,per}}$	$\frac{T_3 + T_4 + \frac{T_z}{2}}{T_{sw,per}}$	$\frac{T_4 + \frac{T_z}{2}}{T_{sw,per}}$
IV	$\frac{\frac{T_z}{2}}{T_{sw,per}}$	$\frac{T_4 + \frac{T_z}{2}}{T_{sw,per}}$	$\frac{T_4 + T_5 + \frac{T_z}{2}}{T_{sw,per}}$
V	$\frac{T_6 + \frac{T_z}{2}}{T_{sw,per}}$	$\frac{\frac{T_z}{2}}{T_{sw,per}}$	$\frac{T_5 + T_6 + \frac{T_z}{2}}{T_{sw,per}}$
VI	$\frac{T_1 + T_6 + \frac{T_z}{2}}{T_{sw,per}}$	$\frac{\frac{T_z}{2}}{T_{sw,per}}$	$\frac{T_6 + \frac{T_z}{2}}{T_{sw,per}}$

$$V_{qs,new}^{s*} = V_{Lim} \cos \gamma \quad (29)$$

$$V_{ds,new}^{s*} = -V_{Lim} \sin \gamma \quad (30)$$

these would then be used to calculate switch times T_1 and T_2 . The resulting error amplitude would be given by

$$V_{err,amp1} = V_{pk}^* - V_{Lim} \quad (31)$$

Expressions for V_{Lim} in the remaining sectors are documented in Table 7. Assuming γ lies between -30° and 30° where State 1 is the closest, the voltage amplitude error in this case would be

$$V_{err,amp2} = \sqrt{\left(\frac{2V_{dc}}{3}\right)^2 + (V_{pk}^*)^2 - \frac{4}{3} V_{dc} V_{pk}^* \cos \gamma} \quad (32)$$

Expressions governing this voltage error for the remaining values of γ are listed in Table 8. Equations (31) and (32) can be appropriately compared to assess which solution minimizes the voltage amplitude error. The SVM algorithm may viewed in the following steps:

1. The control specifies commanded values of v_{qs}^{s*} and v_{ds}^{s*}
2. From which we can evaluate $\gamma = \tan^{-1}(\frac{v_{qs}^{s*}}{v_{ds}^{s*}})$, the angle of the desired space vector.
3. Determine the sector based on γ (Table 4).
4. Determine the desired peak value of the space vector
$$V_{pk}^* = \sqrt{(v_{qs}^{s*})^2 + (v_{ds}^{s*})^2}$$
5. Calculate the maximum achievable space vector for the γ (V_{Lim}) from Table 7.
- 6a. If V_{pk}^* is less than V_{Lim} then calculate t_α and t_β as directed in (25) and (26).
- 6b. If V_{pk}^* is greater than V_{Lim} then calculate scaled versions of the qd-commanded voltages from (29) and (30) which are then used in (25) and (26) to establish t_α and t_β . (Unless the error vector using a single space vector "full on" is smaller. Then, set the corresponding duty cycles to one or zero for the given leg and skip the remaining steps.)
7. Identify the switch times from Table 5.
8. Identify the switch leg duty cycles from Table 6.
9. Round duty cycles $D_{max} < D < 1$ up to one and duty cycles $0 < D < D_{min}$ down to zero.
10. If presently at State 8, the upper switch stays low (off) for $1 - D$. If presently at State 7, the upper switch stays high (on) for D .
11. Repeat each $T_{sw,per}$.

Table 7. Maximum Achievable Space Vector for Each Sector

Sector	V_{Lim}
I	$\frac{V_{dc}}{\sqrt{3}} \frac{1}{\cos(\gamma - 30^\circ)}$
II	$\frac{V_{dc}}{\sqrt{3}} \frac{1}{\cos(\gamma - 90^\circ)}$
III	$\frac{V_{dc}}{\sqrt{3}} \frac{1}{\cos(\gamma - 150^\circ)}$
IV	$\frac{V_{dc}}{\sqrt{3}} \frac{1}{\cos(\gamma - 210^\circ)}$
V	$\frac{V_{dc}}{\sqrt{3}} \frac{1}{\cos(\gamma - 270^\circ)}$
VI	$\frac{V_{dc}}{\sqrt{3}} \frac{1}{\cos(\gamma - 330^\circ)}$

Table 8. Error Vector Amplitudes Using Single State

Desired Vector Location	$V_{err,amp2}$
$-30^\circ < \gamma < 30^\circ$	$\sqrt{(\frac{2V_{dc}}{3})^2 + V_{pk}^{*2} - \frac{4V_{dc}}{3} V_{pk}^* \cos(\gamma)}$
$30^\circ < \gamma < 90^\circ$	$\sqrt{(\frac{2V_{dc}}{3})^2 + V_{pk}^{*2} - \frac{4V_{dc}}{3} V_{pk}^* \cos(\gamma - 60^\circ)}$
$90^\circ < \gamma < 150^\circ$	$\sqrt{(\frac{2V_{dc}}{3})^2 + V_{pk}^{*2} - \frac{4V_{dc}}{3} V_{pk}^* \cos(\gamma - 120^\circ)}$
$150^\circ < \gamma < 210^\circ$	$\sqrt{(\frac{2V_{dc}}{3})^2 + V_{pk}^{*2} - \frac{4V_{dc}}{3} V_{pk}^* \cos(\gamma - 180^\circ)}$
$210^\circ < \gamma < 270^\circ$	$\sqrt{(\frac{2V_{dc}}{3})^2 + V_{pk}^{*2} - \frac{4V_{dc}}{3} V_{pk}^* \cos(\gamma - 240^\circ)}$
$270^\circ < \gamma < 330^\circ$	$\sqrt{(\frac{2V_{dc}}{3})^2 + V_{pk}^{*2} - \frac{4V_{dc}}{3} V_{pk}^* \cos(\gamma - 300^\circ)}$

c. Hysteresis (Bang-Bang) Modulation

Hysteresis or Bang-Bang PWM is implemented by having the error between the commanded abc-quantities and the actual abc-quantities directly dictate the switch status in each inverter leg. For instance for Leg A,

If $i_{as}^* - i_{as} > \epsilon$, then close the top switch in Leg A.

If $i_{as}^* - i_{as} < -\epsilon$, then close the bottom switch in Leg A.

If within the hysteresis band, $-\epsilon < i_{as}^* - i_{as} < \epsilon$, then remain at the current state.

This strategy is most easily implemented using analog circuitry since it requires simply a fast-acting comparator with hysteresis. Problems arise when high-frequency harmonics corrupt the a-phase current measurements, resulting in sudden bursts of rapid switching in a given leg. This problem can be mitigated by either increasing the hysteresis band or by filtering the current measurement. Both solutions result in steady-state error between the commanded and actual quantities, where the level of error is oftentimes a complex function of load. Additional problems result when considering the implementation with the PUC-GEN0. For hysteresis control for a given output sample, the inverter leg will either be "full on" or "full off." Thus, the minimum width pulse derivable from a given inverter leg is fixed by the sampling period. Therefore a very high sampling frequency is required in order for the inverter to respond fast enough to track the desired waveform with sufficient accuracy and without introducing considerable harmonics. As a result, bang-bang PWM is more appropriately implemented using analog circuitry where the sampling rate of a DSP board is not at issue. Owing to this inherent limitation, hysteresis modulation was not considered any further in this effort.

2. Current Control Algorithms

A PWM Voltage-Source-Inverter (PWM-VSI) can be made to appear as an adjustable current source by having the modulating signals derived from a fast-acting current control loop. The 3-phase output voltages are specified within the admissible limits described in the previous section in order to minimize the error between the desired and actual currents. This report will consider two current control topologies and underscore the advantages and disadvantages of each. In addition to outlining the algorithm required for each, analysis tools useful for establishing feedback gains and system performance are derived and illustrated using a basic example. Both algorithms are based on reference frame analysis. Details of such analysis is documented in some degree in this report. The reader is referred to supplementary resources for additional information.

a. Implementation in the Stationary Reference Frame

The Stationary Reference Frame (STA-RF) current control is illustrated in Figure 4 where K_i and K_p represent integral and proportional gains. The signals i_{qs}^{s*} and i_{ds}^{s*} are the desired qd-currents in the STA-RF. The currents i_{qs}^s and i_{ds}^s are the actual qd-currents in the STA-RF and are related to the actual abc-load currents by

$$i_{qs}^s = i_{as} \quad (33)$$

$$i_{ds}^s = -\frac{1}{\sqrt{3}} i_{as} - \frac{2}{\sqrt{3}} i_{bs} \quad (34)$$

where the fact that the phase currents must sum to zero in a three-wire wye-connected load has been used to simplify (33) and (34) so that only two current measurements are required. For a delta-connected load, the ab-quantities above would be the line currents which must also sum to zero. Expressions for the signals V_{rq}^s and V_{rd}^s are derived from Figure 4 as

$$V_{rq}^s = K_p (i_{qs}^{s*} - i_{qs}^s) + K_i \int (i_{qs}^{s*} - i_{qs}^s) dt \quad (35)$$

$$V_{rd}^s = K_p (i_{ds}^{s*} - i_{ds}^s) + K_i \int (i_{ds}^{s*} - i_{ds}^s) dt \quad (36)$$

These signals are then either transformed out of the STA-RF to realize the balanced set of modulating signals which would be the inputs to STPWM or passed directly to the SVM algorithm as the desired space vector. For STPWM,

$$V_{mod,a} = V_{rq}^s \quad (37)$$

$$V_{mod,b} = -\frac{1}{2} V_{rq}^s - \frac{\sqrt{3}}{2} V_{rd}^s \quad (38)$$

$$V_{mod,c} = -V_{mod,a} - V_{mod,b} \quad (39)$$

If the phase angle of the currents is not critical and simply a commanded amplitude, I_{amp} , and frequency, ω_e , are required, then i_{qs}^{s*} and i_{ds}^{s*} may be derived from

$$i_{qs}^{s*} = I_{amp} \cos \theta_e \quad (40)$$

$$i_{ds}^{s*} = I_{amp} \sin \theta_e \quad (41)$$

where

$$\theta_e = \omega_e t \quad (42)$$

and ranges from zero to 2π radians.

The STA-RF control is straightforward to implement but has a basic limitation which is exposed upon analysis. We will next set forth the analysis of this architecture then consider the selection of control gains for the case of a balanced 3-phase RL-load. We will employ a vector notation where possible to condense the development. Notationally, the modulating signals are related to the control signals by

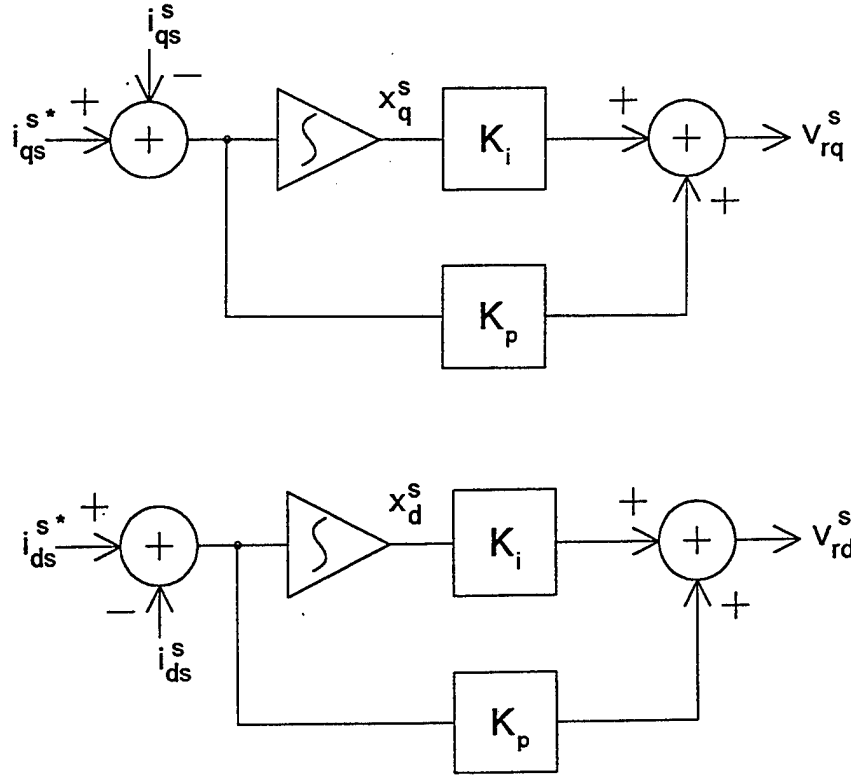


Figure 4. Stationary Reference Frame Current Control Implementation

$$\vec{v}_{\text{mod,abc}} = (\mathbf{K}_s^s)^{-1} \vec{v}_{\text{rqd0}}^s \quad (43)$$

where

$$\vec{v}_{\text{rqd0}}^s = \begin{bmatrix} V_{\text{rq}}^s \\ V_{\text{rd}}^s \\ 0 \end{bmatrix} \quad (44)$$

Note, the zero-sequence quantity is zero in (44). We argued previously in STPWM that the phase voltage quantities are related to the modulating quantities by (ignoring all but the fundamental)

$$\vec{v}_{\text{abcs}} = \mathbf{G} \vec{v}_{\text{mod,abc}} \quad (45)$$

where \mathbf{G} is the gain of the modulator and is given by

$$\mathbf{G} = \frac{V_{\text{dc}}}{2 A_t} \quad (46)$$

in the linear range and

$$\mathbf{G} = \frac{V_{\text{dc}}}{\pi A_t} \left[\sin^{-1} \frac{1}{M} + \frac{1}{M} \sqrt{1 - \left(\frac{1}{M}\right)^2} \right] \quad (47)$$

in the over-modulation range. The STA-RF phase voltages are related to \vec{v}_{abcs} by

$$\vec{v}_{qd0s}^s = K_s^s \vec{v}_{abcs} \quad (48)$$

Therefore if we substitute (43) into (45) and the result into (48), we find that

$$\vec{v}_{qd0s}^s = G \vec{v}_{rqd0}^s \quad (49)$$

The entire system is most conveniently analyzed in the Synchronous Reference Frame (SYN-RF) since the forcing functions are constants in that frame. As a result, the steady-state variables are constants and steady-state analysis is simplified. Upon introducing state variables x_q^s and x_d^s , we can write the modeling equations for the STA-RF implementation as

$$\rho x_q^s = (i_{qs}^{s*} - i_{qs}^s) \quad (50)$$

$$\rho x_d^s = (i_{ds}^{s*} - i_{ds}^s) \quad (51)$$

$$v_{qs}^s = G K_i x_q^s + G K_p (i_{qs}^{s*} - i_{qs}^s) \quad (52)$$

$$v_{ds}^s = G K_i x_d^s + G K_p (i_{ds}^{s*} - i_{ds}^s) \quad (53)$$

The equations are transformed into the SYN-RF by considering the mapping

$$\vec{v}_{qd0s}^e = {}^s K^e \vec{v}_{qd0s}^s \quad (54)$$

where

$${}^s K^e = \begin{bmatrix} \cos \theta_e & -\sin \theta_e & 0 \\ \sin \theta_e & \cos \theta_e & 0 \\ 0 & 0 & 1 \end{bmatrix} \quad (55)$$

or we can just consider the first two rows and columns since the zero-sequence quantities are all zero in this formulation. Equations (50)-(51) are rewritten in vector form as

$$\rho \vec{x}_{qds}^s = (\vec{i}_{qds}^{s*} - \vec{i}_{qds}^s) \quad (56)$$

If we substitute the transformation between reference frames, (56) becomes

$$\rho [({}^s K^e)^{-1} \vec{x}_{qds}^e] = ({}^s K^e)^{-1} (\vec{i}_{qds}^{e*} - \vec{i}_{qds}^e) \quad (57)$$

Expanding using the product rule,

$$({}^s K^e)^{-1} \rho \vec{x}_{qds}^e + \rho ({}^s K^e)^{-1} \vec{x}_{qds}^e = ({}^s K^e)^{-1} (\vec{i}_{qds}^{e*} - \vec{i}_{qds}^e) \quad (58)$$

and simplifying by multiplying through by ${}^s K^e$

$$\rho \vec{x}_{qds}^e = -{}^s K^e \rho ({}^s K^e)^{-1} \vec{x}_{qds}^e + (\vec{i}_{qds}^{e*} - \vec{i}_{qds}^e) \quad (59)$$

Upon performing the matrix multiplication and expanding, we find that

$$\rho x_q^e = -\omega_e x_d^e + (i_{qs}^{e*} - i_{qs}^e) \quad (60)$$

$$\rho x_d^e = \omega_e x_q^e + (i_{ds}^{e*} - i_{ds}^e) \quad (61)$$

The voltage equations (52)-(53) are similarly vectorized

$$\vec{v}_{qds}^s = G K_i \vec{x}_{qds}^s + G K_p (\vec{i}_{qds}^{s*} - \vec{i}_{qds}^s) \quad (62)$$

and transformed into the SYN-RF

$$({}^s K^e)^{-1} \vec{v}_{qds}^e = G K_i ({}^s K^e)^{-1} \vec{x}_{qds}^e + G K_p ({}^s K^e)^{-1} (\vec{i}_{qds}^{e*} - \vec{i}_{qds}^e) \quad (63)$$

to yield

$$\vec{v}_{qds}^e = G K_i \vec{x}_{qds}^e + G K_p (\vec{i}_{qds}^{e*} - \vec{i}_{qds}^e) \quad (64)$$

which expand to

$$v_{qs}^e = G K_i x_q^e + G K_p (i_{qs}^{e*} - i_{qs}^e) \quad (65)$$

$$v_{ds}^e = G K_i x_d^e + G K_p (i_{ds}^{e*} - i_{ds}^e) \quad (66)$$

Equations (59),(60),(65) and (66) represent the STA-RF control in the SYN-RF. The next step is to formulate the equations of the proposed load in the SYN-RF. A 3-phase RL-load is described by

$$\vec{v}_{abcs} = r_s \vec{i}_{abcs} + L_s \rho \vec{i}_{abcs} \quad (67)$$

where r_s is the phase resistance and L_s is the phase inductance. Transforming these equations into the SYN-RF yields

$$\rho i_{qs}^e = -\frac{r_s}{L_s} i_{qs}^e - \omega_e i_{ds}^e + \frac{1}{L_s} v_{qs}^e \quad (68)$$

$$\rho i_{ds}^e = -\frac{r_s}{L_s} i_{ds}^e + \omega_e i_{qs}^e + \frac{1}{L_s} v_{ds}^e \quad (69)$$

Therefore, combining (59),(60),(65),(66),(68) and (69) results in the following state space system description in normal form:

$$\rho \begin{bmatrix} i_{qs}^e \\ i_{ds}^e \\ x_q^e \\ x_d^e \end{bmatrix} = \begin{bmatrix} \frac{-r_s - G K_p}{L_s} & -\omega_e & \frac{G K_i}{L_s} & 0 \\ \omega_e & \frac{-r_s - G K_p}{L_s} & 0 & \frac{G K_i}{L_s} \\ -1 & 0 & 0 & -\omega_e \\ 0 & -1 & \omega_e & 0 \end{bmatrix} \begin{bmatrix} i_{qs}^e \\ i_{ds}^e \\ x_q^e \\ x_d^e \end{bmatrix} + \begin{bmatrix} G \frac{K_p}{L_s} & 0 \\ 0 & G \frac{K_p}{L_s} \\ 1 & 0 \\ 0 & 1 \end{bmatrix} \begin{bmatrix} i_{qs}^{e*} \\ i_{ds}^{e*} \end{bmatrix} \quad (70)$$

which is in the form

$$\rho \vec{x} = A_s \vec{x} + B_s \vec{u} \quad (71)$$

where A_s is the system matrix, \vec{x} is the state vector and \vec{u} is the vector of inputs. Equation (70) may be used to determine system eigenvalues for various choices of K_p and K_i and may also be used to determine the steady-state error. The steady-state error is found by

setting the derivative in (71) equal to zero and solving for the state vector \vec{x} .

$$\vec{x} = - (A_s)^{-1} B_s \vec{u} \quad (72)$$

The difference between the derived operating points in (72) and the values i_{qs}^* and i_{ds}^* provides a measure of the accuracy of the current control. To illustrate the design process, consider the sample parameter values listed in Table 9. The governing system eigenvalues may be evaluated for a variety of gains. In addition, suppose a desired amplitude of 10A is specified for the current ($i_{qs}^*=10A$ and $i_{ds}^*=0A$) then the steady-state error may be evaluated as well. Sample results are presented in Table 10.

Table 9. Parameters for STA-RF Current Control Example

r_s	L_s	V_{dc}	A_t	ω_e
25 Ω	20 mH	850 V	10 V	377 rad/sec

Table 10. Eigenvalue Analysis Results

K_p	K_i	eigs 1&2	eigs 3&4	I_{as} pk amp.
5	100	-18 +/- j377	-11857 +/- j377	8.96A
5	1000	-181 +/- j377	-11693 +/- j377	9.26A
1	250	-166 +/- j377	-3209 +/- j377	7.22A
0.1	250	-672 +/- j377	-790 +/- j377	7.96A
0.01	500	-636 +/- j1188	-636 +/- j434	10.24A
0.01	1500	-636 +/- j2045	-636 +/- j1291	10.33A

The final values of gains in the table were then used in a detailed ACSL simulation of the system. The STPWM algorithm was simulated in detailed. Initially, the q and d-stationary reference frame desired currents were set to an amplitude of 5A then around 0.06sec the amplitude was stepped up to 10A. The results are depicted in Figure 5. In this case, the limitations of the STA-RF controller are not apparent; however, what is obvious is that the accuracy is parameter dependent and as the load changes, the steady-state error will vary. In addition, the above table summarizes amplitude information and does not address phase error which is critical in a vector-controlled induction machine drive. The steady-state error issue results from the fact that we are attempting to regulate sinusoidal quantities. In the next section, the control action is moved to a reference frame where the desired quantities are constants. The result is that the integral action in the Proportional-Integral (PI) controller facilitates achieving zero steady-state error. One final point to be made is

that the eigenvalues and error listed in Table 10 are not the only issues driving the selection of the gains. One must also be aware that too large of gains will result in saturating the control, driving the STPWM algorithm into either over-modulation or six-step modulation. The results of employing too large of control gains are illustrated in Figure 6 where immediately following the step increase in desired current, the actual current tracking is unacceptable.

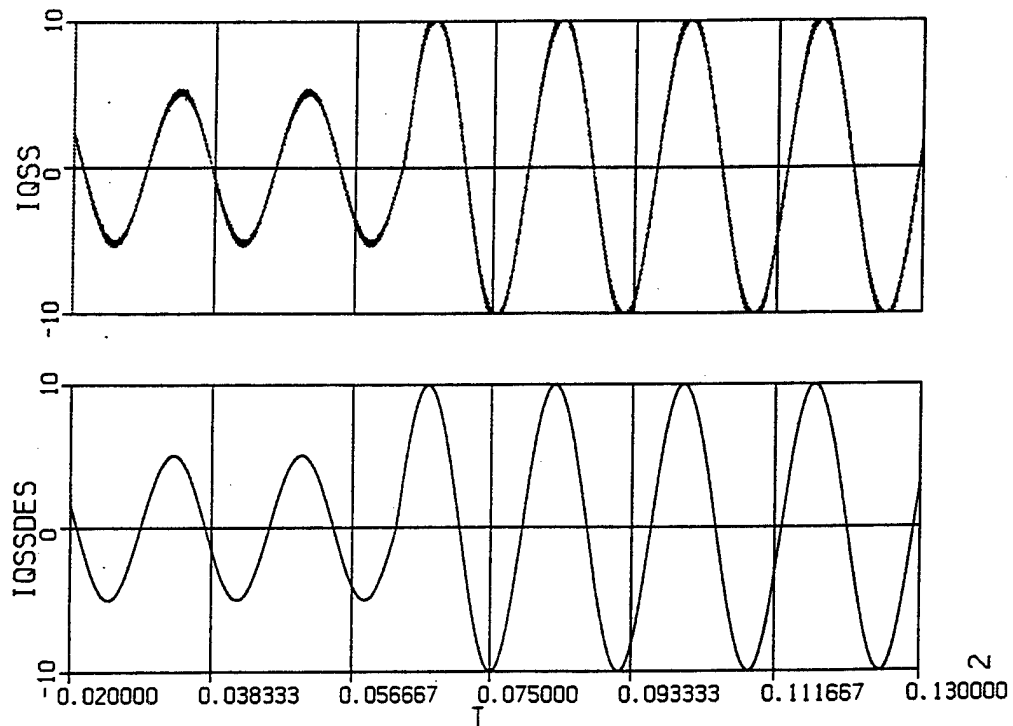


Figure 5. STA-RF Current Control Waveforms
(bot: commanded q-axis current, top: actual q-axis current)

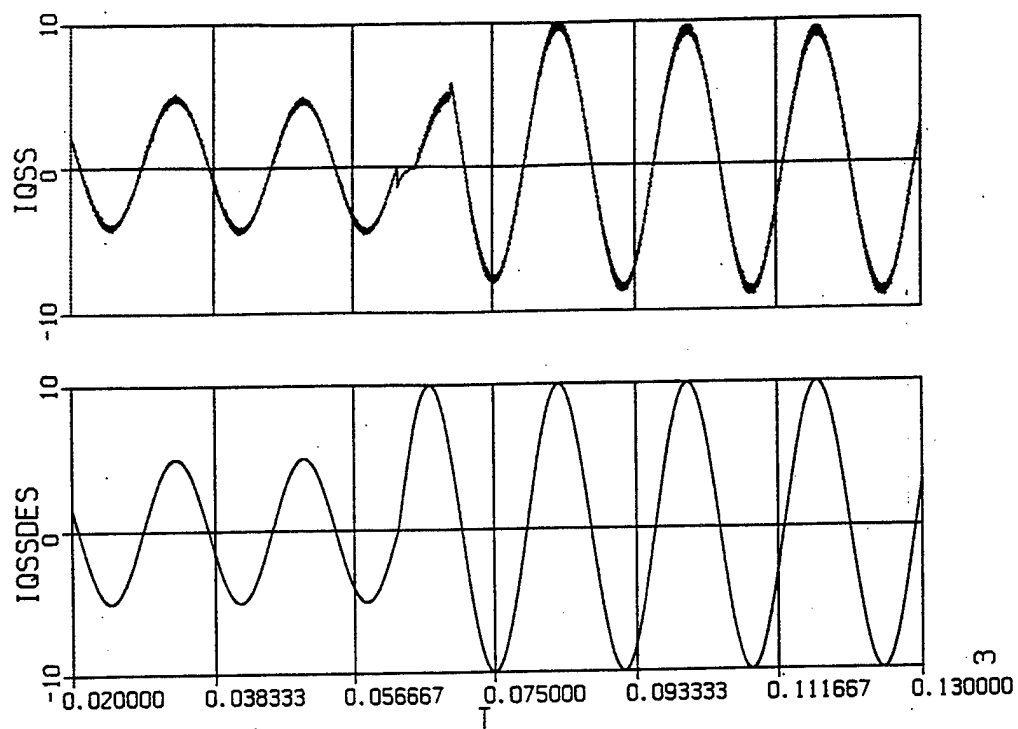


Figure 6. STA-RF Current Control Waveforms (overmodulation)
(bot: commanded q-axis current, top: actual q-axis current)

b. Implementation in the Synchronous Reference Frame

The Synchronous Reference Frame (SYN-RF) current control is illustrated in Figure 7 where K_{iq} and K_{id} represent the integral control gains and K_{pq} and K_{pd} represent the proportional control gains. The signals i_{qs}^{e*} and i_{ds}^{e*} are the desired qd-currents in the SYN-RF. The currents i_{qs}^e and i_{ds}^e are the actual qd-currents in the SYN-RF and are related to the actual abc-load currents by

$$\vec{i}_{qd0s}^e = K_s^e \vec{i}_{abcs} \quad (73)$$

where

$$K_s^e = \frac{2}{3} \begin{bmatrix} \cos \theta_e & \cos(\theta_e - \frac{2\pi}{3}) & \cos(\theta_e + \frac{2\pi}{3}) \\ \sin \theta_e & \sin(\theta_e - \frac{2\pi}{3}) & \sin(\theta_e + \frac{2\pi}{3}) \\ \frac{1}{2} & \frac{1}{2} & \frac{1}{2} \end{bmatrix} \quad (74)$$

The modeling equations for the SYN-RF control are derived directly from Figure 7 as

$$\rho x_q^e = (i_{qs}^{e*} - i_{qs}^e) \quad (75)$$

$$\rho x_d^e = (i_{ds}^{e*} - i_{ds}^e) \quad (76)$$

$$v_{qs}^e = G K_{iq} x_q^e + G K_{pq} (i_{qs}^{e*} - i_{qs}^e) \quad (77)$$

$$v_{ds}^e = G K_{id} x_d^e + G K_{pd} (i_{ds}^{e*} - i_{ds}^e) \quad (78)$$

where G is the gain of the PWM method ($G = \frac{V_{dc}}{2A_t}$ for STPWM in the linear range).

Incorporating these equations together with (68) and (69) results in the following state space normal depiction of the SYN-RF control.

$$\rho \begin{bmatrix} i_{qs}^e \\ i_{ds}^e \\ x_q^e \\ x_d^e \end{bmatrix} = \begin{bmatrix} \frac{-r_s - G K_{pq}}{L_s} & -\omega_e & \frac{G K_{iq}}{L_s} & 0 \\ \omega_e & \frac{-r_s - G K_{pd}}{L_s} & 0 & \frac{G K_{id}}{L_s} \\ -1 & 0 & 0 & 0 \\ 0 & -1 & 0 & 0 \end{bmatrix} \begin{bmatrix} i_{qs}^e \\ i_{ds}^e \\ x_q^e \\ x_d^e \end{bmatrix} + \begin{bmatrix} G \frac{K_{pq}}{L_s} & 0 \\ 0 & G \frac{K_{pd}}{L_s} \\ 1 & 0 \\ 0 & 1 \end{bmatrix} \begin{bmatrix} i_{qs}^{e*} \\ i_{ds}^{e*} \end{bmatrix} \quad (79)$$

which is in the form

$$\rho \vec{x} = A_e \vec{x} + B_e \vec{u} \quad (80)$$

One outright advantage of the SYN-RF implementation is that in the steady state ($\rho \vec{x} = 0$), there is no error; that is, $i_{qs}^e = i_{qs}^{e*}$ and $i_{ds}^e = i_{ds}^{e*}$. The "cost" of the implementation is that angle-dependent transformations are required to map the SYN-RF control signals back into abc-modulating signals and the actual sensed abc-currents into the required qd-feedback currents.

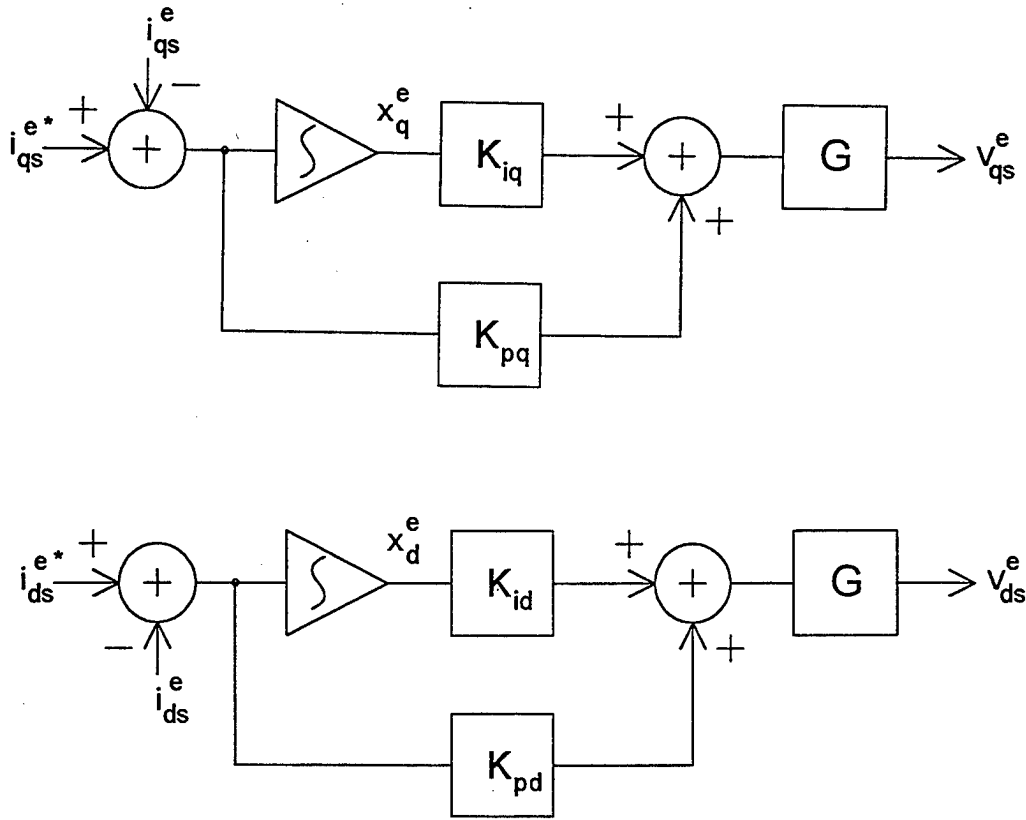


Figure 7. Synchronous Reference Frame Current Control Implementation

A simple design illustration is presented next. Considering the parameters listed in Table 9, eigenvalues may be computed for a variety of control gains. A procedure for placing the eigenvalues for a related problem is described in the next section and can be readily extended to this case study. The locations of the eigenvalues (or poles) in the complex plane directly influences transient response. The real-part of the dominant eigenvalue (closest to the $j\omega$ axis) is closely related to the settling time while the ratio of the imaginary to the real-part dictates the overshoot. Transfer function zeros in the neighborhood of these dominant eigenvalues will also impact the transient response and must be considered.

Since the integral action guarantees zero steady-state error for a constant input, we do not need to consider the impact of the gains on the resultant steady-state current amplitude. Table 11 documents how the eigenvalues transition in the complex plane for different gains. Once again, an effort should be made to minimize the gains in order to minimize the control effort and avoid overmodulation. The current control design was validated in ACSL using a detailed representation of the STPWM. Simulation results are presented in Figures 8 and 9. Initially, the load operates with $i_{qs}^* = 5A$ and $i_{ds}^* = 0A$. As the curves

indicate, there is no steady-state error. At about 0.06sec, i_{qs}^{e*} is stepped to 10A. The output current responds quickly as predicted by the eigenvalues, distortion is avoided as overmodulation is not entered due to the suitably small selection of K_p , and there is zero steady-state error. Despite being somewhat more involved to implement, the superior performance and robustness of the SYN-RF current control make it more attractive than its STA-RF counterpart.

Table 11. SYN-RF Design Example

K_p	K_i	Eigs 1&2	Eigs 3&4
0.05	1000	$-580 \pm j1119$	$-776 \pm j1496$
0.01	1000	$-545 \pm j1140$	$-726 \pm j1517$
0.01	2000	$-575 \pm j1783$	$-696 \pm j2160$
0.01	250	$-384 \pm j287$	$-888 \pm j664$
0.01	100	$-166 \pm j66$	$-1106 \pm j443$

3. Voltage Control Algorithms

On board a naval ship, it may be more common to require an ARCP inverter to establish and regulate a balanced set of three-phase voltages. Since it is generally required that these be sinusoidal voltages with very little harmonic distortion, the normal PWM output voltages are processed through a passive filter before being applied to a load. In order to illustrate a high-performance scheme involving both feedforward and feedback components, consider the diagram illustrated in Figure 10. Note that the load is once again assumed to consist of a resistor and an inductor. The inverter is coupled to the load through an LC-filter. The governing equations for this network in terms of system variables are given in vector form as

$$-\vec{V}_{ABCn} + L_f \rho \vec{i}_{Lf,abc} + \vec{V}_{L,abc} = 0 \quad (81)$$

$$C_f \rho \vec{V}_{L,abc} = \vec{i}_{Lf,abc} - \vec{i}_{L,abc} = 0 \quad (82)$$

$$-\vec{V}_{L,abc} + R_L \vec{i}_{L,abc} + L_L \rho \vec{i}_{L,abc} = 0 \quad (83)$$

where

$$\vec{V}_{ABCn} = \begin{bmatrix} V_{An} \\ V_{Bn} \\ V_{Cn} \end{bmatrix} \quad (84)$$

$$\vec{V}_{L,abc} = \begin{bmatrix} V_{L,a} \\ V_{L,b} \\ V_{L,c} \end{bmatrix} \quad (85)$$

$$\vec{i}_{L,abc} = \begin{bmatrix} i_{L,a} \\ i_{L,b} \\ i_{L,c} \end{bmatrix} \quad (86)$$

$$\vec{i}_{Lf,abc} = \begin{bmatrix} i_{Lf,a} \\ i_{Lf,b} \\ i_{Lf,c} \end{bmatrix} \quad (87)$$

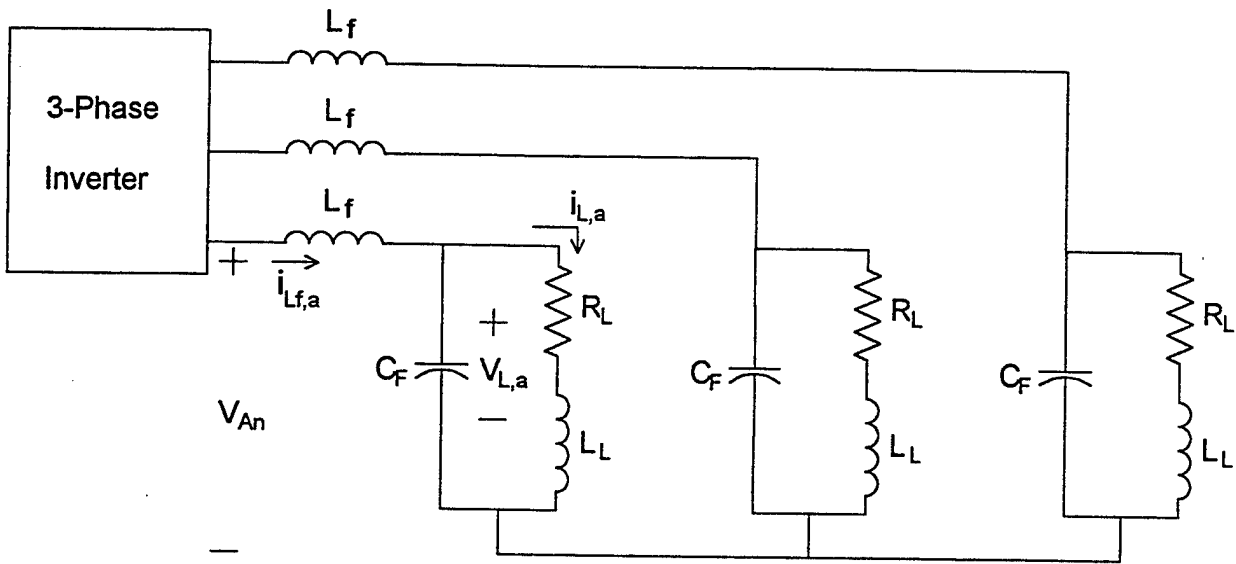


Figure 10. Inverter Voltage Control Output Filter and Load

It has been shown in previous sections that analysis in the Synchronous Reference Frame (SYN-RF) is advantageous in modeling inverter systems while considering only the fundamental quantity. This holds because sinusoids become constants in the SYN-RF implying that all state variables are constants in the steady state. If we consider balanced operation where all zero-sequence variables are identically zero, we can transform (81)-(83) into the SYN-RF and arrive at

$$\rho \, i_{Lf,q}^e = -\omega_e \, i_{Lf,d}^e + \frac{1}{L_f} \, v_{Qn}^e - \frac{1}{L_f} \, v_{L,q}^e \quad (88)$$

$$\rho \, i_{Lf,d}^e = \omega_e \, i_{Lf,q}^e + \frac{1}{L_f} \, v_{Dn}^e - \frac{1}{L_f} \, v_{L,d}^e \quad (89)$$

$$\rho \, v_{L,q}^e = -\omega_e \, v_{L,d}^e + \frac{1}{C_f} \, i_{Lf,q}^e - \frac{1}{C_f} \, i_{L,q}^e \quad (90)$$

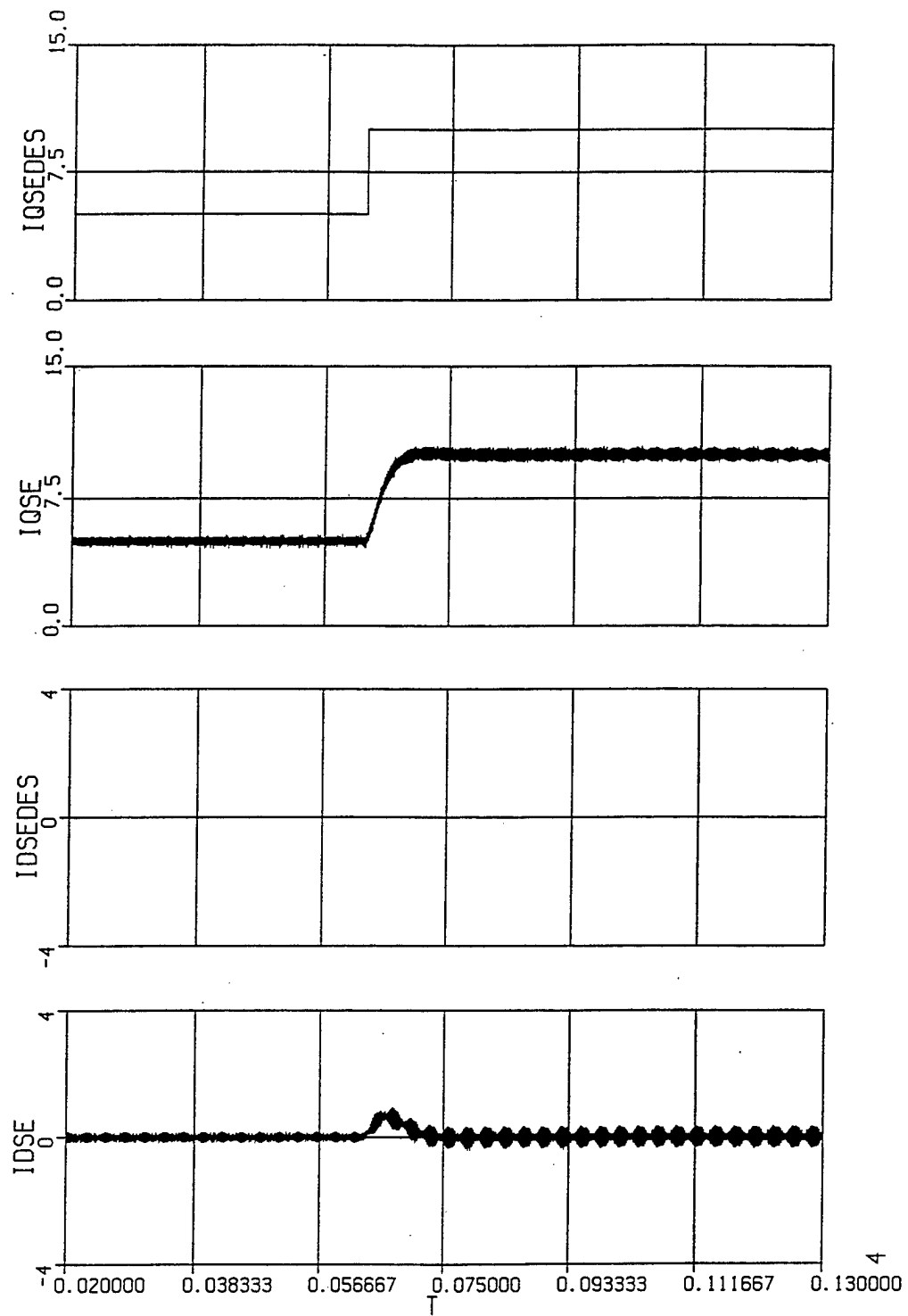


Figure 8. SYN-RF Current Control Waveforms

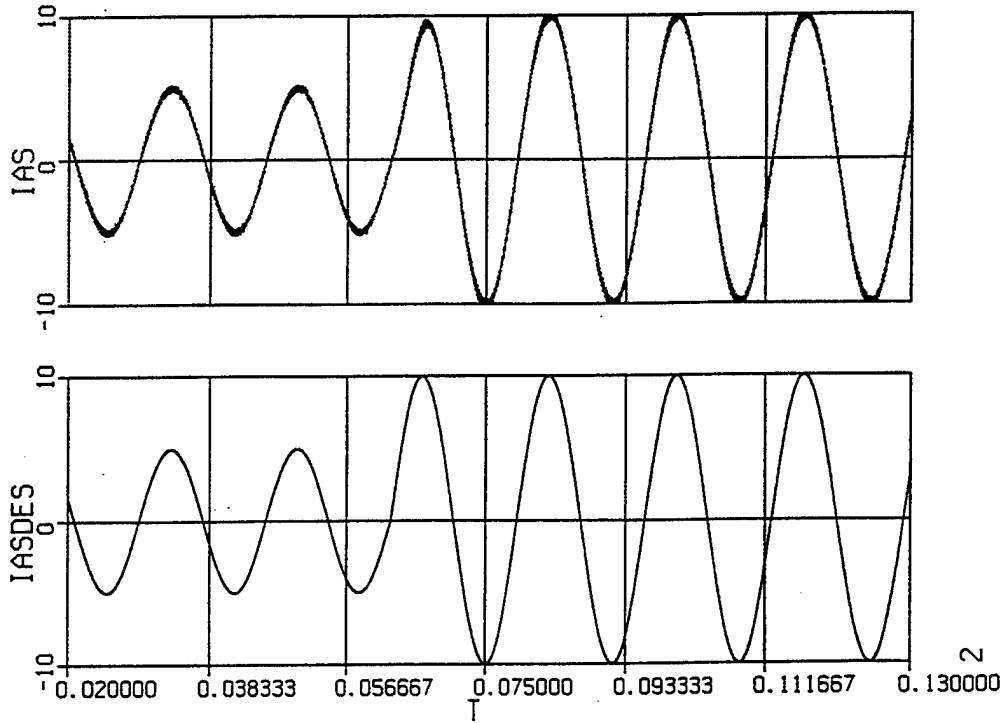


Figure 9. SYN-RF Current Control a-Phase Current Waveforms

$$\rho v_{L,d}^e = \omega_e v_{L,q}^e + \frac{1}{C_f} i_{Lf,d}^e - \frac{1}{C_f} i_{Lf,q}^e \quad (91)$$

$$\rho i_{L,q}^e = -\omega_e i_{L,d}^e + \frac{1}{L_L} v_{L,q}^e - \frac{R_L}{L_L} i_{L,q}^e \quad (92)$$

$$\rho i_{L,d}^e = \omega_e i_{L,q}^e + \frac{1}{L_L} v_{L,d}^e - \frac{R_L}{L_L} i_{L,d}^e \quad (93)$$

Thus, our system inputs are v_{Qn}^e and v_{Dn}^e which are arrived at from manipulating the inverter switching via either STPWM or SVM. In terms of our original quantities, v_{Qn}^e and v_{Dn}^e are the SYN-RF transformed versions of \bar{v}_{ABCn} .

We desire to regulate the output load voltages represented by $v_{L,q}^e$ and $v_{L,d}^e$. Let's assume that we can monitor the instantaneous values of the output voltages ($v_{L,q}^e$ and $v_{L,d}^e$), the output currents ($i_{L,q}^e$ and $i_{L,d}^e$), the filter inductor currents ($i_{Lf,q}^e$ and $i_{Lf,d}^e$), and the input dc voltage (V_{dc}). That is, assume that the appropriate abc-quantities can be sampled and then transformed into the SYN-RF at the front-end of the DSP control implementation. Therefore, assuming balanced operation, the proposed scheme requires seven variables to be sampled.

Before we delve into the control architecture, consider that the desired output voltages assume the following form

$$\begin{bmatrix} v_{L,a}^* \\ v_{L,b}^* \\ v_{L,c}^* \end{bmatrix} = \begin{bmatrix} V_o \cos(\omega_e t) \\ V_o \cos(\omega_e t - \frac{2\pi}{3}) \\ V_o \cos(\omega_e t + \frac{2\pi}{3}) \end{bmatrix} \quad (94)$$

Transforming this balanced set into the SYN-RF yields

$$\begin{bmatrix} v_{L,q}^{e*} \\ v_{L,d}^{e*} \\ v_{L,0}^* \end{bmatrix} = \begin{bmatrix} V_o \\ 0 \\ 0 \end{bmatrix} \quad (95)$$

We can therefore view our setpoint as being $v_{L,q}^{e*}$. Also since the load voltage is across the filter capacitor, it follows that the desired capacitor current is given by

$$\vec{i}_{c,abc}^* = C_f \rho \vec{v}_{L,abc}^* \quad (96)$$

or transforming into the SYN-RF

$$\vec{i}_{c,qd0}^{e*} = C_f \rho \vec{v}_{L,qd0}^{e*} + \begin{bmatrix} \omega_e C_f v_{L,d}^{e*} \\ -\omega_e C_f v_{L,q}^{e*} \\ 0 \end{bmatrix} \quad (97)$$

The proposed control architecture is illustrated in Figure 11. We will first describe the flow qualitatively in order to provide the reader with the basic idea. First, there is an inner fast-acting current control loop surrounded by a slower-acting voltage control loop. The voltage control loop consists of Proportional-Integral (PI) regulators for both the q and d-axis output voltages. The outputs of these regulators provide for transient changes in the commanded filter capacitor currents. The commanded filter capacitor currents also consist of a feedforward term which programs in the required steady-state currents. Next, the load current is added to the capacitor current to establish a commanded value of inductor filter current. The inner current control processes the error between the commanded filter inductor current and the actual filter inductor current to generate q and d-feedback derived signals. The desired inverter output voltages are found by adding the feedback signals to feedforward components, dictated by the commanded capacitor voltages and the voltage drops across the filter inductances. These signals then are either transformed to the STA-RF for SVM or to the abc-realm for STPWM.

Certainly there is nothing trivial about this formulation. Let's step back and walk through it one more time with the aid of the equations.

Step 1. Perturbation signals are derived from the error in the commanded and

actual output load voltages:

$$i_{cap,q}^e = K_{pvq} (v_{L,q}^{e*} - v_{L,q}^e) + K_{ivq} \int (v_{L,q}^{e*} - v_{L,q}^e) dt \quad (98)$$

$$i_{cap,d}^e = K_{pvd} (v_{L,d}^{e*} - v_{L,d}^e) + K_{ivd} \int (v_{L,d}^{e*} - v_{L,d}^e) dt \quad (99)$$

Note from (97) that with the commanded voltage signals constant, the steady-state capacitor filter currents are given by

$$\vec{i}_{c,qd0}^{e*} = \begin{bmatrix} \omega_e C_f v_{L,d}^{e*} \\ -\omega_e C_f v_{L,q}^{e*} \\ 0 \end{bmatrix} \quad (100)$$

Step 2. Incorporate feedforward action to form the desired filter capacitor currents:

$$i_{c,q}^{e*} = i_{cap,q}^e + \omega_e C_f v_{L,d}^{e*} \quad (101)$$

$$i_{c,d}^{e*} = i_{cap,d}^e - \omega_e C_f v_{L,q}^{e*} \quad (102)$$

Thus, $i_{cap,q}^e$ and $i_{cap,d}^e$ "correct" the feedforward components and are necessary to compensate for imprecise knowledge of C_f and for loss mechanisms ignored in the analysis.

Step 3. Form the desired filter inductor currents from the desired filter capacitor currents and the measured load currents (in the SYN-RF):

$$i_{Lf,q}^{e*} = i_{c,q}^{e*} + i_{L,q}^e \quad (103)$$

$$i_{Lf,d}^{e*} = i_{c,d}^{e*} + i_{L,d}^e \quad (104)$$

These signals become inputs to the inner current control.

Step 4. Perturbation signals are derived from the error in the commanded and actual filter inductor currents:

$$v_{fbk,q}^e = K_{pcq} (i_{Lf,q}^{e*} - i_{Lf,q}^e) + K_{icq} \int (i_{Lf,q}^{e*} - i_{Lf,q}^e) dt \quad (105)$$

$$v_{fbk,d}^e = K_{pcd} (i_{Lf,d}^{e*} - i_{Lf,d}^e) + K_{icd} \int (i_{Lf,d}^{e*} - i_{Lf,d}^e) dt \quad (106)$$

Rewriting (88) and (89), we have that

$$v_{Qn}^e = v_{L,q}^e + L_f \rho i_{Lf,q}^e + \omega_e L_f i_{Lf,d}^e \quad (107)$$

$$v_{Dn}^e = v_{L,d}^e + L_f \rho i_{Lf,d}^e - \omega_e L_f i_{Lf,q}^e \quad (108)$$

Thus in the steady state we can ignore the derivative-of-current terms and generate a feedforward component for the desired line-to-neutral voltage across the filter capacitor and

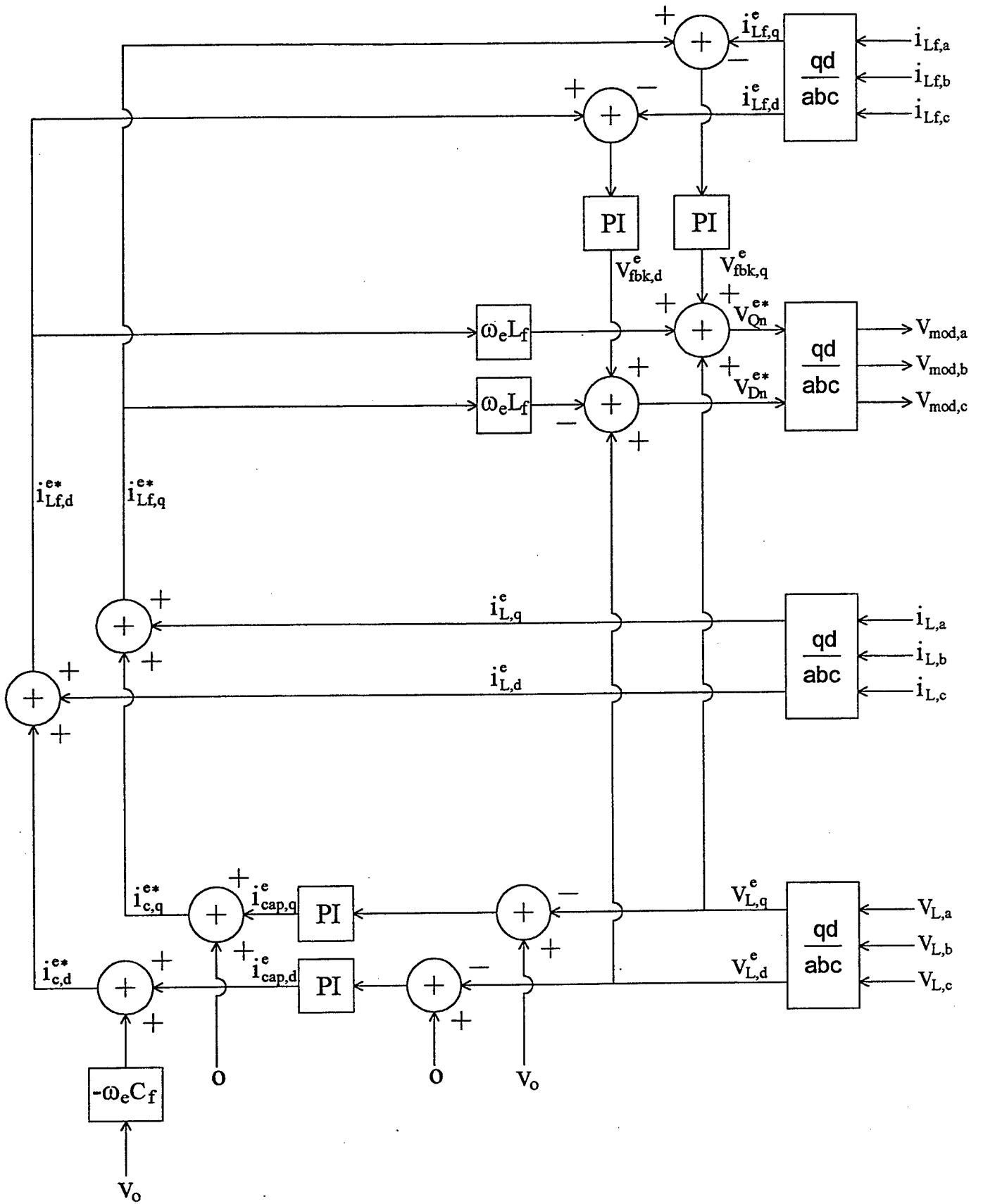


Figure 11. Voltage Control Block Diagram

inductor. We accomplish this by measuring the actual load voltages and using the previously derived commanded filter currents.

Step 5. Form the commanded line-to-neutral voltage across the filter capacitor and inductor from the steady-state feedforward component using the commanded filter inductor currents and the feedback component generated in Step 4:

$$v_{Qn}^{e*} = v_{L,q}^e + \omega_e L_f i_{Lf,d}^{e*} + v_{fbk,q}^e \quad (109)$$

$$v_{Dn}^{e*} = v_{L,d}^e - \omega_e L_f i_{Lf,q}^{e*} + v_{fbk,d}^e \quad (110)$$

Thus, $v_{fbk,q}^e$ and $v_{fbk,d}^e$ "correct" the feedforward components to compensate for uncertainty and non-idealities.

Step 6. Use v_{Qn}^{e*} and v_{Dn}^{e*} to generate the required STPWM or SVM signals. That is, either transform these quantities to abc-quantities for use as modulation signals in STPWM or transform them to STA-RF quantities for application in SVM.

Synthesizing the control gains in a systematic manner is a non-trivial endeavor, though the process can be simplified by making some basic observations and assumptions. The filter inductor current dynamics are given by

$$\rho i_{Lf,q}^e = -\omega_e i_{Lf,d}^e + \frac{1}{L_f} v_{Qn}^e - \frac{1}{L_f} v_{L,q}^e \quad (111)$$

$$\rho i_{Lf,d}^e = \omega_e i_{Lf,q}^e + \frac{1}{L_f} v_{Dn}^e - \frac{1}{L_f} v_{L,d}^e \quad (112)$$

where the actual applied SYN-RF voltages out of the inverter are related to the control signals by the gain G as shown in

$$v_{Qn}^e = G v_{Qn}^{e*} = G (v_{L,q}^e + \omega_e L_f i_{Lf,d}^{e*} + v_{fbk,q}^e) \quad (113)$$

$$v_{Dn}^e = G v_{Dn}^{e*} = G (v_{L,d}^e - \omega_e L_f i_{Lf,q}^{e*} + v_{fbk,d}^e) \quad (114)$$

The dynamics introduced by the current control integral compensators are described by

$$\rho x_{cq}^e = i_{Lf,q}^{e*} - i_{Lf,q}^e \quad (115)$$

$$\rho x_{cd}^e = i_{Lf,d}^{e*} - i_{Lf,d}^e \quad (116)$$

and

$$v_{fbk,q}^e = K_{pcq} (i_{Lf,q}^{e*} - i_{Lf,q}^e) + K_{icq} x_{cq}^e \quad (117)$$

$$v_{fbk,d}^e = K_{pcd} (i_{Lf,d}^{e*} - i_{Lf,d}^e) + K_{icd} x_{cd}^e \quad (118)$$

Therefore, if we choose G in (113)-(114) to be unity and substitute the result into (111)-(112), the filter current dynamics become simply

$$\rho \dot{i}_{Lf,q}^e = -\omega_e \dot{i}_{Lf,d}^e + \omega_e \dot{i}_{Lf,d}^{e*} + \frac{K_{pcq}}{L_f} (\dot{i}_{Lf,q}^{e*} - \dot{i}_{Lf,q}^e) + \frac{K_{icq}}{L_f} x_{cq}^e \quad (119)$$

$$\rho \dot{i}_{Lf,d}^e = \omega_e \dot{i}_{Lf,q}^e - \omega_e \dot{i}_{Lf,q}^{e*} + \frac{K_{pcd}}{L_f} (\dot{i}_{Lf,d}^{e*} - \dot{i}_{Lf,d}^e) + \frac{K_{icd}}{L_f} x_{cd}^e \quad (120)$$

Combining (115)-(116) and (119)-(120) yields the state space description:

$$\rho \begin{bmatrix} \dot{i}_{Lf,q}^e \\ \dot{i}_{Lf,d}^e \\ x_{cq}^e \\ x_{cd}^e \end{bmatrix} = \begin{bmatrix} -\frac{K_{pcq}}{L_f} & -\omega_e & \frac{K_{icq}}{L_f} & 0 \\ \omega_e & -\frac{K_{pcd}}{L_f} & 0 & \frac{K_{icd}}{L_f} \\ -1 & 0 & 0 & 0 \\ 0 & -1 & 0 & 0 \end{bmatrix} \begin{bmatrix} \dot{i}_{Lf,q}^e \\ \dot{i}_{Lf,d}^e \\ x_{cq}^e \\ x_{cd}^e \end{bmatrix} + \begin{bmatrix} \frac{K_{pcq}}{L_f} & \omega_e \\ -\omega_e & \frac{K_{pcd}}{L_f} \\ 1 & 0 \\ 0 & 1 \end{bmatrix} \begin{bmatrix} \dot{i}_{Lf,q}^{e*} \\ \dot{i}_{Lf,d}^{e*} \end{bmatrix} \quad (121)$$

Instead of using trial-and-error, the eigenvalues for (121) may be uniquely specified using the four available gains. To illustrate how this is accomplished, consider the characteristic equation

$$\lambda^4 + \left(\frac{K_{pcq}}{L_f} + \frac{K_{pcd}}{L_f} \right) \lambda^3 + \left(\frac{K_{icq}}{L_f} + \frac{K_{icd}}{L_f} + \frac{K_{pcq}}{L_f} \frac{K_{pcd}}{L_f} + \omega_e^2 \right) \lambda^2 + \left(\frac{K_{icq}}{L_f} \frac{K_{pcd}}{L_f} + \frac{K_{icd}}{L_f} \frac{K_{pcq}}{L_f} \right) \lambda + \frac{K_{icq}}{L_f} \frac{K_{icd}}{L_f} = 0 \quad (122)$$

Equation (122) can be compared with a desired characteristic equation formulated from the desired eigenvalue locations. Assume that the desired equation is given by

$$\lambda^4 + d_3 \lambda^3 + d_2 \lambda^2 + d_1 \lambda + d_0 = 0 \quad (123)$$

If we let $x_1 = \frac{K_{pcq}}{L_f}$, $x_2 = \frac{K_{pcd}}{L_f}$, $x_3 = \frac{K_{icq}}{L_f}$, and $x_4 = \frac{K_{icd}}{L_f}$, then we can coefficient match between (122) and (123) and formulate the following set of four nonlinear equations in four unknowns.

$$f_1 = x_1 + x_2 - d_3 \quad (124)$$

$$f_2 = x_1 x_2 + x_3 + x_4 + \omega_e^2 - d_2 \quad (125)$$

$$f_3 = x_1 x_4 + x_2 x_3 - d_1 \quad (126)$$

$$f_4 = x_3 x_4 - d_0 \quad (127)$$

where we seek to find values of 'x' where each function 'f' is equal to zero. We can solve this problem by using a Newton-Raphson approach where we define the vector-valued nonlinear vector-function

$$\vec{f} = \begin{bmatrix} f_1 \\ f_2 \\ f_3 \\ f_4 \end{bmatrix} \quad (128)$$

our vector of unknowns

$$\vec{x} = \begin{bmatrix} x_1 \\ x_2 \\ x_3 \\ x_4 \end{bmatrix} \quad (129)$$

and the Jacobian matrix

$$\bar{F} = \begin{bmatrix} 1 & 1 & 0 & 0 \\ x_{2o} & x_{1o} & 1 & 1 \\ x_{4o} & x_{3o} & x_{2o} & x_{1o} \\ 0 & 0 & x_{4o} & x_{3o} \end{bmatrix} \quad (130)$$

where x_{1o} through x_{4o} represent the current guesses of the unknowns x_1 through x_4 . We can solve for the unknowns by iteratively applying

$$\vec{x}_{n+1} = \vec{x}_n - \bar{F}(\vec{x}_n)^{-1} \bar{f}(\vec{x}_n) \quad (131)$$

An example will be illustrated at the end of this section.

The voltage loop may then be designed by assuming that the current dynamics are much faster than the voltage control dynamics so that

$$i_{Lf,q}^e = i_{Lf,q}^{e*} \quad (132)$$

$$i_{Lf,d}^e = i_{Lf,d}^{e*} \quad (133)$$

The dynamics introduced by the voltage control integral compensators are described by

$$\rho x_{vq}^e = v_{L,q}^{e*} - v_{L,q}^e \quad (134)$$

$$\rho x_{vd}^e = v_{L,d}^{e*} - v_{L,d}^e \quad (135)$$

The current loop being assumed ideal allows us to rewrite (90)-(91) as

$$\rho v_{L,q}^e = -\omega_e v_{L,d}^e + \frac{1}{C_f} i_{Lf,q}^{e*} - \frac{1}{C_f} i_{L,q}^e \quad (136)$$

$$\rho v_{L,d}^e = \omega_e v_{L,q}^e + \frac{1}{C_f} i_{Lf,d}^{e*} - \frac{1}{C_f} i_{L,d}^e \quad (137)$$

which can be reduced upon inspection of the control algorithm since

$$i_{Lf,q}^{e*} = i_{L,q}^e + \omega_e C_f v_{L,d}^e + K_{pvq} (v_{L,q}^{e*} - v_{L,q}^e) + K_{ivq} x_{vq}^e \quad (138)$$

$$i_{Lf,d}^{e*} = i_{L,d}^e - \omega_e C_f v_{L,q}^e + K_{pvd} (v_{L,d}^{e*} - v_{L,d}^e) + K_{ivd} x_{vd}^e \quad (139)$$

Thus, substituting (138)-(139) into (136)-(137) then augmenting with equations (134)-(135), we arrive at One can quickly ascertain that the system matrix is identical in form to the system matrix in (121). Therefore, the eigenvalue assignment problem is the same: solve an identical set of four nonlinear equations using the previously described Newton-Raphson algorithm.

$$\rho \begin{bmatrix} v_{L,q}^e \\ v_{L,d}^e \\ x_{vq}^e \\ x_{vd}^e \end{bmatrix} = \begin{bmatrix} -\frac{K_{pvq}}{C_f} & -\omega_e & \frac{K_{ivq}}{C_f} & 0 \\ \omega_e & -\frac{K_{pvd}}{C_f} & 0 & \frac{K_{ivd}}{C_f} \\ -1 & 0 & 0 & 0 \\ 0 & -1 & 0 & 0 \end{bmatrix} \begin{bmatrix} v_{L,q}^e \\ v_{L,d}^e \\ x_{vq}^e \\ x_{vd}^e \end{bmatrix} + \begin{bmatrix} \frac{K_{pvq}}{C_f} & \omega_e \\ -\omega_e & \frac{K_{pvd}}{C_f} \\ 1 & 0 \\ 0 & 1 \end{bmatrix} \begin{bmatrix} v_{L,q}^{e*} \\ v_{L,d}^{e*} \end{bmatrix} \quad (140)$$

Next, let's illustrate the procedure with a design example. Consider the parameters listed in Table 12.

Table 12. Parameters for Inverter Voltage Control Example

R_L	L_L	C_f	L_f
25 Ω	20 mH	0.1 mF	10.1 mH
V_{dc}	A_t	f_s	ω_e
850 V	425 V	5 kHz	377 rad/sec

A set of MATLAB script files were written to perform the calculations. First, the four current control eigenvalues were specified. For convenience, all four were placed at the same location, comfortably in the left-half-plane, yet not too far to interfere with the switching frequency $2\pi 5000$ rad/sec.

$$\lambda_{1,2,3,4} = -3000$$

Next, the current gains were found by applying the Newton-Raphson algorithm. The voltage-loop eigenvalues were then specified. We chose to locate them a factor of five times closer to the $j\omega$ axis so that the current-control dynamics would be faster. In particular,

$$\lambda_{5,6,7,8} = -600$$

The voltage-loop gains were then found by applying the Newton-Raphson algorithm. Both sets of gains are recorded in Table 13. The eigenvalues of the overall system were then established without using any loop-interaction approximation yielding the following results:

$$\begin{aligned} &-2649 \pm j2699 \\ &-2472 \pm j1926 \\ &-825 \pm j415 \\ &-459 \pm j100 \\ &-653 \\ &-1040 \end{aligned}$$

Note, the actual eigenvalue locations are somewhat different than the desired locations.

This occurs because of the approximation that the current loop is infinitely faster than the voltage loop. Had we located the current-control eigenvalues further into the left-half-plane, the resultant eigenvalues would more closely track the desired values. Nonetheless, the above concentration is approximately where we want them and so we should expect acceptable transient response (though there are some zeros near to the $j\omega$ axis which tend to increase the overshoot).

Table 13. Multi-Loop Control Gains

K_{pcq} 56.79	K_{icq} 90900.0	K_{pcd} 64.41	K_{icd} 90900.0
K_{pvq} 0.0823	K_{ivq} 36.0	K_{pvd} 0.1577	K_{ivd} 36.0

The next step in the procedure is to validate the design using a detailed ACSL simulation. One of the previous programs was modified to depict the described algorithm.

Initially, it is assumed that the filter capacitors are de-energized. As a result, the commanded voltage is ramped up from 0V to 360V, over a 0.1sec interval. That is, $v_{L,q}^{e*}$ is ramped from 0V to 360V while $v_{L,d}^{e*}$ is held at zero. The 360V corresponds to the peak phase voltage; therefore, we are ramping up to a rms line-to-neutral voltage of 255V or an rms line-to-line voltage of 440V. The 0.1sec is arbitrary but is required to limit the current drawn from the inverter and helps maintain the inverter in the linear modulation range. At 0.15sec, the load is step-changed from 25Ω down to 10Ω . The plots illustrated include the a-phase commanded and actual phase voltage, the q and d-load voltages, the filter and load currents, and the a-phase PWM modulating signal. Note that the integral action on the qd-load voltages guarantees zero steady-state error. Also, the fast-acting inner current loop together with the feedforward action guarantees rapid response to the load change and only a minimal voltage transient. The transient persists for about 10msec as anticipated with the dominant eigenvalue located with a real part of approximately -400 . The q-load voltage decreases by about 4V while the d-load voltage decreases by about 2V resulting in less than a 5V decrease in the line-to-neutral voltage, hardly even noticeable in the figure. As is illustrated, the voltages are very sinusoidal and the modulation signal remains predominantly in the linear modulation range. In addition, it is important to recognize that the control design was performed independent of the load parameters. The gains were selected based solely on knowing the filter parameters and the desired output frequency. The ultimate selection of the inverter output filter components will be dictated by stability issues and the desired level of harmonics.

The algorithm may be summarized as follows.

1. The a and b-phase load voltages, load currents and filter currents are measured with appropriate sensors.
2. The q and d-synchronous reference frame quantities are then calculated. For example for the load voltage, this may be shown in two steps (first going to the stationary reference frame)

$$v_{L,q}^s = v_{L,a}$$
$$v_{L,d}^s = -\frac{1}{\sqrt{3}} v_{L,a} - \frac{2}{\sqrt{3}} v_{L,b}$$

(Then to the synchronous reference frame)

$$v_{L,q}^e = v_{L,q}^s \cos\theta_e - v_{L,d}^s \sin\theta_e$$
$$v_{L,d}^e = v_{L,q}^s \sin\theta_e + v_{L,d}^s \cos\theta_e$$

where θ_e is the angle of the SYN-RF that varies at ω_e . This angle or the trigonometric functions may be evaluated by table lookup as described by Floodeen.

3. The commanded load voltage components are initialized wherein a ramp algorithm may be used to initiate startup.
4. Equations (98)-(99) and (101)-(110) are programmed using the trapezoidal approximation for the integration function as described by both Hanson and Floodeen.
5. The appropriate duty cycle signals are formulated using either STPWM or SVM.

Thus far, current control and a voltage control algorithm has been considered for the ARCP inverter outer control. The final element of this report will document an induction machine start-up and speed control algorithm that will build on the previous presentation.

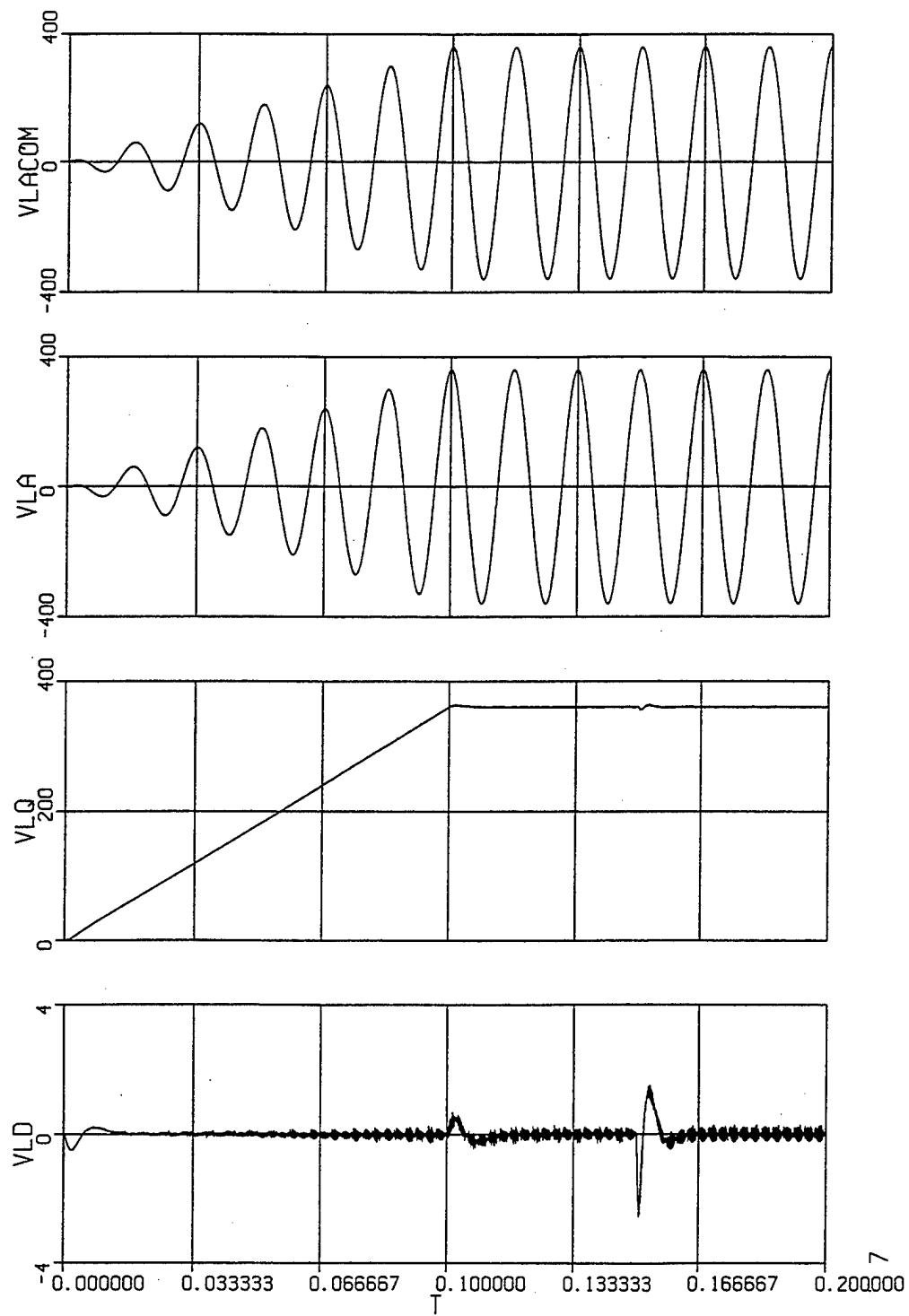


Figure 12. Voltage Waveforms for the Voltage Control Example

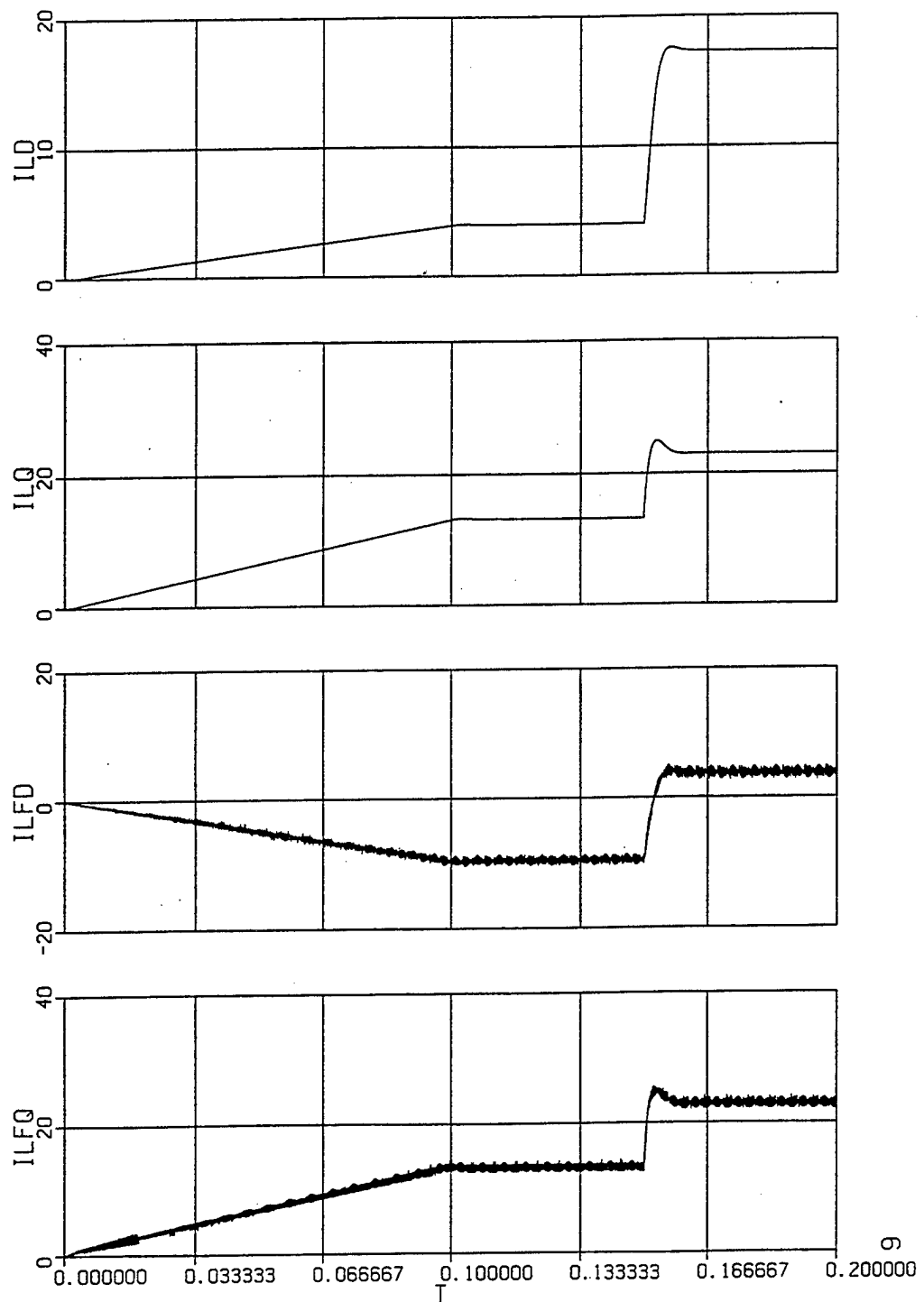


Figure 13. Current Waveforms for the Voltage Control Example

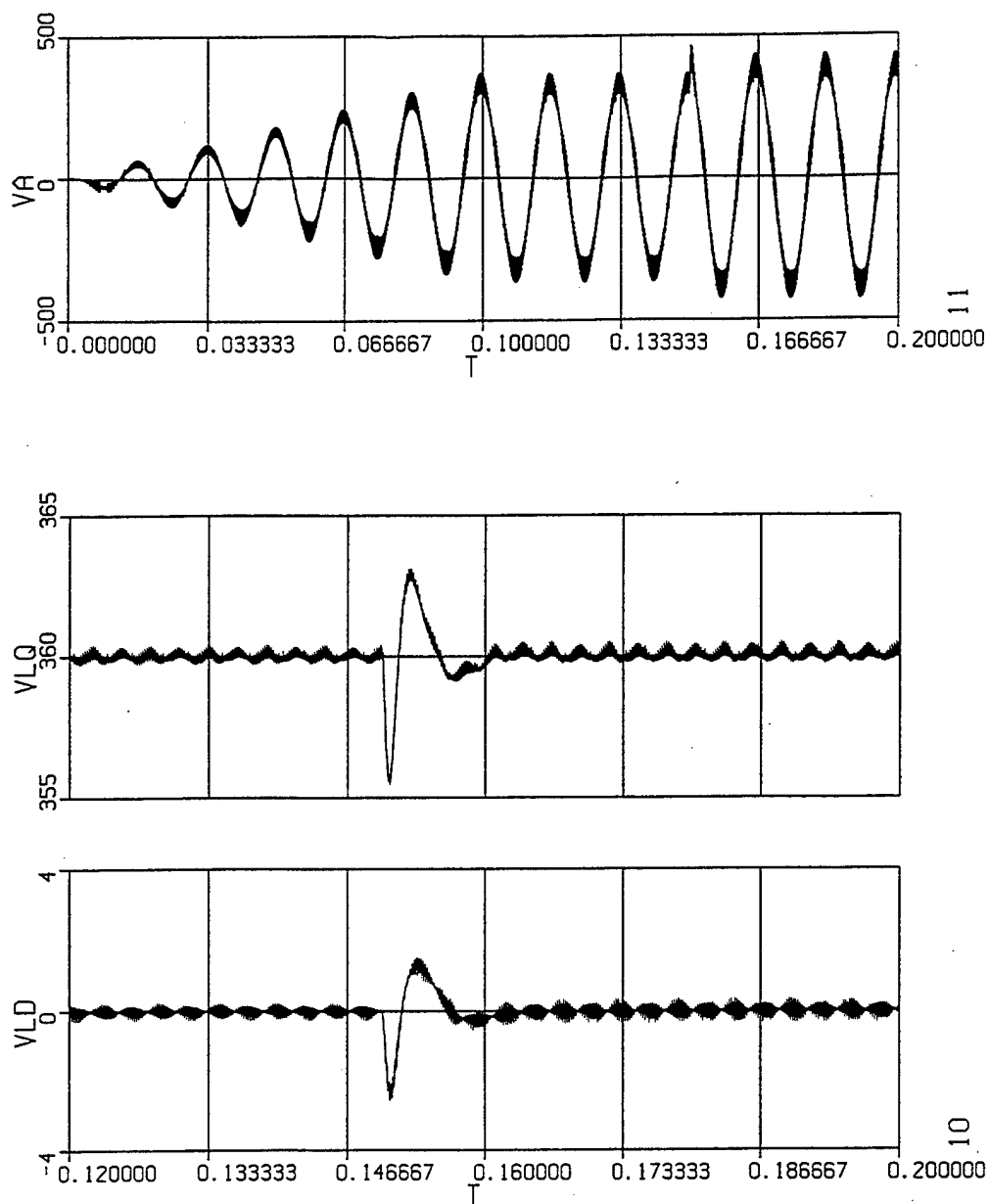


Figure 14. Blowup of the Voltage Transient

B. Induction Machine Startup Control

On board ship, each electrical zone will have numerous electric machine loads that in turn power compressors, blowers, fans and other actuators. In DC ZEDS, most of these machines are induction motors and all must be energized by SSIMs, providing variable-voltage variable-frequency control opportunities. It is well understood that Direct-On-Line (DOL) starting of an induction machine typically results in a large in-rush current. One approach to limiting the starting current is to reduce the applied voltages at rated frequency. This has the disadvantage of also reducing the available starting torque, which may or may not be an issue for the load. By varying both the voltage amplitude and the applied frequency, the machine stator current can be limited without compromising the starting torque.

In this section, we wish to propose two approaches to implementing an induction machine startup control that allow the user to ramp up the speed of the machine to a desired level and have that speed regulated in the presence of any load disturbances. In addition, it is desired to automatically limit the current impressed through the SSIM semiconductor switches and avoid the large surge of current from the dc bus when the machine is starting.

Both approaches proffered use a multi-loop design where a slow speed-control loop is wrapped around a fast-acting current-control loop. Since the machine torque is intimately related to the stator currents, we may view the outer loop as generating a commanded torque signal and the inner loop as programming the currents necessary to realize that desired torque. The current control operates in a manner analogous to the approach outlined in a previous section. The outer speed control loop develops commanded values of frequency and current amplitude to indirectly control the torque and regulate the magnetic flux. If the machine flux is not held below the saturation level of the iron, additional losses are introduced, harmonic distortion is increased, and airborne noise and vibration may become unacceptable.

1. Constant Air-Gap Flux Control

The standard per-phase steady-state equivalent circuit of the induction machine is illustrated in Figure 15. The parameters r_s and r_r' are the resistances of the stator winding and the referred rotor winding (referred to have the same number of turns as the stator). The reactances X_{ls} and X_{lr}' are associated with the leakage flux produced by the stator and referred rotor windings. The reactance X_m accounts for the production of the flux which couples both the stator and the rotor, the air-gap flux. The resistance R_c is oftentimes inserted into the circuit to account for core losses arising from hysteresis and eddy currents. The current flowing down through the center branch is termed the magnetizing

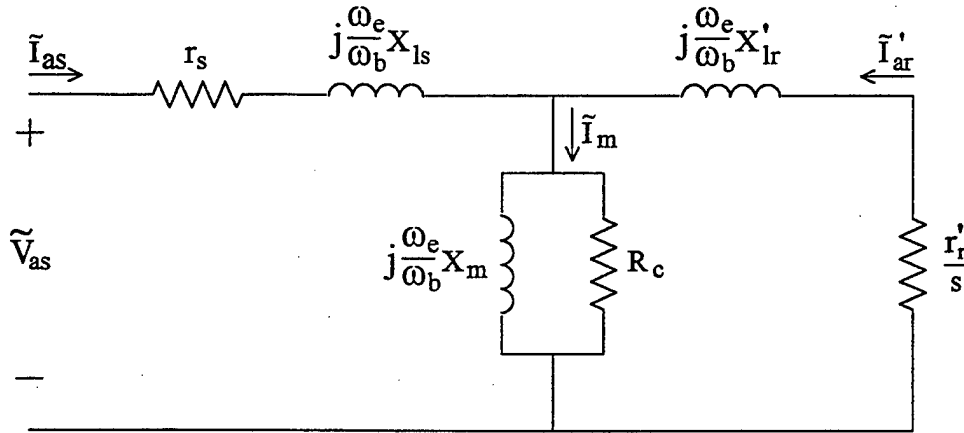


Figure 15. Per-Phase Steady-State Equivalent Induction Machine Circuit

current and is directly related to the air-gap flux. If we assume that our fast-acting current control resembles a current source (the electrical dynamics are much faster than the mechanical dynamics), then the stator phase current \tilde{I}_{as} is fixed and neither r_s or X_{ls} will effect its value. How that current divides into magnetizing current and rotor-referred current is dictated by the machine slip

$$s = \frac{\omega_e - \omega_r}{\omega_e} = \frac{\frac{2}{P} \omega_e - \omega_{rm}}{\frac{2}{P} \omega_e} \quad (141)$$

where ω_e is the fundamental frequency of the applied \tilde{I}_{as} , ω_{rm} is the actual rotor speed in radians/sec, and ω_r is the rotor electrical speed which is related to ω_{rm} by the number of pole pairs, $\frac{P}{2}$.

For small values of slip, the rotor branch impedance is large and thus most of the stator current proceeds down the magnetizing branch. Therefore, since rated magnetizing current is typically much smaller than rated stator current, a moderate amplitude of \tilde{I}_{as} has the potential of saturating the machine iron. As a result, we must ensure that for a given operating speed and applied frequency that the appropriate amplitude of current is applied. The magnetizing current is related to the stator current by

$$\tilde{I}_m = \frac{\frac{r_r'}{s} + j \frac{\omega_e}{\omega_b} X_{lr}'}{\frac{r_r'}{s} + j \frac{\omega_e}{\omega_b} X_{rr}'} \tilde{I}_{as} \quad (142)$$

where

$$X_{rr}' = X_m + X_{lr}' \quad (143)$$

If we constrain operation to occur at rated magnetizing current, $\tilde{I}_m = \tilde{I}_{m, \text{rat}}$, then

$$\text{mag}(\tilde{I}_{m, \text{rat}})^2 = \frac{(\frac{r_r'}{s})^2 + (\frac{\omega_e}{\omega_b} X_{lr}')^2}{(\frac{r_r'}{s})^2 + (\frac{\omega_e}{\omega_b} X_{rr}')^2} \text{mag}(\tilde{I}_{as})^2 \quad (144)$$

dividing each term by $(\frac{\omega_e}{\omega_b})^2$ and defining

$$\omega_{sln} = s \frac{\omega_e}{\omega_b} = \frac{\omega_e - \omega_r}{\omega_e} \frac{\omega_e}{\omega_b} = \frac{\omega_e - \omega_r}{\omega_b} = \frac{\omega_{sl}}{\omega_b} \quad (145)$$

where ω_{sln} is the normalized slip frequency yields

$$\text{mag}(\tilde{I}_{m, \text{rat}})^2 = \frac{(\frac{r_r'}{\omega_{sln}})^2 + (X_{lr}')^2}{(\frac{r_r'}{\omega_{sln}})^2 + (X_{rr}')^2} \text{mag}(\tilde{I}_{as})^2 \quad (146)$$

which can be rearranged to solve for the required stator current amplitude

$$\text{mag}(\tilde{I}_{as}) = \sqrt{\frac{(X_{rr}' \omega_{sl})^2 + (r_r' \omega_b)^2}{(X_{lr}' \omega_{sl})^2 + (r_r' \omega_b)^2}} \text{mag}(\tilde{I}_{m, \text{rat}}) \quad (147)$$

Therefore given the rated magnetizing current of the machine, the applied electrical frequency ω_e and the rotor electrical angular velocity ω_r , we can establish the required stator current. This relationship will figure predominately in the proposed control strategy. Further it can be shown that while operating at rated flux, the developed torque is directly related to the slip frequency. In particular,

$$T_e = 3 \frac{P}{2} \frac{X_m^2}{\omega_b} \frac{r_r' s \omega_{en}}{r_r'^2 + (X_{lr}' s \omega_{en})^2} \text{mag}(\tilde{I}_{m, \text{rat}})^2 \quad (148)$$

where

$$\omega_{en} = \frac{\omega_e}{\omega_b} \quad (149)$$

For $s \omega_{en}$ small, (148) reduces to

$$T_e = 3 \frac{P}{2} \frac{X_m^2}{\omega_b} \frac{s \omega_{en}}{r_r'} \text{mag}(\tilde{I}_{m, \text{rat}})^2 \quad (150)$$

But since $s\omega_{en} = \frac{\omega_e - \omega_r}{\omega_b}$, it follows then that the torque is approximately proportional to the slip frequency $\omega_e - \omega_r$ for values up to rated torque when the air-gap flux is held constant.

Thus, we have a mechanism for achieving speed control. The outer speed control loop develops a commanded slip frequency signal which directly controls the torque. By sensing the actual rotor speed, this signal can be added to the slip frequency signal to derive the required fundamental frequency of the inverter modulating signals. In addition, the commanded slip frequency can be used together with (147) to specify the amplitude of the stator current required to maintain the air-gap flux at its rated level.

Consider the block diagram illustrated in Figure 16. A commanded slip frequency signal is established by the outer speed control loop. The rotor electrical angular velocity is added to this signal to derive the desired ω_e^* . In addition, ω_{sl}^* is then used to establish the proper stator phase current amplitude to guarantee rated air-gap flux. This peak amplitude is then allocated into i_{qs}^{e*} and i_{ds}^{e*} . The inner current control loop then forces the actual current to track these desired values. The maximum torque, at rated air-gap flux, occurs at

$$\omega_{sl,max} = \omega_b \frac{r_r'}{X_{lr}'} \quad (151)$$

Therefore we can maintain the torque on the negative-sloped portion of the torque versus speed characteristic by imposing this limit on the commanded slip frequency signal. In general, we would probably specify a lower value so as to limit the amplitude of the commanded currents out of the inverter.

Let's consider how a dynamic plays out. Consider a step increase in the commanded rotor speed. The output signal of the speed controller, ω_{sl}^* , saturates corresponding to a demand of maximum torque. This is achieved by commanding the appropriate maximum value of current. As the current control quickly establishes the required current, the developed torque accelerates the rotor and the speed error decreases. Eventually, ω_{sl}^* comes off the limit, the demanded stator current amplitude is reduced, and the developed torque decreases until steady state is achieved.

The control requires that two stator currents be sensed for the inner current control and that a rotor speed signal be derived for the outer loop calculations. The bounds on the commanded slip frequency and the associated commanded current can be adjusted to appropriately limit the current being demanded out of the inverter.

The above control was implemented for a 4-pole, $\frac{1}{4}$ horsepower squirrel-cage induction machine in the laboratory at NPS. The machine has a rated rms phase voltage of 120V, rated rms phase current of 1.2A, and a rated speed of 1670rpm. The parameters of

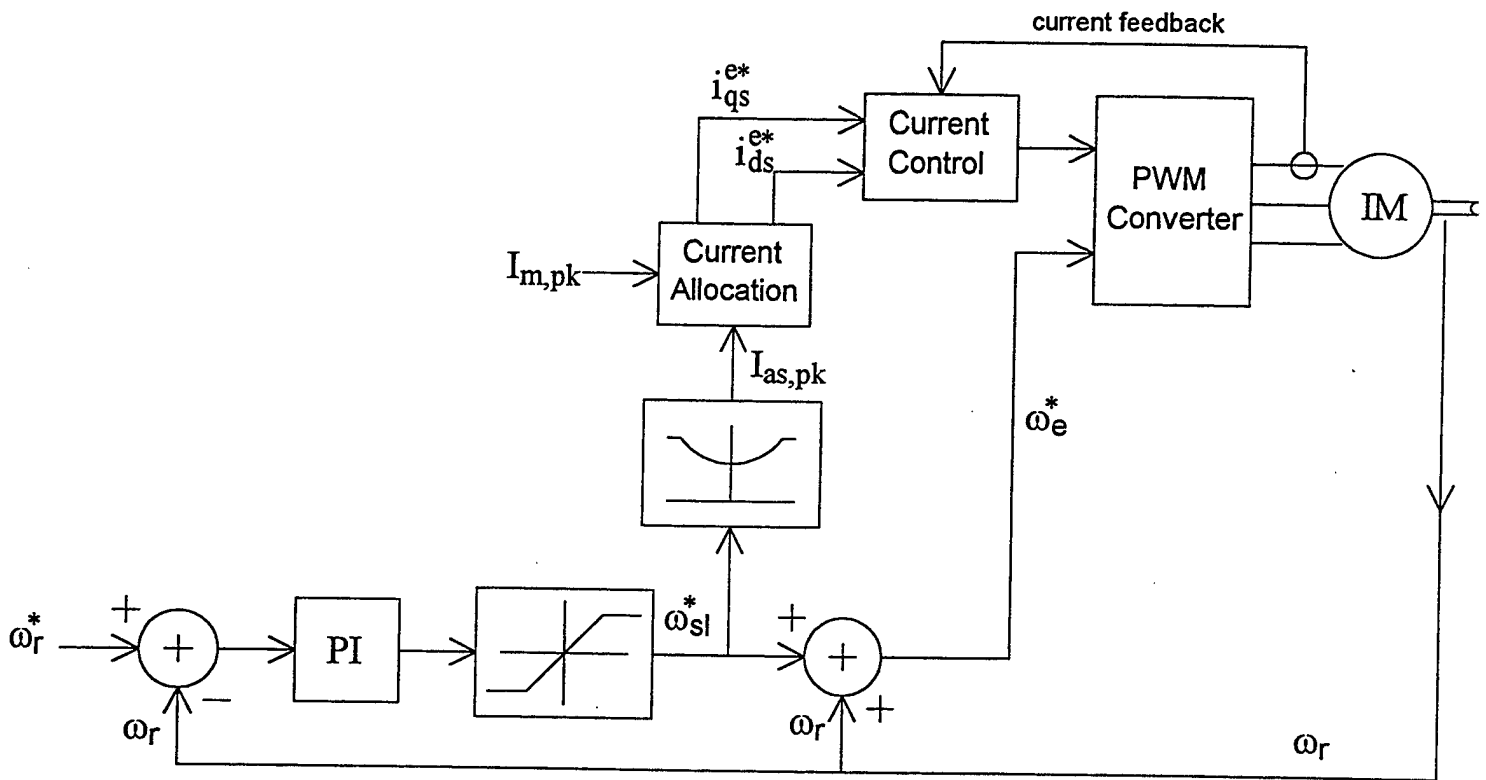


Figure 16. Constant Air-Gap Flux Induction Machine
Speed Control Block Diagram

the machine as determined by resistance measurements, no-load and blocked-rotor tests are summarized in the following table.

Table 14. NPS Induction Machine Parameters

$r_s = 11.78 \Omega$	$X_{ls} = 10.84 \Omega$	$X_m = 149.0 \Omega$
$r_r' = 8.83 \Omega$	$X_{lr}' = 10.84 \Omega$	$R_c = 2097 \Omega$
$P = 4$	$J = 0.0024 \text{ kg/m}^2$	$B = 0.001 \text{ N-m-sec}$

In order to understand how the various control gains can be analytically determined, we need to set forth the modeling equations for the induction machine in the synchronous reference frame.

$$\frac{d}{dt} i_{qs}^e = -c_1 i_{qs}^e - \omega_e i_{ds}^e + c_2 \psi_{qr}'^e - c_3 \omega_r \psi_{dr}'^e + c_4 v_{qs}^e \quad (152)$$

$$\frac{d}{dt} i_{ds}^e = \omega_e i_{qs}^e - c_1 i_{ds}^e + c_3 \omega_r \psi_{qr}'^e + c_2 \psi_{dr}'^e + c_4 v_{ds}^e \quad (153)$$

$$\frac{d}{dt} \psi_{qr}'^e = c_6 i_{qs}^e - c_5 \psi_{qr}'^e - (\omega_e - \omega_r) \psi_{dr}'^e \quad (154)$$

$$\frac{d}{dt} \psi_{dr}'^e = c_6 i_{ds}^e + (\omega_e - \omega_r) \psi_{qr}'^e - c_5 \psi_{dr}'^e \quad (155)$$

$$\frac{d}{dt} \omega_r = -c_7 \omega_r + c_8 i_{qs}^e \psi_{dr}'^e - c_8 i_{ds}^e \psi_{qr}'^e - c_9 T_L \quad (156)$$

where the parameter-dependent constants c_1 through c_9 are given by

$$c_1 = \frac{\omega_b}{D} \left[\frac{r_r' X_m^2}{X_{rr}'} + r_s X_{rr}' \right] \quad (157)$$

$$c_2 = \frac{r_r' \omega_b X_m}{D X_{rr}'} \quad (158)$$

$$c_3 = \frac{X_m}{D} \quad (159)$$

$$c_4 = \frac{X_{rr}' \omega_b}{D} \quad (160)$$

$$c_5 = \frac{r_r' \omega_b}{X_{rr}'} \quad (161)$$

$$c_6 = \frac{r_r' \omega_b X_m}{X_{rr}'} \quad (162)$$

$$c_7 = \frac{B}{J} \quad (163)$$

$$c_8 = \frac{3 P^2 X_m}{8 J \omega_b X_{rr}} \quad (164)$$

$$c_9 = \frac{P}{2J} \quad (165)$$

The interconnection of the synchronous reference frame current control and STPWM to the induction machine representation is accomplished in a manner similar to that described previously. In particular, the integral-action in the current compensators introduce the following dynamic equations

$$\frac{d}{dt} x_q^e = i_{qs}^{e*} - i_{qs}^e \quad (166)$$

$$\frac{d}{dt} x_d^e = i_{ds}^{e*} - i_{ds}^e \quad (167)$$

and the induction machine input voltages are then given by

$$v_{qs}^e = K_{pwm} K_{pq} (i_{qs}^{e*} - i_{qs}^e) + K_{pwm} K_{iq} x_q^e \quad (168)$$

$$v_{ds}^e = K_{pwm} K_{pd} (i_{ds}^{e*} - i_{ds}^e) + K_{pwm} K_{id} x_d^e \quad (169)$$

where K_{pwm} is the gain of the PWM modulator which, in the linear range, is given by

$$K_{pwm} = \frac{V_{dc}}{2 A_t} \quad (170)$$

Here we have once again assumed, for analysis purposes, that the fundamental inverter output voltages dominate in writing (168) and (169). The outer speed control loop contributes the following dynamic equation

$$\frac{d}{dt} x_s = \omega_r^* - \omega_r \quad (171)$$

and the output equation

$$\omega_{sl}^* = K_{ps} (\omega_r^* - \omega_r) + K_{is} x_s \quad (172)$$

The gain of the block implementing the relationship between the commanded slip frequency and the commanded stator current amplitude may be approximated by the following,

$$K_1 = \frac{I_{as,max} - I_{m,rat}}{\omega_{sl,lim}} \quad (173)$$

Before developing expressions used to determine feedback gains, let's consider how $I_{as,pk}$ may be employed by the inner current control. Recall, the inner current control utilizes the inputs i_{qs}^{e*} and i_{ds}^{e*} . We could simply set one equal to zero and set the other equal to $I_{as,pk}$. The dynamic that results, however, is unacceptable. For instance, if we set i_{ds}^{e*} equal to zero, then i_{qs}^{e*} would be responsible for both maintaining constant air-gap flux

and adjusting the electromagnetic torque. A better approach, somewhat mimicking what is done in vector control, would be to use i_{ds}^{e*} to establish a baseline value of air-gap flux and use i_{qs}^{e*} to control the torque. This may be accomplished by setting

$$i_{ds}^{e*} = I_{m, \text{rat}, \text{pk}} \quad (174)$$

$$i_{qs}^{e*} = \sqrt{I_{as, \text{pk}}^2 - i_{ds}^{e*2}} \quad (175)$$

The modeling equations described above are nonlinear. In order to investigate operating point stability, we must linearize the equations. Upon noting that,

$$\Delta \omega_{sl}^* = K_{ps}(\Delta \omega_r^* - \Delta \omega_r) + K_{is} \Delta x_s \quad (176)$$

where Δ indicates a perturbation quantity away from an assigned operating point. It follows that

$$\Delta \omega_e = \Delta \omega_{sl}^* + \Delta \omega_r \quad (177)$$

Also, noting that we may approximate our nonlinear relationship between the commanded slip and desired stator current amplitude as

$$I_{as, \text{pk}} = K_1 \omega_{sl}^* \quad (178)$$

Therefore,

$$\Delta I_{as, \text{pk}} = K_1 \Delta \omega_{sl}^* \quad (179)$$

Finally, since our expression for i_{qs}^{e*} is nonlinear, linearizing it yields

$$\Delta i_{qs}^{e*} = \frac{I_{as, \text{pk}0}}{\sqrt{I_{as, \text{pk}0}^2 - i_{ds0}^{e*2}}} \Delta I_{as, \text{pk}} = K_2 \Delta I_{as, \text{pk}} \quad (180)$$

where $I_{as, \text{pk}0}$ is the peak value of the stator current at the selected operating point. Therefore, linearizing the machine equations and substituting the above results, we arrive at the following model:

$$\frac{d}{dt} \Delta \vec{x}_{im1} = A_{im1} \Delta \vec{x}_{im1} + B_{im1} \Delta \vec{u}_{im1} \quad (181)$$

$$A_{im1} = \begin{bmatrix} -d_1 & -\omega_{e0} & c_2 & -c_3 \omega_{r0} & a_1 & d_2 & 0 & a_3 \\ \omega_{e0} & -d_4 & c_3 \omega_{r0} & c_2 & a_2 & 0 & d_5 & K_{is} i_{qso}^{e*} \\ c_6 & 0 & -c_5 & -\omega_{e0} + \omega_{r0} & K_{ps} \psi_{dro}'^{e*} & 0 & 0 & -K_{is} \psi_{dro}'^{e*} \\ 0 & c_6 & \omega_{e0} - \omega_{r0} & -c_5 & -K_{ps} \psi_{qro}'^{e*} & 0 & 0 & K_{is} \psi_{qro}'^{e*} \\ c_8 \psi_{dro}'^{e*} & -c_8 \psi_{qro}'^{e*} & -c_8 i_{dso}^{e*} & c_8 i_{qso}^{e*} & -c_7 & 0 & 0 & 0 \\ -1 & 0 & 0 & 0 & K_1 K_2 K_{ps} & 0 & 0 & K_1 K_2 K_{is} \\ 0 & -1 & 0 & 0 & 0 & 0 & 0 & 0 \\ 0 & 0 & 0 & 0 & -1 & 0 & 0 & 0 \end{bmatrix} \quad (182)$$

$$\Delta \vec{x}_{im1} = \left[\Delta i_{qs}^e \quad \Delta i_{ds}^e \quad \Delta \psi_{qr}'^e \quad \Delta \psi_{dr}'^e \quad \Delta \omega_r \quad \Delta x_q^e \quad \Delta x_d^e \quad \Delta x_s^e \right]^t \quad (184)$$

$$B_{im1} = \begin{bmatrix} -i_{dso}^e K_{ps} + d_3 K_1 K_2 K_{ps} & 0 \\ i_{qso}^e K_{ps} & 0 \\ -\psi_{dro}^{'e} K_{ps} & 0 \\ \psi_{qro}^{'e} K_{ps} & 0 \\ 0 & -c_9 \\ K_1 K_2 K_{ps} & 0 \\ 0 & 0 \\ 1 & 0 \end{bmatrix} \quad (183)$$

$$\Delta \vec{u}_{im1} = \begin{bmatrix} \Delta \omega_r^* & \Delta T_L \end{bmatrix}^t \quad (185)$$

where the additional constants are given by

$$d_1 = c_1 + K_{pwm} K_{pq} c_4 \quad (186)$$

$$d_2 = K_{pwm} K_{iq} c_4 \quad (187)$$

$$d_3 = K_{pwm} K_{pq} c_4 \quad (188)$$

$$d_4 = c_1 + K_{pwm} K_{pd} c_4 \quad (189)$$

$$d_5 = K_{pwm} K_{id} c_4 \quad (190)$$

$$a_1 = -c_3 \psi_{dro}^{'e} - i_{dso}^e (1 - K_{ps}) - d_3 K_1 K_2 K_{ps} \quad (191)$$

$$a_2 = c_3 \psi_{qro}^{'e} + i_{qso}^e (1 - K_{ps}) \quad (192)$$

$$a_3 = -i_{dso}^e K_{is} + d_3 K_1 K_2 K_{is} \quad (193)$$

The operating point quantities listed in the above are found once the desired load torque and commanded speed are specified. For instance,

$$\omega_{eo} = \frac{4 \omega_b^2 r_r' (T_{Lo} + B \omega_{ro})}{3 P X_m^2 I_{m,pk}^2} + \omega_{ro} \quad (194)$$

$$i_{dso}^e = I_{m,pk} \quad (195)$$

$$s\omega_o = \frac{\omega_{eo} - \omega_{ro}}{\omega_b} \quad (196)$$

$$I_{as,pko}^2 = \frac{4 \omega_b (T_{Lo} + B \omega_{ro}) [(s\omega_o X_r')^2 + r_r'^2]}{3 P X_m^2 s\omega_o r_r'} \quad (197)$$

$$i_{qso}^e = \sqrt{I_{as,pko}^2 - i_{dso}^{e2}} \quad (198)$$

The rotor flux linkages per second operating points are then found from

$$\begin{bmatrix} \psi_{qro}^{'e} \\ \psi_{dro}^{'e} \end{bmatrix} = \begin{bmatrix} c_5 & \omega_{eo} - \omega_{ro} \\ -\omega_{eo} + \omega_{ro} & c_5 \end{bmatrix}^{-1} \begin{bmatrix} c_6 i_{qso}^e \\ c_6 i_{dso}^e \end{bmatrix} \quad (199)$$

Let's consider a design example for the machine parameters listed in Table 14. For the given rated speed and rated voltage, the rated magnetizing current may be evaluated by circuit analysis

$$I_{m,pk} = 0.9684 \text{ A}$$

We also must choose $I_{as,max} = 1.7 \text{ A}$ and a corresponding limit on the slip frequency of $\omega_{sl,lim} = 30 \text{ rad/sec}$. These quantities are required to calculate K_1 in the linearized system. We also will assume that $V_{dc} = 850 \text{ V}$ and $A_t = 10 \text{ V}$. If we choose the coefficient of damping to be $B = 0.001 \text{ N-m-sec}$, the steady-state load torque to be $T_{Lo} = 0.0 \text{ N-m}$, and the steady-state desired speed to be $\omega_r^* = 300 \text{ rad/sec}$, the following operating points are identified by calculation

$$\begin{aligned} i_{qso}^e &= 0.2803 \text{ A} \\ i_{dso}^e &= 0.9684 \text{ A} \\ \psi_{qro}^{'e} &= 0.0 \text{ V} \\ \psi_{dro}^{'e} &= 144.29 \text{ V} \\ \omega_{eo} &= 306.028 \text{ rad/sec} \\ I_{as,pko} &= 1.008 \text{ A} \end{aligned}$$

Note that since this is a 4-pole machine, $\omega_r^* = 300 \text{ rad/sec}$ corresponds to a running speed of 150 rad/sec or 1432 rpm . These values may then be substituted along with the machine parameters into the linearized system and the eigenvalues evaluated for various gains. The following set of gains, $K_{pq} = K_{pd} = 10$, $K_{iq} = K_{id} = 50000$, $K_{ps} = 5.0$, and $K_{is} = 75.0$, resulted in the following set of eigenvalues:

$$\begin{aligned} -4001 \text{ } +/- \text{ } j4919 \\ -3805 \text{ } +/- \text{ } j4683 \\ -15.3 \text{ } +/- \text{ } j5.7 \\ -385 \\ -16.3 \end{aligned}$$

Note that all of the eigenvalues are comfortably in the open left-half plane implying that the selected operating point is stable and should exhibit acceptable transient response. The first two sets of eigenvalues are largely influenced by the current control gains while the remaining four eigenvalues are influenced by the speed control parameters and operating point. It should be clear that the current control dynamics are much faster than the mechanical dynamics and thus our original assumptions are true. A decoupled analysis of the inner and outer control loops may be performed to arrive at a more analytical approach to determining the control gains, however, that will not be presented in this document. To investigate the robustness of the design let's consider another operating point, $T_{Lo} = 0.3 \text{ N-m}$ and $\omega_r^* = 75.0 \text{ rad/sec}$, the new operating point values are

$$i_{qso}^e = 0.3504 \text{ A}$$

$$i_{ds0}^e = 0.9684 \text{ A}$$

$$\psi_{qro}^e = 0.0 \text{ V}$$

$$\psi_{dro}^e = 144.29 \text{ V}$$

$$\omega_{eo} = 82.535 \text{ rad/sec}$$

$$I_{as,pko} = 1.03 \text{ A}$$

The corresponding eigenvalues are located at

$$-3852 \pm j4837$$

$$-3988 \pm j4727$$

$$-16.7 \pm j8.2$$

$$-311$$

$$-16.0$$

and the response is anticipated to be acceptable.

The next step is to evaluate the system using a detailed ACSL simulation. First a couple subtleties must be pointed out. For the system to develop the requisite torque to begin accelerating the machine, it is advisable to first establish the air-gap flux by bringing up i_{ds}^e to its desired value. Next, since the machine torque is limited by the current bound, the machine can only accelerate so quickly. It is generally wise to ramp up the speed at a rate that the machine can logically follow. Furthermore, the speed control integrator should have anti-windup incorporated to avoid large overshoots and settling times.

An ACSL simulation was developed and the following study conducted. The initial 0.1 seconds are used to build up the air-gap flux in the motor while it is at rest. The commanded speed is then ramped up from 0 rad/sec to 300 rad/sec over the next 0.6 seconds. The simulation is then run till 0.9 seconds to assess the settling of the rotor speed and other variables. In this initial study, the load torque is set to zero and only friction is present. The previous set of parameters are assumed and a switching frequency of 5 kHz is employed.

The following figures illustrate the dynamics (Fig. 17-20). Note that the actual rotor electrical angular velocity tracks the desired value and only experiences a slight overshoot (303.7 rad/sec) at the transition point (0.7 sec). It is also clear that the torque follows the commanded slip frequency as expected. In addition, the limit on the slip frequency (30 rad/sec) translates to a limit on the torque (1.48 N-m) and a corresponding limit on i_{qs}^e . The current control is fast and accurate as is illustrated by the d-axis current being locked around its desired value (0.9684 A). Harmonics are apparent in each of the SYN-RF currents and can be further reduced by increasing the switching frequency from 5 kHz. The next set of curves illustrate a step change in load torque from 0 N-m up to 0.5 N-m. The drive responds quickly and, following a 1.5 rad/sec dip in speed, regains operation at the commanded speed. Also, the air-gap flux remains very well regulated at the rated value.

A second study was then performed in which the commanded speed was reduced to 75rad/sec (Figs. 21-22). Once again the commanded speed was ramped up following an initial period in which the air-gap flux was brought up to its rated value. The machine accelerates under current-control up to its new steady-state speed with little overshoot. At 0.9 seconds, a load torque of 0.3N-m was stepped onto the machine. As illustrated in the figure, the drive responds quickly and returns the motor to operation as 75rad/sec.

2. Indirect Method of Vector Control

The second, and final, implementation for an induction machine startup algorithm involves using the indirect method of vector control. Vector control achieves near-instantaneous torque control by properly partitioning the stator current into a flux-controlling component and a torque-controlling component. The flux-controlling component is typically held fixed (unless field- weakening mode is required) so that the rotor flux is maintained at its optimal rated level. The torque-controlling component of the stator current is adjusted based on the output of the speed-control loop. This decoupling control is best explained using the SYN-RF representation of the induction machine. The point of the SYN-RF transformation, in addition to eliminating time-varying inductances, was to create q and d-windings that were mutually orthogonal so that q-currents only effect q-flux and d-currents only effect d-flux. As a consequence, Our decoupling of torque and flux control is realized by recognizing that we need either the q or d-component of the flux to be zero so that the corresponding current component will not effect the flux. It has been shown that instantaneous torque control is achieved by implementing the control with regards to the rotor flux instead of either the stator flux or the air-gap flux. Thus, we impose

$$\psi_{qr}^e = 0 \quad (200)$$

and

$$\frac{d}{dt} \psi_{qr}^e = 0 \quad (201)$$

Therefore i_{qs}^e is used to control the torque and i_{ds}^e is used to set the rotor flux. There are two approaches to realizing these constraints: the direct and the indirect method. In the direct method, the spatial position of the peak rotor flux is located. This is where we must place the SYN-RF d-axis. Thus, we arrive at a θ_e^* which enables us to form i_{qs}^e and i_{ds}^e from the measured stator currents and then also transform the SYN-RF control signals back to abc-quantities for performing STPWM. In the indirect method, a necessary and sufficient condition between i_{qs}^e , i_{ds}^e , and $\omega_e - \omega_r$ is established from the modeling equations. This results in a desired slip angle to which we add the actual rotor electrical position to derive the required SYN-RF angle. The θ_e^* is then used as described previously.

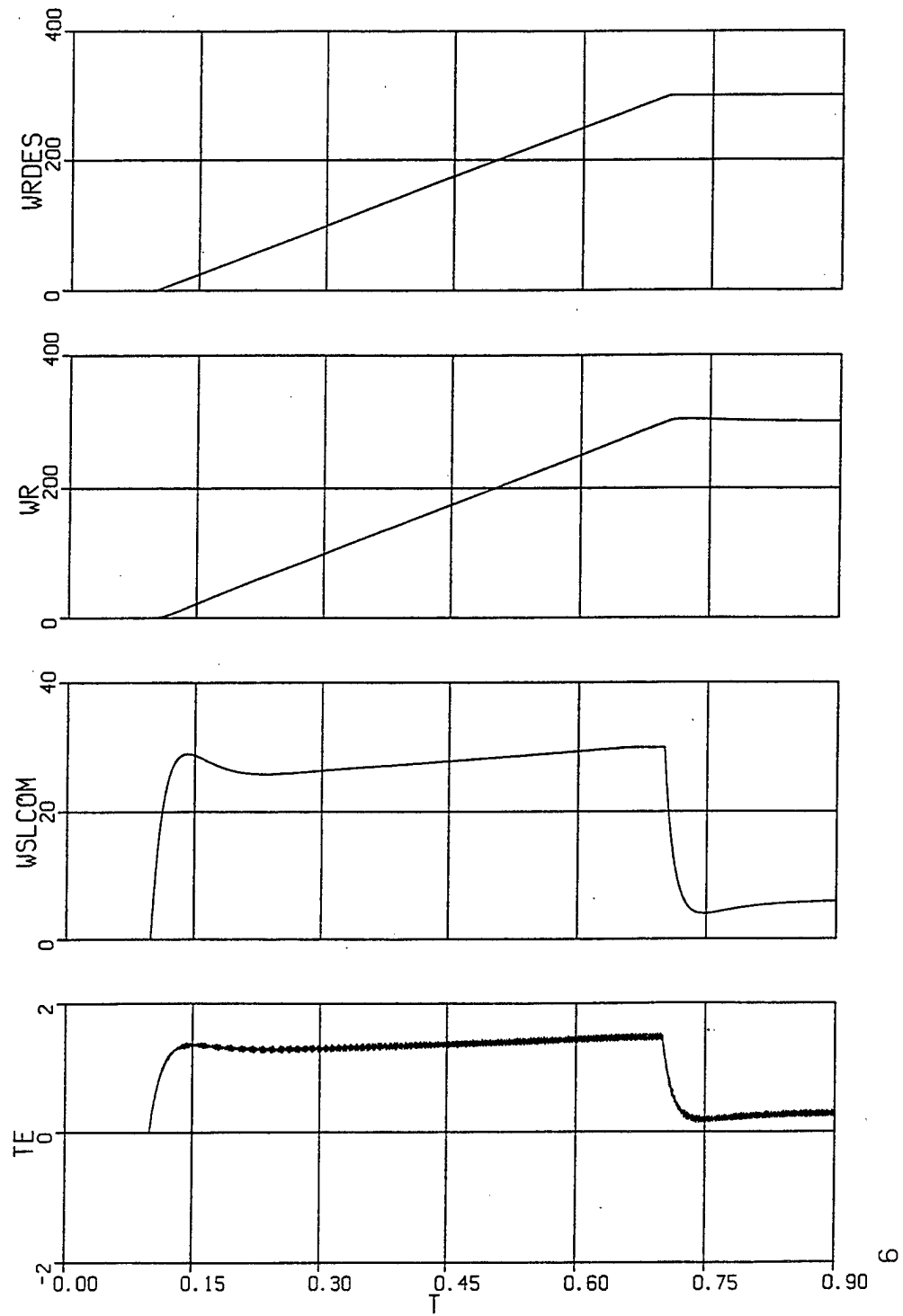


Figure 17. Startup Waveforms for Constant Air-Gap Flux Control

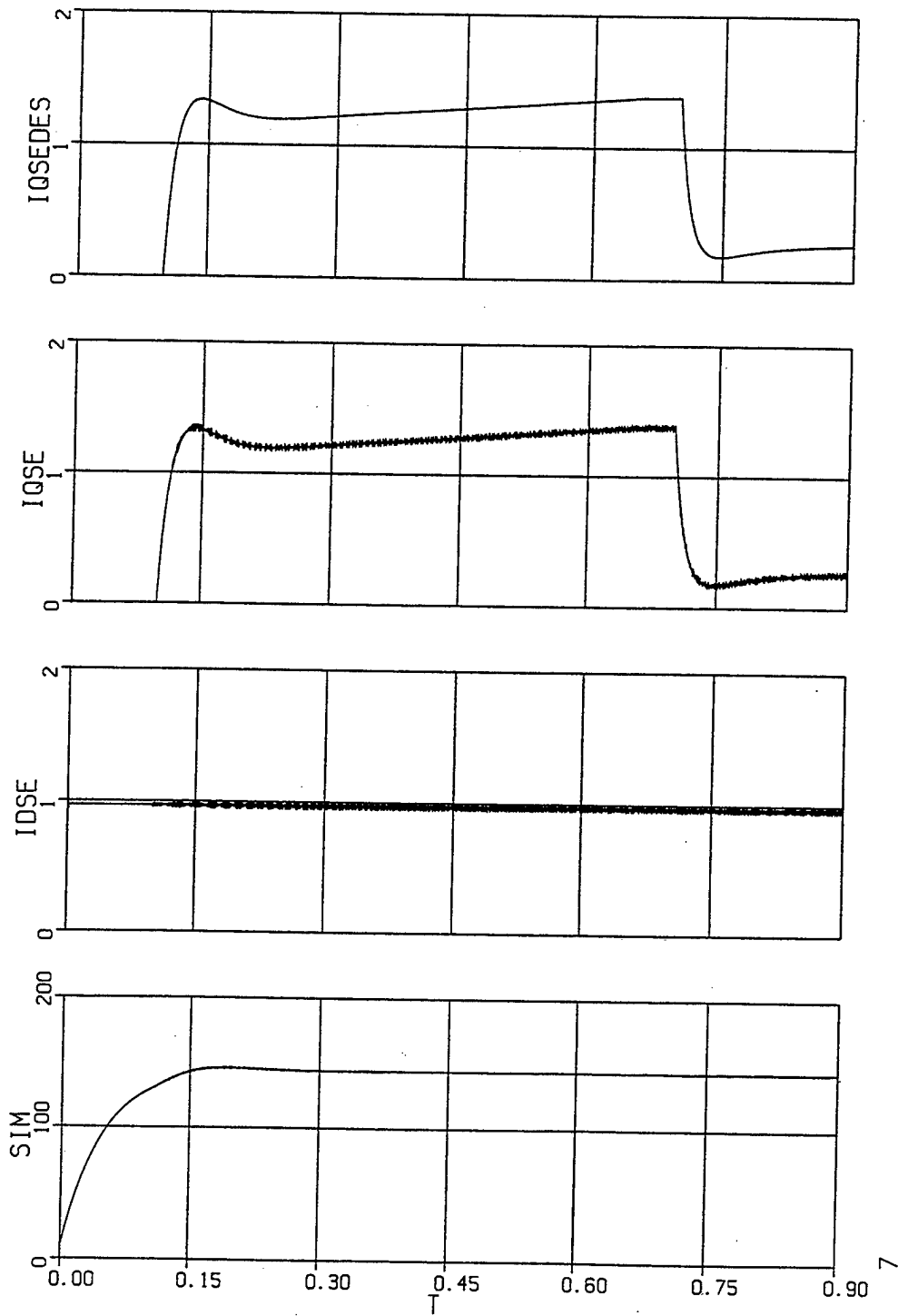


Figure 18. Current and Flux Waveforms Corresponding to Figure 17.

The slip relationship that must hold for the q-axis rotor flux to be held at zero is

$$\omega_e - \omega_r = \frac{r_r' X_m \omega_b}{X_{rr'}} \frac{i_{qs}^{e*}}{\psi_{dr}^{e*}} \quad (202)$$

If we choose to hold i_{ds}^{e*} constant so that $\psi_{dr}^{e*} = X_m i_{ds}^{e*}$, then it follows that the required SYN-RF angle is given by

$$\theta_e^* = \theta_r + \int_0^t \frac{r_r' \omega_b}{X_{rr'}} \frac{i_{qs}^{e*}}{i_{ds}^{e*}} d\zeta \quad (203)$$

Therefore, the principle difference between the vector control implementation and the previous approach is now the speed control loop output is i_{qs}^{e*} and ω_e^* is no longer required since we are directly forming θ_e^* . The nonlinear mapping between ω_{sl}^* and $I_{as,pk}$ is no longer needed as is the partitioning of $I_{as,pk}$ into i_{qs}^{e*} and i_{ds}^{e*} .

The attractive features of vector control are realized as long as the control remains tuned, that is, as long as the parameters used in the slip relationship closely match those of the machine. Typically, adaptive algorithms, such as an extended Kalman filter, may be merged with the vector control to provide updates on the rotor resistance which is a very temperature dependent parameter. Such an expense is not warranted for drives which do not require instantaneous torque response and is not considered here.

The design of the current control gains and speed control gains may be accomplished in a manner analogous to the previous section. First, note that the equations for the induction machine will be the same. Next, the slip frequency constraint is forcing

$$\omega_e^* = \frac{r_r' \omega_b}{X_{rr'} i_{ds}^{e*}} i_{qs}^{e*} + \omega_r = T_1 i_{qs}^{e*} + \omega_r \quad (204)$$

and thus linearizing

$$\Delta \omega_e^* = T_1 \Delta i_{qs}^{e*} + \Delta \omega_r \quad (205)$$

The output of the speed control loop is similar to before

$$i_{qs}^{e*} = K_{ps} (\omega_r^* - \omega_r) + K_{is} x_s \quad (206)$$

or linearizing

$$\Delta i_{qs}^{e*} = K_{ps} (\Delta \omega_r^* - \Delta \omega_r) + K_{is} \Delta x_s \quad (207)$$

Inserting the current control dynamics and the linearization of the induction machine dynamics results in

$$\frac{d}{dt} \Delta \vec{x}_{im2} = A_{im2} \Delta \vec{x}_{im2} + B_{im2} \Delta \vec{u}_{im2} \quad (208)$$

$$A_{im2} = \begin{bmatrix} -d_1 & -\omega_{co} & c_2 & -c_3 \omega_{ro} & a_4 & d_2 & 0 & a_6 \\ \omega_{co} & -d_4 & c_3 \omega_{ro} & c_2 & a_5 & 0 & d_5 & K_{is} T_1 i_{qso}^e \\ c_6 & 0 & -c_5 & -\omega_{co} + \omega_{ro} & K_{ps} T_1 \psi_{dro}^e & 0 & 0 & -K_{is} T_1 \psi_{dro}^e \\ 0 & c_6 & \omega_{co} - \omega_{ro} & -c_5 & -K_{ps} T_1 \psi_{qro}^e & 0 & 0 & K_{is} T_1 \psi_{qro}^e \\ c_8 \psi_{dro}^e & -c_8 \psi_{qro}^e & -c_8 i_{dso}^e & c_8 i_{qso}^e & -c_7 & 0 & 0 & 0 \\ -1 & 0 & 0 & 0 & K_{ps} & 0 & 0 & K_{is} \\ 0 & -1 & 0 & 0 & 0 & 0 & 0 & 0 \\ 0 & 0 & 0 & 0 & -1 & 0 & 0 & 0 \end{bmatrix} \quad (209)$$

$$B_{im2} = \begin{bmatrix} -i_{dso}^e T_1 K_{ps} + d_3 K_{ps} & 0 \\ i_{qso}^e T_1 K_{ps} & 0 \\ -\psi_{dro}^e T_1 K_{ps} & 0 \\ \psi_{qro}^e T_1 K_{ps} & 0 \\ 0 & -c_9 \\ K_{ps} & 0 \\ 0 & 0 \\ 1 & 0 \end{bmatrix} \quad (210)$$

$$\Delta \vec{x}_{im2} = \begin{bmatrix} \Delta i_{qs}^e & \Delta i_{ds}^e & \Delta \psi_{qr}^e & \Delta \psi_{dr}^e & \Delta \omega_r & \Delta x_q^e & \Delta x_d^e & \Delta x_s \end{bmatrix}^t \quad (211)$$

$$\Delta \vec{u}_{im2} = \begin{bmatrix} \Delta \omega_r^* & \Delta T_L \end{bmatrix}^t \quad (212)$$

where the additional constants are

$$a_4 = -i_{dso}^e (1 - T_1 K_{ps}) - c_3 \psi_{dro}^e - d_3 K_{ps} \quad (213)$$

$$a_5 = i_{qso}^e (1 - T_1 K_{ps}) + c_3 \psi_{qro}^e \quad (214)$$

$$a_6 = -i_{dso}^e T_1 K_{is} + d_3 K_{is} \quad (215)$$

In order to determine the operating points to be inserted in the above linearized system, the peak rotor-referred flux must be identified by analyzing the steady-state equivalent circuit for rated conditions. This yields

$$\psi_{dro}^e = 143.725 \text{ V}$$

Also if the control is tuned, the necessary and sufficient condition guarantees that

$$\psi_{qro}^e = 0 \text{ V}$$

The d-axis stator current is fixed by the desired rotor flux according to

$$i_{dso}^e = \frac{\psi_{dro}^e}{X_m} = 0.9646 \text{ A}$$

The q-axis stator current is established from the cumulative load on the shaft. Since during tuned vector control

$$T_e = \frac{3 P X_m}{4 \omega_b X_{\pi}} \frac{i_{qso}^e}{\psi_{dro}^e} = T_{Lo} + B \omega_{ro} \quad (216)$$

the q-axis stator current is found readily. Let's consider a numerical example and illustrate

some effective gains. Assume that $T_{Lo} = 0 \text{ N-m}$ and $\omega_r^* = 300 \text{ rad/sec}$. This leads to

$$i_{qso}^e = 0.2814 \text{ A}$$

$$\omega_{eo} = 306.075 \text{ rad/sec}$$

Substituting into the linearized system equations, gains may now be selected and the eigenvalues evaluated. Once again, it was assumed that $V_{dc} = 850 \text{ V}$ and $A_t = 10 \text{ V}$. The following set of gains, $K_{pq} = K_{pd} = 10$, $K_{iq} = K_{id} = 50000$, $K_{ps} = 0.1$, and $K_{is} = 5.0$, resulted in the following set of eigenvalues:

$$-4102 \pm j4890$$

$$-3853 \pm j4587$$

$$-44.7 \pm j49.5$$

$$-20.8 \pm j6.1$$

A variety of operating points were then assessed and it was found that the eigenvalues were largely fixed in the complex plane, with the dominant eigenvalues at around -20.

The vector control was next to be assessed via detailed ACSL simulation. Similar provisions were placed on the speed control to ensure against integrator anti-windup. Initially, 0.1 seconds are reserved to allow the rotor flux to be established at which point the commanded speed is ramped up over a 0.6 second interval and then held fixed for an additional 0.2 seconds. The results are documented in the following figures.

In the study (Figs. 23-26), a 0.1 second time period is used to build up the rotor flux to its prescribed value. The commanded speed is then ramped up to 300 rad/sec over a 0.6 sec interval. The study is run till $t = 0.9 \text{ sec}$. The drive responds with excellent performance -- only a slight 2% overshoot. At 0.9 sec the load torque is stepped from 0 N-m up to 0.5 N-m. The eigenvalue selections result in a slightly overdamped response which settles out in 0.2 sec. The transient in the rotor speed is quite acceptable. The change in rotor flux is hardly noticeable.

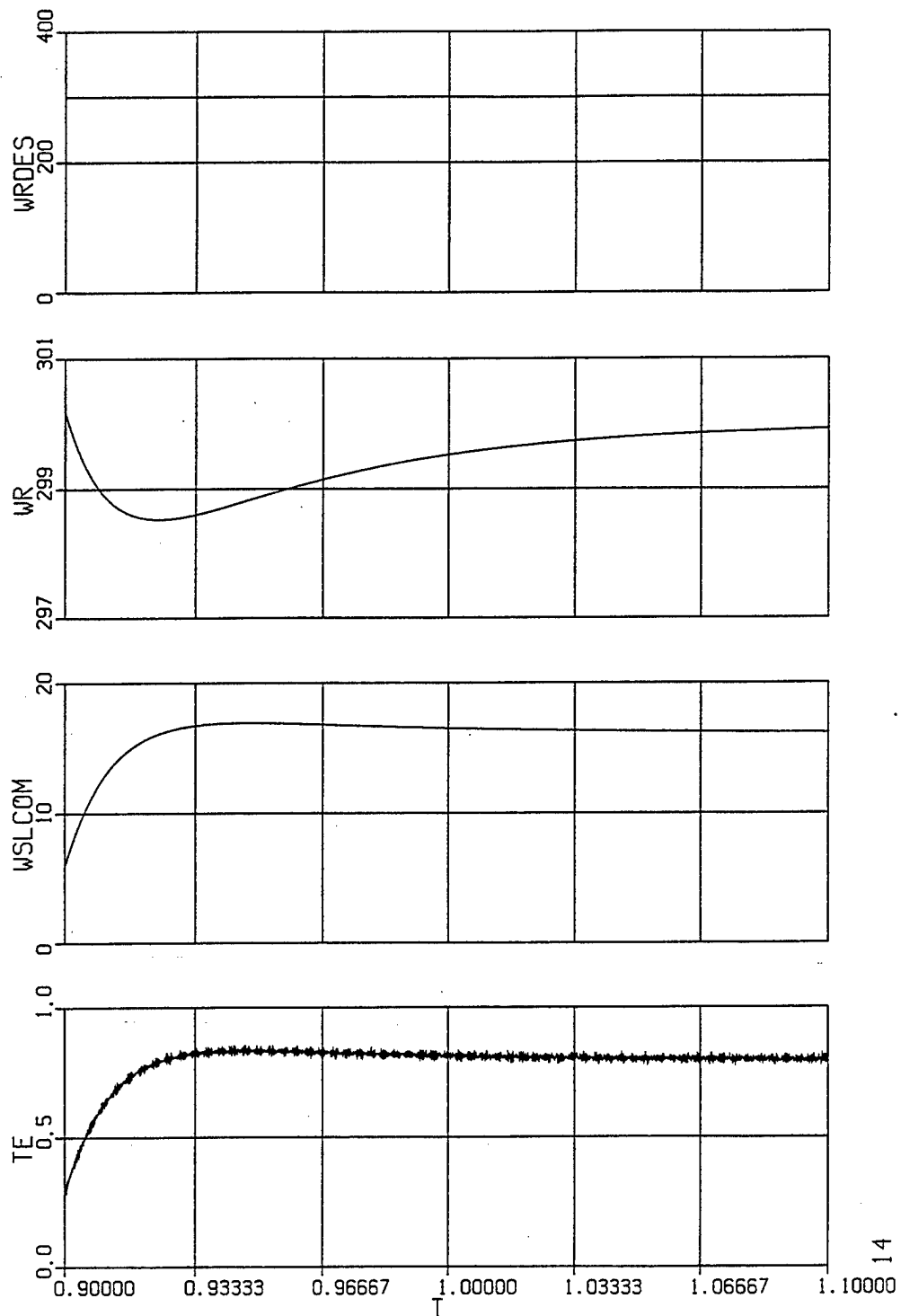


Figure 19. Transient Behavior During a Load Torque Change

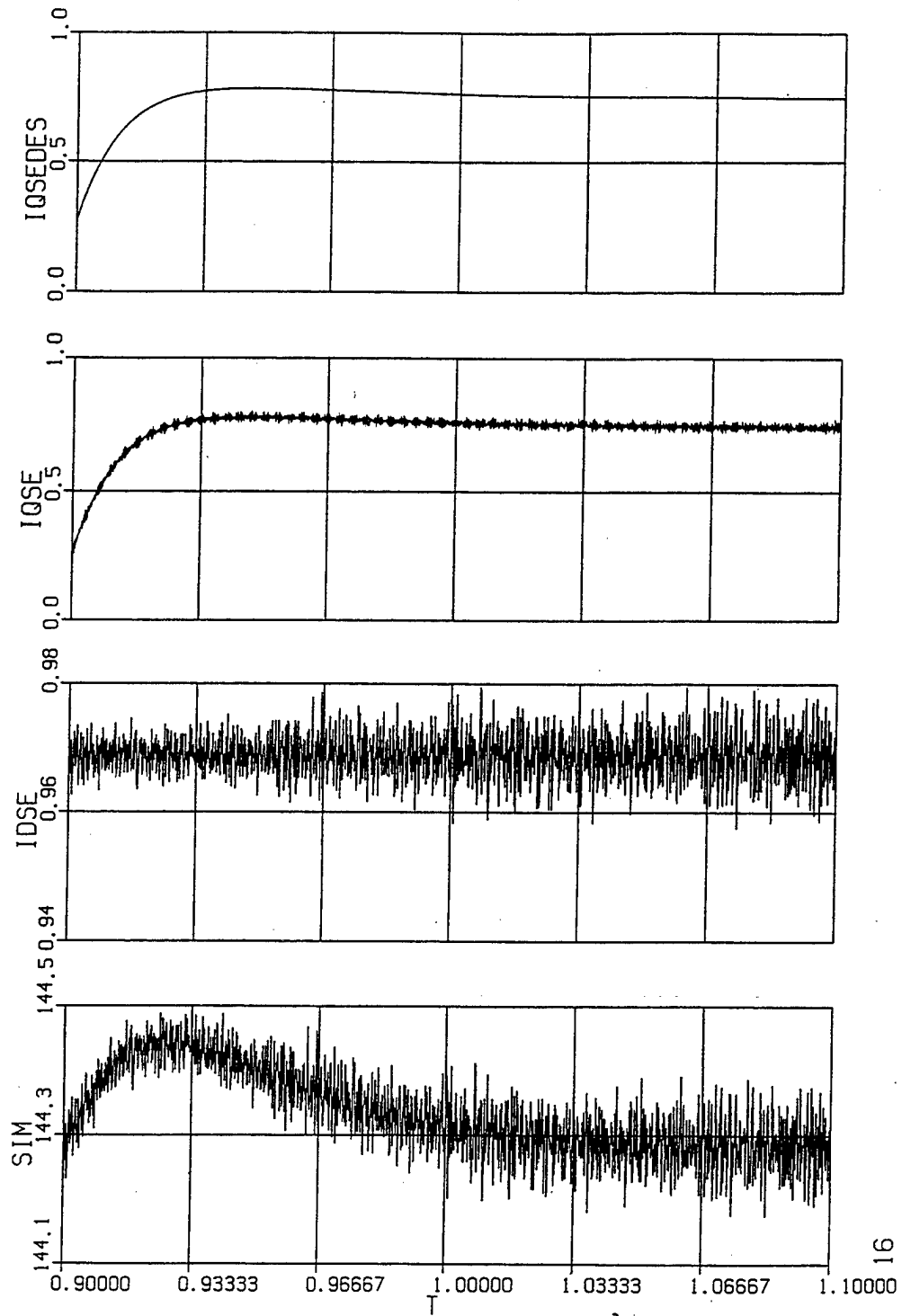


Figure 20. Current and Flux Waveforms Corresponding to Figure 19.

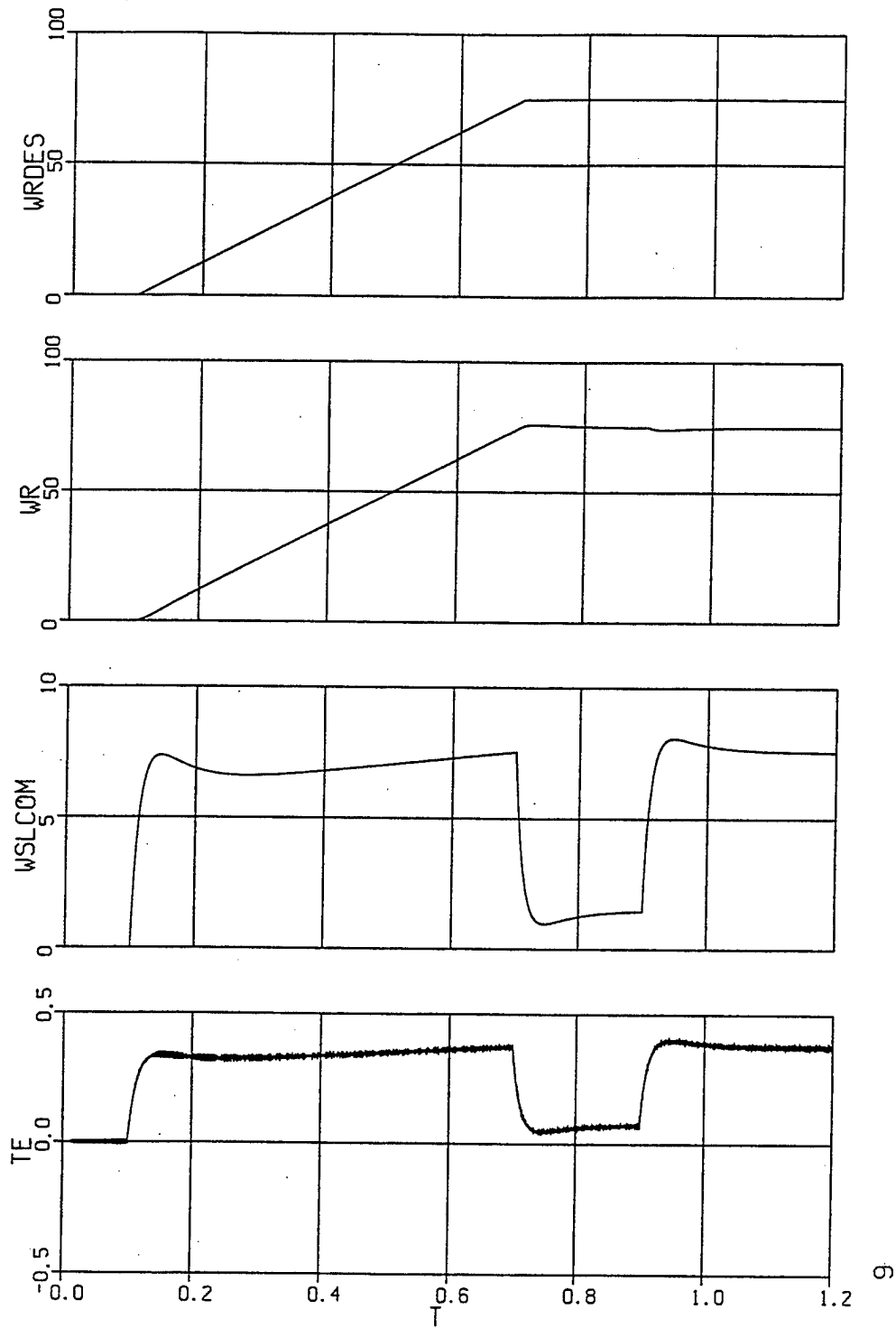


Figure 21. Startup Behavior for a Lower Commanded Speed

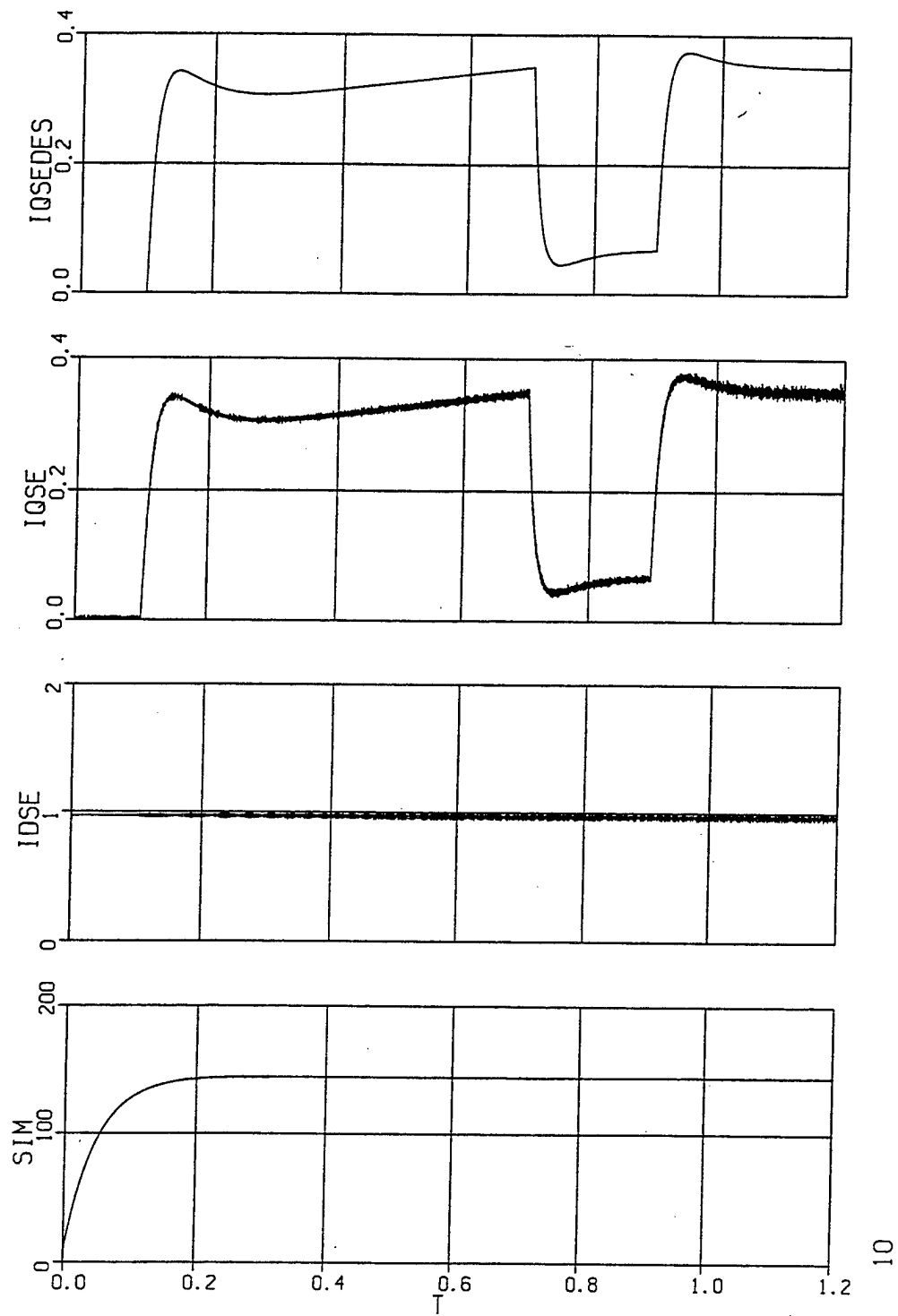


Figure 22. Current and Flux Waveforms Corresponding to Figure 21.

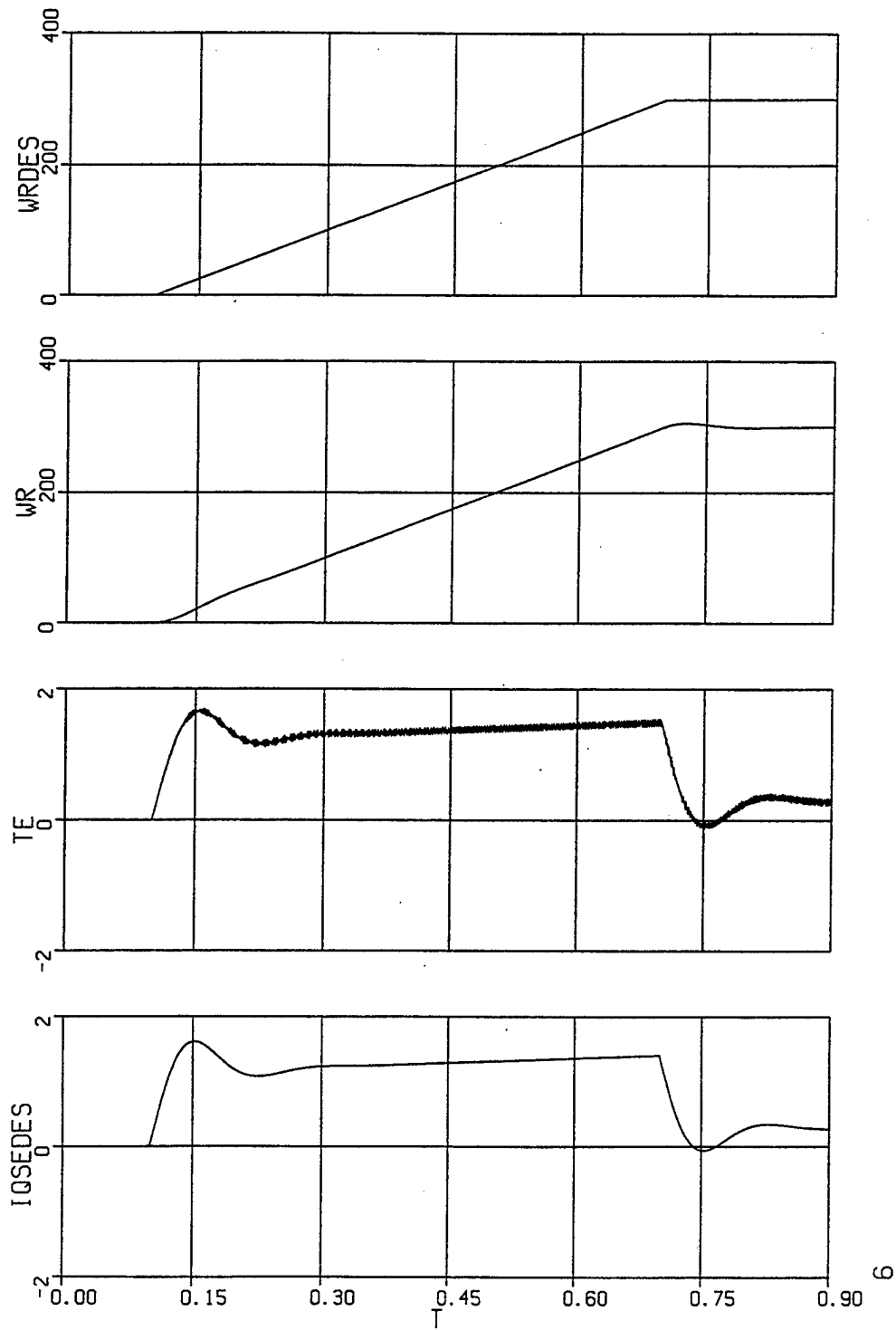


Figure 23. Startup Waveforms for Vector Control

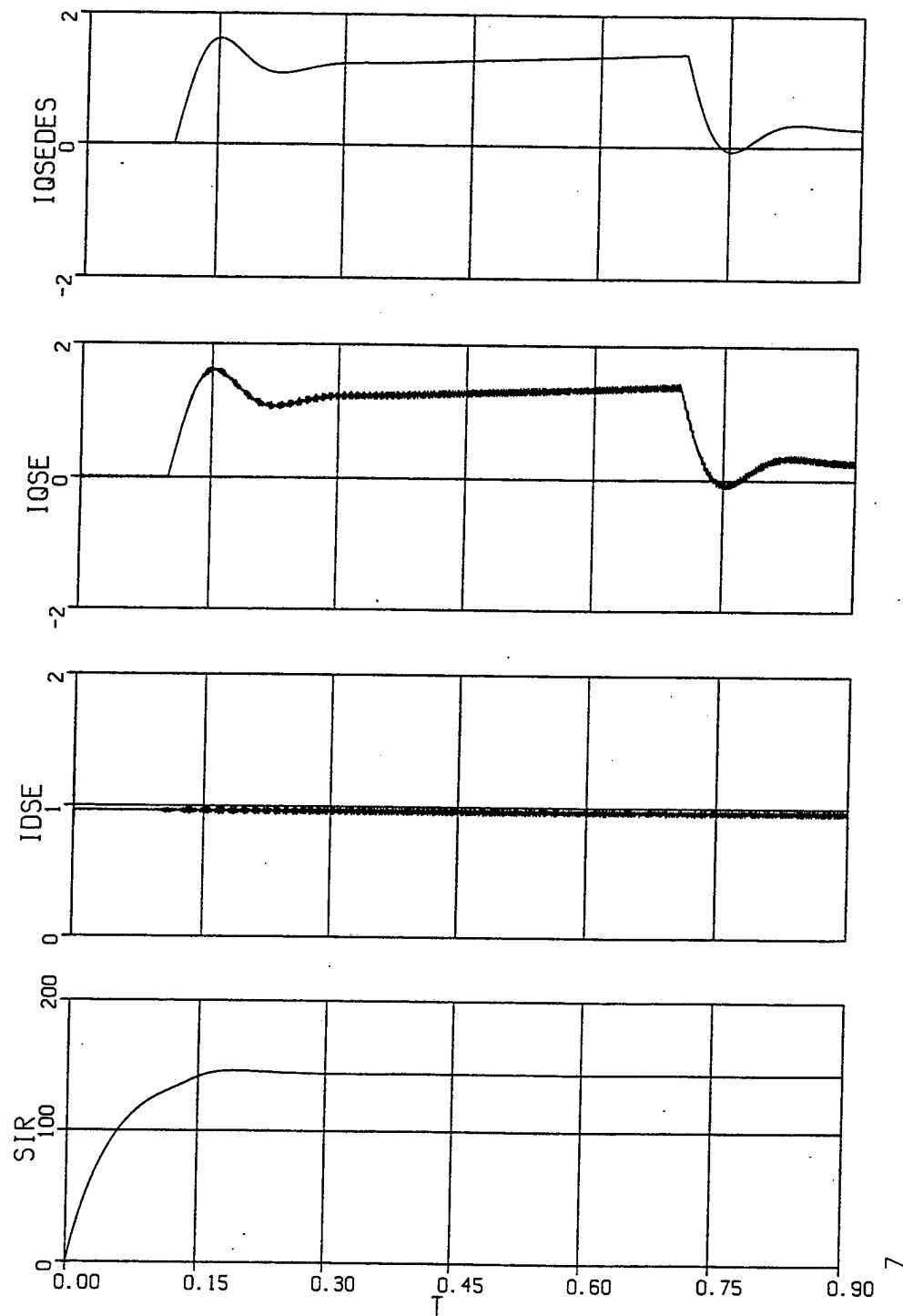
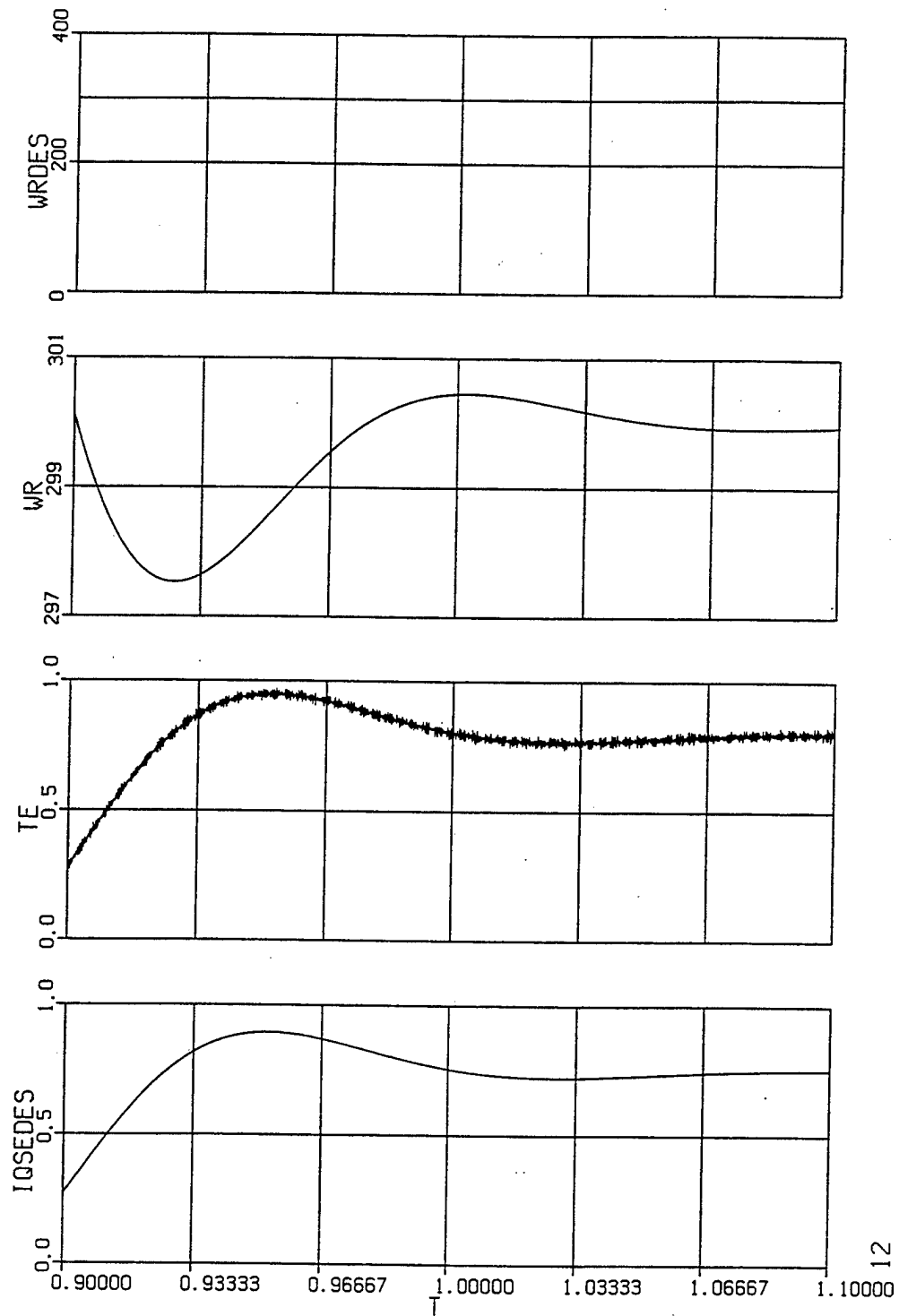
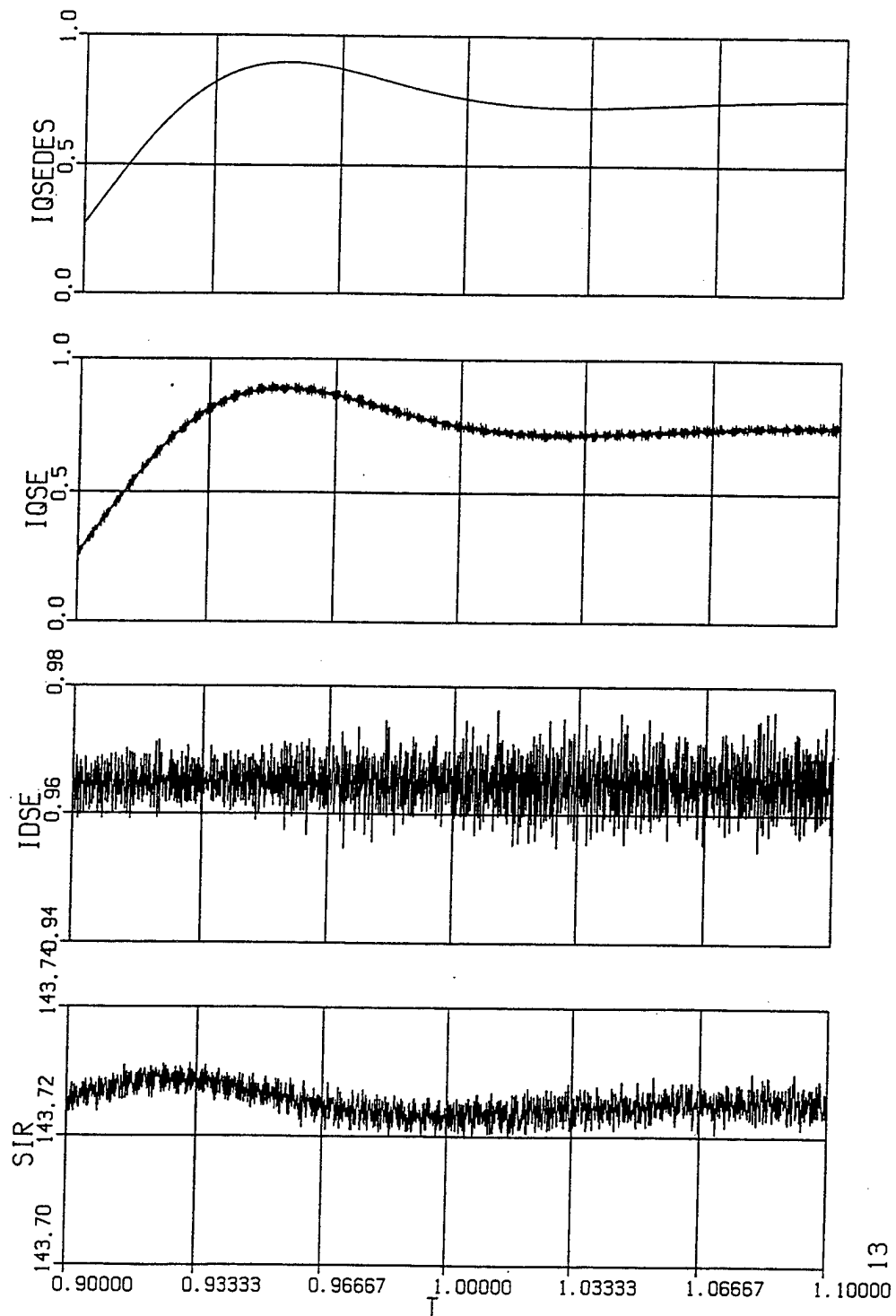


Figure 24. Current and Flux Waveforms Corresponding to Figure 23.



12

Figure 25. Transient Behavior During a Load Torque Change



13

Figure 26. Current and Flux Waveforms Corresponding to Figure 25.

C. Concluding Comments

The Navy is actively developing Power Electronic Building Blocks (PEBBs) in support of its initiatives into DC Zonal Electric Distribution (DC ZEDS). DC ZEDS, in turn, is a component of the larger Integrated Power System (IPS) initiative that seeks to power both ship service and ship propulsion from a common set of prime movers. The principle PEBB-like components under development currently are the Ship Service Converter Module (SSCM) and the Ship Service Inverter Module (SSIM) as specified in DC ZEDS. These devices are basically fast-switching, high-bandwidth, high-power buck choppers and Pulse-Width-Modulation (PWM) inverters, respectively. Currently, the Auxiliary Resonant Commutated Pole (ARCP) inverter is the topology of choice due to its inherent soft-switching advantages while a Zero-Voltage-Switching (ZVS) buck chopper is being investigated to replace its hard-switched counterpart.

The purpose of this report was to document several algorithms which may be employed to control a conventional three-phase PWM inverter. It is assumed that the soft-switching aspect of the ARCP inverter is being handled internal to the unit. The report first documented two approaches to developing the actual modulation signals. First, the discretization of Sine-Triangle PWM (STPWM) was considered and the issues regarding implementation with the PEBB Universal Controller Generation 0 (PUC-GEN0) were highlighted. Specific coding details are documented in both Hanson and Floodeen. Next, Space Vector Modulation (SVM) was outlined and various equations required for implementation identified. SVM has an advantage of being able to realize slightly larger voltages in the linear modulation range but also requires far more calculation capacity or more extensive look-up tables. This poses a trade-off. For very complex feedback control algorithms, the extra overhead involved in SVM may preclude its selection.

The next section of the report documented current and voltage control strategies for a three-phase PWM inverter. In particular with regards to the current control, algorithms were presented which were implemented in both the Stationary Reference Frame (STA-RF) and the Synchronous Reference Frame (SYN-RF). For generality, a standard three-phase resistive-inductive (RL) load was assumed for convenience. The STA-RF control is more easily implemented since there are no angle-dependent transformations required; however, steady-state accuracy is very parameter dependent and therefore care must be exercised. Modeling equations were derived for the STA-RF control and design example used to illustrate the selection of the feedback gains. A detailed ACSL simulation was then used to illustrate the system dynamics. The SYN-RF control is slightly more complicated due to the fact that the feedback signals must be transformed to the SYN-RF via a diffeomorphic angle-dependent transformation. In addition, signals internal to the control must then be mapped back to abc-quantities for STPWM or to STA-RF-quantities for SVM. However, a SYN-RF control was successfully implemented in the NPS Power Systems

Laboratory using the dSPACE control development system (Frasz, 1998) and its advantage far outweighs the added complexities. In particular, the integral-action in the SYN-RF guarantees zero steady-state error since sinusoidal quantities appear as constants in the SYN-RF. Modeling equations were derived for the SYN-RF control and a similar design example used to illustrate the selection of feedback gains. An ACSL simulation was implemented and used to study the dynamic performance. Results were found to be acceptable.

Most shipboard applications will probably require a well-regulated output voltage. The next section of the report documented a sophisticated inverter output voltage control which relies heavily on reference frame theory. It incorporates an outer voltage control loop and an inner current control loop and various feedforward signals. The modeling equations were set forth, a design example used to illustrate the selection of feedback gains, and a detailed ACSL simulation used to document the dynamic performance. This algorithm requires a number of feedback signals but results in superior dynamic performance as illustrated in the aforementioned studies. A systematic algorithm for determining the feedback gains was set forth and shown to be independent of the load parameters themselves.

The final section of the report dealt with two algorithms for handling the startup of a three-phase induction machine load. Both algorithms utilized an outer speed control loop and an inner current control loop. The first algorithm used the output of the outer speed control loop to program a desired slip frequency which, in turn, was bounded to limit the torque and current. The commanded slip frequency was added to the rotor electrical angular velocity to arrive at the desired inverter switching frequency (in rad/sec). In addition, the commanded slip frequency signal was then used to map into a commanded stator current amplitude in order to achieve constant air-gap flux in the steady state. The current amplitude was then apportioned into commanded synchronous reference frame currents and sent to the inner current control, which was simply the SYN-RF current control from a previous section. The modeling equations were set forth and a linearized system derived to aid in the selection of control gains for a representative machine from the NPS Power Systems Laboratory. A detailed ACSL simulation was formulated to illustrate the dynamics.

Finally, an alternative startup strategy was derived using the indirect method of vector control. The theory was introduced, the equations assembled, a linearized system formulated, a design example proffered, and an ACSL simulation generated and exercised. The basic difference between this algorithm and the previous is that a necessary-and-sufficient condition on the slip frequency is derived which guarantees near-instantaneous torque response. This condition is used in a feedforward sense together with a measure of the rotor position to derive a desired SYN-RF angle. This angle is then used directly in

the control to map the SYN-RF signals back to abc-modulating signals. The simulation study results illustrated acceptable performance.

PWM Inverter control algorithms must be derived with vision of all anticipated loading conditions. With this in mind, additional considerations must be kept in mind. In particular, paralleling of inverter modules to share a load proportionately is a key issue. Also, the impact of input filters on overall system stability must be an issue which is heeded.

REFERENCES

- [1] C. Petry and J. Rumburg, "Zonal Electrical Distribution Systems: An Affordable Architecture for the Future," *Naval Engineers Journal*, Vol. 105, pp. 45-51, May, 1993.
- [2] N. Doerry and J. Davis, "Integrated Power System for Marine Applications," *Naval Engineers Journal*, Vol. 106, pp. 77-90, May, 1994.
- [3] R. DeDoncker and J. Lyons, "The Auxiliary Resonant Commutated Pole Converter," *IEEE-IAS Annual Meeting Proceedings*, pp. 1228-1235, 1990.
- [4] J. Mayer and F. Salberta, "High-Frequency Power Electronic Converter for Propulsion Applications," *Dept. of EE and Applied Research Laboratory*, Penn State University, University Park, PA.
- [5] J. Kassakian, M. Schlect and G. Verghese, *Principles of Power Electronics*, Boston MA.: Addison-Wesley Pub. Co., 1991.
- [6] P. Krause, O. Wasynczuk and S. Sudhoff, *Analysis of Electric Machinery*, McGraw-Hill, New York, 1986.
- [7] N. Mohan, T. Undeland, W. Robbins, *Power Electronics, Converters, Applications and Design* John Wiley & Sons, Inc., New York, 1989.
- [8] R. DeDoncker and J. Lyons, "Control of Three Phase Power Supplies for Ultra Low THD," *APEC Sixth Annual Applied Power Electronics Conference and Exposition*, pp. 622-629, March 1991.
- [9] T. Rowan and R. Kerkman, "A New Synchronous Current Regulator and an Analysis of Current Regulated PWM Inverters," *IEEE-IAS Annual Meeting*, pp. 487-495, 1985.
- [10] Mitchell and Gauthier Associates, *Advanced Continuous Simulation Language Reference Manual*, Concord, MA., 1993.
- [11] H. Van der Broeck, H. Skudelny and G. Stanke, "Analysis and Realization of a Pulsewidth Modulator Based on Voltage Space Vectors," *EEE Conference on Industrial Electronics Proceedings*, Vol. 24, pp. 142-150, 1988.
- [12] T. Rowan, "Analysis of Naturally Sampled Current Regulated Pulse-Width-Modulated Inverters," Doctoral Thesis, University of Wisconsin - Madison, 1985.

- [13] R. Hanson, "*Implementing Desired Control Algorithms for ARCP Inverters and DC-to-DC Converters Using Existing DSP Resources*," Master's Thesis, Naval Postgraduate School, June 1997.
- [14] M. Oberley, "*The Operation and Interaction of the Auxiliary Resonant Commutated Pole Converter in a Shipboard DC Power Distribution Network*," Master's Thesis, Naval Postgraduate School, December 1996.
- [15] D. Floodeen, "*Implementing Desired Control Algorithms for Auxiliary Resonant Commutated Pole PWM Inverters Using Existing DSP Resources*," Master's Thesis, Naval Postgraduate School, September 1998.
- [16] H. Blalock III, "*Power Electronic Converter Simulation, Real Time Control and Hardware-in-the-Loop Testing for a Shipboard Integrated Power System*," Master's Thesis, Naval Postgraduate School, March 1995.
- [17] B. Salerno, "*Controller Design, Analysis, and Prototype for Ship Service Converter Module*," Master's Thesis, Naval Postgraduate School, June 1996.

INITIAL DISTRIBUTION LIST

		No. Copies
1.	Defense Technical Information Center 8725 John J. Kingman Rd, STE 0944 Ft. Belvoir, VA 22060-6218	2
2.	Dudley Knox Library, Code 52 Naval Postgraduate School 411 Dyer Road Monterey, CA 93943-5101	2
3.	Research Office, Code 09 Naval Postgraduate School 589 Dyer Road Monterey, CA 93943-5138	1
4.	Chairman, Code EC Department of Electrical and Computer Engineering Naval Postgraduate School 833 Dyer Road Monterey, CA 93943-5121	1
5.	Professor John G. Ciezki, Code EC/Cy Department of Electrical and Computer Engineering Naval Postgraduate School 833 Dyer Road Monterey, CA 93943-5121	2
6.	Professor Robert W. Ashton, Code EC/Ah Department of Electrical and Computer Engineering Naval Postgraduate School 833 Dyer Road Monterey, CA 93943-5121	2
7.	Naval Surface Warfare Center Attn: Robert Cooley Carderock Division/Annapolis Detachment 3A Leggett Circle Annapolis, MD 21402-5067	2
8.	Naval Surface Warfare Center Attn: Joe Borraccini Carderock Division/Annapolis Detachment 3A Leggett Circle Annapolis, MD 21402-5067	2

No. Copies

9. Naval Surface Warfare Center
Attn: Mike Golda
Carderock Division/Annapolis Detachment
3A Leggett Circle
Annapolis, MD 21402-5067

1